

E-ISSN 2980-3012

Physics and Astronomy Reports

VOLUME 2 • NUMBER 1 • JUNE 2024



İSTANBUL
UNIVERSITY
PRESS

Indexing and Abstracting

NASA/ADS



OWNER

Prof. Dr. Tansel AK

Istanbul University, Faculty of Science, İstanbul, Türkiye

RESPONSIBLE MANAGER

Prof. Dr. Elif AKALIN

Istanbul University, Faculty of Science,
Department of Physics, İstanbul, Türkiye

CORRESPONDENCE ADDRESS

Istanbul University Faculty of Science
PK 34134 Vezneciler, Fatih, İstanbul, Türkiye

Phone : +90 (212) 455 57 00

Fax : +90 (212) 512 21 40

E-mail: par@istanbul.edu.tr

<https://iupress.istanbul.edu.tr/en/journal/par/home>

<https://dergipark.org.tr/en/pub/par>

PUBLISHER

Istanbul University Press

Istanbul University Central Campus,
34452 Beyazıt, Fatih, İstanbul, Türkiye

Phone: +90 (212) 440 00 00

Authors bear responsibility for the content of their published articles.

The publication language of the journal is English.

This is a scholarly, international, peer-reviewed and open-access journal published biannually in June and December.

Publication Type: Periodical

EDITORIAL MANAGEMENT BOARD

EDITOR-IN-CHIEF

Prof. Dr. Elif AKALIN – İstanbul University, Faculty of Science, Department of Physics, İstanbul, Türkiye – eakalin@istanbul.edu.tr

CO-EDITOR

Prof. Dr. Selçuk BİLİR – İstanbul University, Faculty of Science, Department of Astronomy and Space Sciences, İstanbul, Türkiye – sbilir@istanbul.edu.tr

STATISTICS EDITOR

Assit. Prof. Dr. Hikmet ÇAKMAK – İstanbul University, Faculty of Science, Department of Computer Science, İstanbul, Türkiye – hcakmak@istanbul.edu.tr

PUBLICITY MANAGER

Assit. Prof. Dr. Talar YONTAN – İstanbul University, Faculty of Science, Department of Astronomy and Space Sciences, İstanbul, Türkiye – talar.yontan@istanbul.edu.tr

ETHICS EDITOR

Prof. Dr. İpek KANAT ÖZTÜRK – İstanbul University, Faculty of Science, Department of Physics, İstanbul, Türkiye – ikanat@istanbul.edu.tr

EDITORIAL ASSISTANT

Assit. Prof. Dr. Özgecan ÖNAL TAŞ – İstanbul University, Faculty of Science, Department of Astronomy and Space Sciences, İstanbul, Türkiye – ozgecan.onal@istanbul.edu.tr

LANGUAGE EDITORS

Elizabeth Mary EARL – İstanbul University, İstanbul, Türkiye – elizabeth.earl@istanbul.edu.tr

EDITORIAL BOARD

Volkan BAKIŞ – Akdeniz University, Antalya, Türkiye – volkanbakis@akdeniz.edu.tr

Timothy BANKS – Harper College, Chicago, United-States – tim.banks@nielsen.com

Gönül BAŞAR – İstanbul University, İstanbul, Türkiye – gbasar@istanbul.edu.tr

Helene CARRERE – University of Toulouse, Toulouse, France – carrere@insa-toulouse.fr

Ömür ÇAKIRLI – Ege University, İzmir, Türkiye – omur.cakirli@ege.edu.tr

Uğur ÇEVİK – Karadeniz Teknik University, Trabzon, Türkiye – ugurc@ktu.edu.tr

Ahmet DERVİŞOĞLU – Ataturk University, Erzurum, Türkiye – ahmet.dervisoglu@atauni.edu.tr

Goran DJORDJEVIC – University of Nis, Nis, Serbia – gorandj@junis.ni.ac.rs

Yavuz EKŞİ – İstanbul University, İstanbul, Türkiye – eksi@itu.edu.tr

Ayşe EROL – Akdeniz University, Antalya, Türkiye – ayseerol@istanbul.edu.tr

Muhsin HARAKEH – University of Groningen, Groningen, Netherlands – m.n.harakeh@rug.nl

Mohamed HENINI – University of Nottingham, Nottingham, United-Kingdom – Mohamed.Henini@nottingham.ac.uk

Ümit KAVAK – NASA Ames Research Center, Moffett-Field, United-States – ukavak@sofia.usra.edu

Mükremin KILIÇ – University of Oklahoma, Oklahoma, United-States – kilic@ou.edu

Sophie KRÖGER – Hochschule für Technik und Wirtschaft Berlin, Berlin, Germany – sophie.kroeger@hte-berlin.de

Yeşim ÖKTEM – İstanbul University, İstanbul, Türkiye – yesim.oktem@istanbul.edu.tr

Faruk SOYDUGAN – Canakkale Onsekiz Mart University, Çanakkale, Türkiye – fsoydugan@comu.edu.tr

Horst STOECKER – Goethe University, Frankfurt, Germany – stoecker@fias.uni-frankfurt.de

Timur ŞAHİN – Akdeniz University, Antalya, Türkiye – timursahin@akdeniz.edu.tr

Hakan Volkan ŞENAVCI – Ankara University, Ankara, Türkiye – hvsenavci@ankara.edu.tr

Kadri YAKUT – Ege University, İzmir, Türkiye – kadri.yakut@ege.edu.tr

Özgür YAVUZÇETİN – University of Wisconsin-Whitewater, Whitewater, United-States – yavuzce@uww.edu

CONTENTS

RESEARCH ARTICLES

- 1 SED Analysis of the Old Open Cluster NGC 188
Deniz Cennet DURSUN, Seval TAŞDEMİR, Seliz KOÇ, Srishti IYER
- 18 The Fundamental Parameters and Evolutionary Status of V454 Aurigae
Gökhan YÜCEL, Remziye CANBAY, Volkan BAKIŞ
- 29 Effect of Annealing on Electronic Transport in Modulation-doped In_{0.32}Ga_{0.68}As/GaAs Quantum Well Structures
Adal RAJHI, Mustafa AYDIN, Ömer DÖNMEZ, Fahrettin SARCAN, Ayşe EROL
- 37 Investigation of Adsorption of the Cardiotonic Drug Milrinone Onto Montmorillonite: An FTIR and Raman Spectroscopic Study
Sevim AKYÜZ

REVIEW ARTICLE

- 41 Fundamentals of Stars: A Critical Look at Mass-Luminosity Relations and Beyond
Zeki EKER, Faruk SOYDUGAN, Selçuk BİLİR

SED Analysis of the Old Open Cluster NGC 188

D. C. Dursun^{1*} , S. Taşdemir¹ , S. Koç¹ , and S. Iyer² 

¹Istanbul University, Institute of Graduate Studies in Science, Programme of Astronomy and Space Sciences, 34116, Beyazıt, İstanbul, Türkiye

²International Centre for Theoretical Sciences, 560089, Bengaluru, Karnataka, India

ABSTRACT

In this study, we investigate the fundamental astrophysical parameters of the old open cluster NGC 188 using two complementary methods: isochron fitting and spectral energy distribution (SED) analysis. Using photometric, astrometric, and spectroscopic data from the *Gaia* Data Release 3 (DR3, [Gaia Collaboration et al. 2023](#)), we identified 868 most likely member stars with membership probabilities $P \geq 0.5$. The mean proper-motion components and trigonometric parallaxes of the cluster are derived as $(\mu_\alpha \cos \delta, \mu_\delta) = (-2.314 \pm 0.002, -1.022 \pm 0.002)$ mas yr⁻¹ and $\varpi = 0.550 \pm 0.023$ mas, respectively. From this initial selection of high probable member stars, we proceed with the determination of astrophysical parameters using the isochron-fitting method. Simultaneously estimating the colour excess, distance and age of the cluster, we employ PARSEC isochrones to observational data on *Gaia* based colour-magnitude diagrams. These findings were obtained as $E(G_{BP} - G_{RP}) = 0.066 \pm 0.012$ mag, $d = 1806 \pm 21$ pc, and $t = 7.65 \pm 1.00$ Gyr, respectively. In addition, we identified and detected 19 previously confirmed blue straggler stars within NGC 188. Subsequently, we performed SED analyses for 412 of the 868 cluster members. We obtained colour excess, distance and age of the cluster as $E(B - V) = 0.034 \pm 0.030$ mag, $d = 1854 \pm 148$ pc, and $t = 7.78 \pm 0.23$ Gyr, respectively. The analysis of member stars revealed patterns of extinction in the *V*-band, with higher values of A_V observed in the lower right quadrant of the cluster. By comparing our SED analysis results with models of stellar evolution, particularly in terms of temperature and surface gravity, we confirm agreement with theoretical predictions. This comprehensive investigation sheds light on the astrophysical properties of NGC 188, contributing to our understanding of stellar evolution within open clusters.

Keywords: Galaxy: open clusters; individual: NGC 188; Methods: spectral energy distribution (SED)

1. INTRODUCTION

Open clusters (OCs) serve as invaluable natural laboratories to investigate the fundamental principles of stellar evolution, Galactic dynamics, and the broader astrophysical processes that shape our Universe. OCs are groups of stars formed from the same molecular cloud under similar physical conditions. Being gravitationally bound systems, OCs feature member stars that share similarities in terms of distance to the Sun, age, chemical composition, position, and velocity ([Harris & Pudritz 1994](#); [Friel 1995](#); [Lada & Lada 2003](#); [Carraro & Costa 2007](#); [Cantat-Gaudin & Anders 2020](#)).

Recent advances in observational techniques have allowed scientists to delve deeper into the complexities of stellar phenomena, with spectral energy distribution (SED) analysis serving as a powerful tool for uncovering the fundamental properties of stars ([Zheng et al. 1999](#)). In astrophysics, SED analysis is a cornerstone method that provides deep insights into the fundamental properties of celestial objects, particularly stars. This analysis manifests in two primary forms: model-based and model-independent approaches. Serving as a link between

theoretical frameworks and observational data, model-based SED analysis aids in determining critical parameters such as effective temperature, surface gravity, and metallicity for stars, thus enhancing our understanding of stellar evolution and behaviour. The examination of the SED of member stars in OCs yields essential astrophysical parameters of the cluster, which, in turn, can be utilized to decipher its dynamics and evolutionary trajectory ([Demarque et al. 1992](#); [Carraro & Chiosi 1994](#); [VandenBerg & Stetson 2004](#)).

Each stellar constituent within OCs, categorised into different luminosity classes, undergoes a unique evolutionary trajectory shaped by factors such as mass, age, and chemical composition. Investigating the physical parameters across diverse evolutionary phases, from giants to main-sequence stars, allows for a comprehensive analysis of the intricate interplay of physical processes governing stellar evolution. The analysis of SED assumes paramount importance in OC studies, offering a means to scrutinise fundamental parameters of member stars originating from the same molecular cloud. Employing SED analysis on the most probable OC members enables the determination of crucial stellar characteristics, including effective tempera-

Corresponding Author: D. C. Dursun **E-mail:** denizcdursun@gmail.com

Submitted: 15.03.2024 • **Revision Requested:** 08.04.2024 • **Last Revision Received:** 16.04.2024 • **Accepted:** 18.04.2024 • **Published Online:** 05.06.2024



This article is licensed under a Creative Commons Attribution-NonCommercial 4.0 International License (CC BY-NC 4.0)

ture (T_{eff}), surface gravity ($\log g$), metallicity ($[\text{Fe}/\text{H}]$), V -band extinction (A_V), distance (d), mass (M), radius (R), and age (t). Acquiring these fundamental physical parameters, particularly mass and radius, is essential for advancing our understanding of stellar evolution. These analyses facilitate an in-depth exploration of the reddening effect on cluster members, shedding light on the influence of interstellar dust and gas.

With the beginning of the *Gaia* era (Gaia Collaboration et al. 2016), high precision of astrometric data has been made available to researchers, enabling accurate analyses for identifying the most likely cluster member stars. By comparing the colour-magnitude diagrams (CMDs) and two-colour diagrams (TCDs) of OCs with theoretical evolutionary models, important parameters such as age, distance, chemical composition and interstellar extinction along the line of sight to the cluster can be determined. One traditional method used for this purpose is main-sequence fitting. This technique is based on the assumption that OCs members share similar characteristics, such as age, distance, and chemical composition, due to their common origin (Carraro et al. 1998; Chen et al. 2003; Joshi 2005; Piskunov et al. 2006; Joshi et al. 2016).

NGC 188 (Melotte 2, MWSC 0074) is an old open cluster that is located in a relatively low contaminated region of the Milky Way, making it an ideal object for observational studies. NGC 188 is located at $\alpha = 00^{\text{h}}47^{\text{m}}20^{\text{s}}.96$ and $\delta = +85^{\circ}15'05''.27$ (J2000.0), corresponding to Galactic coordinates of $l = 122^{\circ}.8368$ and $b = +22^{\circ}.3730$ (Hunt & Reffert 2023). Several research efforts have analysed the main features of this open cluster, as detailed in Table 1. NGC 188 has a wide range of parameters, including ages (t) from 2.63 to 12 Gyr (Demarque & Larson 1964; Hunt & Reffert 2023), metallicities ($[\text{Fe}/\text{H}]$) from -0.08 to 0.60 dex (Spinrad et al. 1970; Hills et al. 2015), colour excess ($E(B-V)$) from 0.025 to 0.50 mag (Sandage 1962; Fornal et al. 2007), and distances (d) from 1445 to 2188 pc (Patenaude 1978; Hills et al. 2015).

Twarog & Anthony-Twarog (1989) compared the ages of NGC 188 and M67 and found that NGC 188 is a slightly older OC, at approximately 6.5 Gyr. They suggested adjustments for reddening and distance modulus to reconcile inconsistencies and remove anomalies, such as the lithium discrepancy. Leonard & Linnell (1992) explored the origins of blue stragglers and contact binaries in M67 and NGC 188, proposing physical stellar collisions and tidal captures as potential mechanisms. The experiments showed that these interactions could explain approximately 10% of the observed objects. Belloni et al. (1998) conducted X-ray observations of M67 and NGC 188, detecting various sources and noting puzzling emissions from specific binaries in M67. They also identified two members in NGC 188, including the FK Com type star D719. Glebbeek & Pols (2008) investigated the detailed evolution of stellar collision products in OCs, with a particular focus on M67 and NGC 188. The authors presented models of merger remnants and compared them with observed blue straggler populations,

indicating recent collision events in M67. In a photometric survey of NGC 188, Song et al. (2023) identified 25 variable stars, including one new variable star, and discussed their characteristics, such as spectral types and classifications, providing insights into the cluster's stellar population.

This study aims to determine the fundamental parameters that define the old open cluster of NGC 188 using advanced analytical techniques, such as isochrone fitting and SED analyses. It is important to acknowledge the potential for parameter degeneracy in analysis processes, which can complicate the investigation. To deal with this challenge, we adopt a rigorous approach by calibrating the distances with trigonometric parallaxes from the *Gaia* Data Release 3 (Gaia DR3, Gaia Collaboration et al. 2023) catalogue and taking advantage of metallicity values from high-resolution spectroscopic data in the literature. These steps aim to minimise parameter degeneracy and provide an accurate determination of the age and other fundamental parameters of the NGC 188 OC.

The subsequent sections of this paper are structured as follows: A description of the astrometric and photometric data of NGC 188 is given in Section 2. In Section 3, the presented methods are used to derive the fundamental parameters of NGC 188. In Section 4, the photometric membership probabilities and structural parameters of the stars in NGC 188 are presented and discussed, followed by the main astrophysical parameters obtained using SED. Finally, Section 5 provides a summary.

2. DATA

2.1. Photometric and Astrometric Data

The photometric and astrometric analyses of NGC 188 utilised data from the *Gaia* DR3 catalogue (DR3, Gaia Collaboration et al. 2023). Astrometric and photometric data were generated based on the equatorial coordinates provided by Hunt & Reffert (2023) ($\langle\alpha, \delta\rangle = (00^{\text{h}}47^{\text{m}}20^{\text{s}}.96, \delta = +85^{\circ}15'05''.27)$). Encompassing the entire field of NGC 188, all stars within a $40'$ radius from the cluster center were considered. Consequently, 17,344 stars falling within the $6 < G(\text{mag}) \leq 23$ mag range were detected. The identification chart of stars in the direction of NGC 188, covering a $40' \times 40'$ field, is illustrated in Figure 1.

2.2. Photometric Completeness Limit and Errors

To precisely determine the structural and astrophysical parameters of the cluster, it is imperative to establish the photometric completeness limit by tallying stars corresponding to G magnitudes. The photometric completeness limit is defined as the magnitude where the number of stars increases with magnitude up to a certain point, beyond which it starts to decrease. For NGC 188, this value, as evident from the histogram in Figure 2, is the photometric completeness limit $G = 20.5$ mag. Stars fainter than this completeness limit were excluded, en-

Table 1. Basic parameters of the NGC 188 open cluster collected from the literature.

$E(B - V)$ (mag)	d (pc)	[Fe/H] (dex)	t (Gyr)	$\langle\mu_\alpha \cos \delta\rangle$ (mas yr ⁻¹)	$\langle\mu_\delta\rangle$ (mas yr ⁻¹)	V_R (km s ⁻¹)	Ref
0.50	1549	–	–	–	–	–	(01)
0.1±0.020	1500	–	–	–	–	-49	(02)
–	–	–	12	–	–	–	(03)
0.18	–	–	5.5	–	–	–	(04)
0.15	–	0.60	–	–	–	–	(05)
0.15	–	–	–	-3.98	-0.65	-49	(06)
0.09	–	–	–	–	–	–	(07)
0.09	1445	–	8	–	–	–	(08)
–	1700	0.00	6	–	–	–	(09)
0.08	–	0.00	10	–	–	–	(10)
0.08	–	–	6.03	–	–	–	(11)
0.12	1995	0.02±0.110	6	–	–	–	(12)
0.03	–	-0.06±0.00	7.5	–	–	–	(13)
0.08	1520	-0.05	7.2	–	–	–	(14)
0.09±0.020	1905	-0.04±0.050	7±0.50	–	–	–	(15)
–	–	0.075±0.050	–	–	–	–	(16)
0.09±0.020	–	0.00	6.8	–	–	–	(17)
0.025±0.005	1700±100	0.00	7.5±0.70	–	–	–	(18)
0.036±0.010	1714±64	0.12	7.5±0.50	–	–	–	(19)
–	2188±100	-0.08±0.003	6.45±0.04	–	–	–	(20)
0.033±0.030	1721±41	0.00	7.08±0.04	–	–	-42.87±0.30	(21)
–	–	0.00	6	–	–	–	(22)
0.075 ± 0.008	–	–	–	-3.000±1.830	-0.370±0.100	–	(23)
–	1864±4	–	–	-2.307±0.139	-0.960±0.146	–	(24)
–	1864±4	–	–	-2.307±0.139	-0.960±0.146	-41.70±0.19	(25)
–	–	0.14±0.003	4.47	-2.310±0.190	-0.960±0.160	-41.50±1.10	(26)
0.068	1698	–	7.08	-2.307±0.139	-0.960±0.146	–	(27)
–	1859±36	0.112±0.020	7.05	-2.302±0.184	-0.955±0.172	-41.602±0.58	(28)
–	1974±20	0.088±0.032	7.08	-2.303±0.182	-0.953±0.167	–	(29)
–	1698	0.088±0.032	7.08	–	–	-42.03±0.05	(30)
–	–	–	–	–	–	-41.64±0.25	(31)
–	1670	0.090±0.020	7.59	–	–	–	(32)
–	1847±6	–	–	-2.335±0.004	-1.024±0.004	-41.70±0.20	(33)
0.074±0.037	1822	–	2.63±1.17	-2.318±0.106	-1.015±0.111	-41.13±0.59	(34)
0.047±0.009	1806±21	-0.030±0.015	7.65±1.00	-2.314±0.048	-1.020±0.045	-41.59±0.14	(35)

(01) Sandage (1962), (02) Greenstein & Keenan (1964), (03) Demarque & Larson (1964), (04) Aizenman et al. (1969), (05) Spinrad et al. (1970), (06) Uggren et al. (1972), (07) McClure & Twarog (1977), (08) Patenaude (1978), (09) Vandenberg (1983), (10) Vandenberg (1983), (11) Janes & Demarque (1983), (12) Caputo et al. (1990), (13) Carraro & Chiosi (1994), (14) Friel (1995), (15) Sarajedini et al. (1999), (16) Worthey & Jowett (2003), (17) Vandenberg & Stetson (2004), (18) Fornal et al. (2007), (19) Wang et al. (2015), (20) Hills et al. (2015), (21) Elsanhoury et al. (2016), (22) Lorenzo-Oliveira et al. (2016), (23) Dias et al. (2014), (24) Cantat-Gaudin et al. (2018), (25) Soubiran et al. (2018), (26) Donor et al. (2018), (27) Cantat-Gaudin & Anders (2020), (28) Dias et al. (2021), (29) Spina et al. (2021), (30) Tarricq et al. (2021), (31) Carrera et al. (2022b), (32) Netopil et al. (2022), (33) Gao & Fang (2022), (34) Hunt & Reffert (2023), (35) This study

sure that they were not considered in subsequent analyses. Photometric inaccuracies reported in *Gaia* DR3 were treated as internal errors, reflecting uncertainties associated with the instrumental magnitudes of celestial bodies. Consequently, the study considered uncertainties in the instrumental magnitudes of stars as internal errors. Mean errors for G magnitudes and $G_{BP} - G_{RP}$ colour indices were computed across the G apparent magnitude interval. The mean errors for G magnitudes along with $G_{BP} - G_{RP}$ colour indices of stars are presented in Table 2 as a function of G magnitudes. The mean internal error for G magnitude and $G_{BP} - G_{RP}$ colour index were determined to be 0.009 and 0.182 mag, respectively.

Table 2. Mean internal photometric errors of NGC 188 for G and $G_{BP} - G_{RP}$ mag in per G magnitude bin.

G (mag)	N	σ_G (mag)	$\sigma_{G_{BP}-G_{RP}}$ (mag)
(06, 14]	487	0.002	0.005
(14, 15]	593	0.002	0.005
(15, 16]	1035	0.002	0.006
(16, 17]	1447	0.002	0.008
(17, 18]	1969	0.003	0.017
(18, 19]	2598	0.003	0.040
(19, 20]	3573	0.004	0.086
(20, 21]	4988	0.009	0.182
(21, 23]	654	0.026	0.297

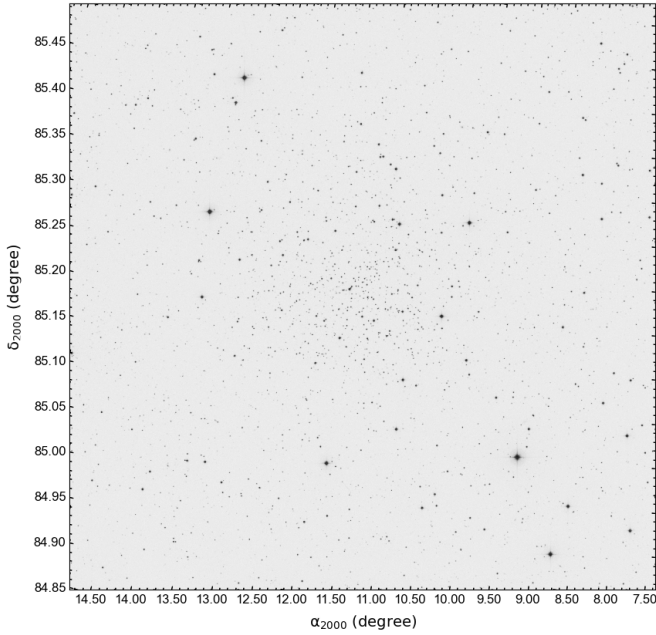


Figure 1. Identification chart of NGC 188 for $40' \times 40'$ region. The up and left directions represent the North and East, respectively.

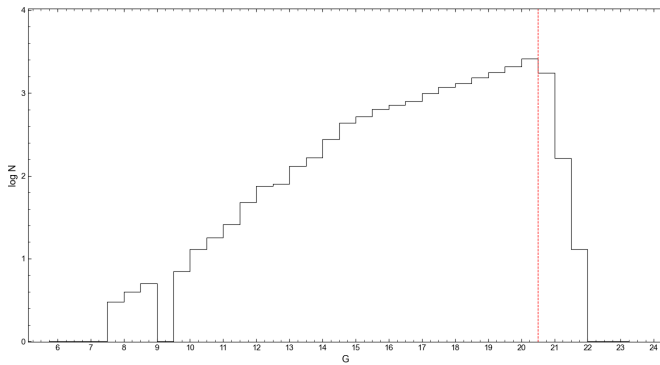


Figure 2. Distribution of the stars in the direction of NGC 188 for G magnitude intervals. The photometric completeness limit is indicated by a red dashed line.

3. METHOD

3.1. Isochrone Fitting

A classical technique employed for determining the fundamental astrophysical parameters of open clusters is the main-sequence fitting method. This method relies on the assumption that members of a star cluster originate from the same molecular cloud and share common properties such as distance, age, and chemical composition. The isochrone-fitting method involves comparison with theoretical isochrones to simultaneously determine the age, metallicity, isochrone distance of the cluster and the best isochrone representing the cluster is shown by fitting over the CMD. The isochrone fitting process entails selecting isochrones with different ages and metallicities that best fit the observed CMD of cluster members. However, this process may introduce parameter degeneracy (King et al. 2005; De Meulenaer et al. 2013; Janes et al. 2014).

To mitigate the potential degeneracy in the analyses, we im-

posed constraints on the distance and metallicity parameters of the cluster. The distance was chosen to be proximate to the value calculated from the mean trigonometric parallax of NGC 188. Additionally, the metallicity of the cluster was derived from a literature study that provided high-resolution spectroscopic data. This approach was adopted to minimise parameter degeneracy in cluster analyses (cf. Yontan et al. 2015, 2019; Yontan 2023).

3.2. Spectral Energy Distribution

In astrophysics, spectral energy distribution (SED) analysis aims to determine the physical properties of stars and other astronomical objects by examining the wavelength and intensity distributions of the light emitted by them across the electromagnetic spectrum (Oke 1974; Adams et al. 1987; Robitaille et al. 2006; Yadav et al. 2024). SED requires observational fluxes with different filters to measure the object over a wide range of the electromagnetic spectrum. These observed fluxes are then analyzed to determine the astrophysical parameters of the object by comparison with theoretical models. SED is assisted by computer simulations and utilizes optimization techniques to effectively match the properties of the astronomical object while considering the complexities of the observed data. In particular, SED analysis determines the astrophysical parameters (T_{eff} , $\log g$, $[\text{Fe}/\text{H}]$, A_v , d , M , R , and t) of stars. This technique is used to understand various astrophysical topics, such as star formation and evolution, Galactic and cosmic evolution processes, and galaxy formation. Furthermore, SED analysis of member stars in open clusters was used to determine the age, chemical composition, and evolutionary state of the star clusters.

For the SED method, we utilised the SpectrAl eneRgy dIstribution bAyesian moDel averagiNg fittEr (ARIADNE; Vines & Jenkins 2022) code for member stars with photometric data points covering a wavelength range from UV to IR. ARIADNE has been designed with a focus on speed, user-friendliness, and versatility. It employs a Bayesian framework to estimate physical characteristics and associated uncertainties efficiently. The platform is flexible and can accommodate various stellar evolution models, star formation scenarios, dust attenuation profiles, and inclusion of nebular emissions. Furthermore, it provides a χ^2 minimization feature through ARIADNE, facilitating straightforward comparisons with existing research. ARIADNE is particularly well-suited for investigating stellar clusters. More than 20 photometric data points within the wavelength range $0.1 < \lambda < 5 \mu\text{m}$ of the electromagnetic spectrum are used to fit the SED of stars. ARIADNE determines the astrophysical parameters of single stars. For the synthetic models included in ARIADNE, the three models with the widest effective temperature, surface gravity, and metallicity parameter range ($2300 < T_{\text{eff}}(\text{K}) < 12000$, $0 < \log g(\text{cgs}) < 6$, and $-2.5 < [\text{Fe}/\text{H}](\text{dex}) < 1$) PHOENIX v2 (Husser et al. 2013),

BT-Cond (Allard et al. 2012), Castelli and Kurucz (Castelli & Kurucz 2003) were used.

4. RESULTS

4.1. Structural Parameters

Radial Density Profile (RDP) analysis is utilized to determine the spatial extent of NGC 188 and obtain its structural parameters. The cluster area is divided into numerous concentric rings, considering the central coordinates provided by Hunt & Reffert (2023) through *Gaia* DR3 data within a 40×40 arcmin² region. To compute the stellar density ($\rho(r)$) of NGC 188, stars within the $G \leq 20.5$ mag completeness limit are considered, and the equation $R_i = N_i/A_i$ is applied for each i^{th} ring, where N_i and A_i denote the number of stars falling into a ring and the area of the particular ring, respectively. The calculated stellar densities were then plotted against the distance from the center of NGC 188 and an empirical King profile King (1962) fitted which is defined as $\rho(r) = f_{\text{bg}} + f_0 / (1 + (r/r_c)^2)$. Here, r , r_c , f_{bg} and f_0 represent angular radius, core radius, background stellar density and central stellar density, respectively.

The RDP fitting method employed the χ^2 minimisation technique, and the best-fit solution of the RDP is depicted with a black solid line in Figure 3. Examining the figure reveals that the stellar density of NGC 188 peaks around the center of the cluster, gradually decreasing radially as it moves away from the cluster center. The RDP flattens and merges with the background star density at a specific point known as the lim-

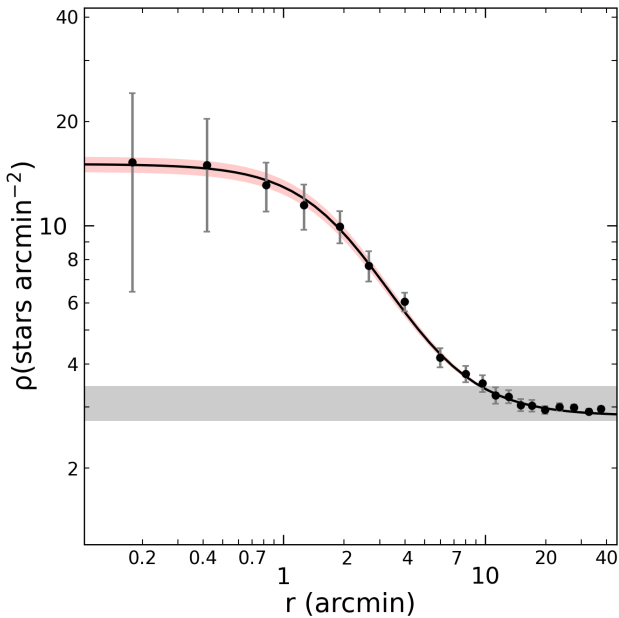


Figure 3. The RDP of King (1962) for NGC 188. Stellar density errors were determined from Poisson statistics $1/\sqrt{N}$, where N is the number of stars. The fitted black curve and horizontal grey shaded area show the best-fitted RDP and background stellar density, respectively. Also, red-shaded area indicates the 1σ uncertainty of the King fit.

iting radius. In this study, we estimated this radius through visual inspection and adopted it as $15'$ (Figure 3). Stars located within this observational limiting radius were utilised in further analyses. To confirm the reliability of the observed limiting radii ($r_{\text{lim}}^{\text{obs}}$) by the theoretical approach, we used the equation given by Bukowiecki et al. (2011) that is expressed by $r_{\text{lim}}^{\text{teo}} = r_c \times ((f_0 / 3\sigma_{\text{bg}}) - 1)^{1/2}$. Considering this equation, the theoretical limiting radius is calculated as $r_{\text{lim}}^{\text{teo}} = 14'.8$. It is clear that theoretical and observed limiting radius values are in good agreement. The central and background stellar densities, as well as the core radius of NGC 188 are obtained as $f_0 = 12.229 \pm 0.768$ stars arcmin⁻², $f_{\text{bg}} = 2.832 \pm 0.356$ stars arcmin⁻² and $r_c = 2'.183 \pm 0'.304$, respectively.

4.2. Membership Probabilities and Astrometric Analysis

To accurately determine the astrophysical parameters of Open Clusters (OCs), it is crucial to distinguish the physical members of the cluster from the field stars, given the significant impact of field stars on OCs located in the Galactic plane. The members of an open cluster share the same origin, arising from the collapse of a common molecular cloud. Consequently, the proper motion vectors of cluster member stars exhibit a consistent direction in space, and their proper motion values closely align with the mean proper motions of the cluster. This congruence serves as a valuable tool for effectively separating field stars from cluster stars.

The Unsupervised Photometric Membership Assignment in Stellar Clusters (UPMASK) method was employed for membership analyses, utilising astrometric parameters, including equatorial coordinates (α , δ), proper motion components ($\mu_\alpha \cos \delta$, μ_δ), and trigonometric parallaxes (ϖ), along with their uncertainties, from the *Gaia* DR3 catalogue of NGC 188. UPMASK relies on a machine-learning clustering algorithm, specifically k -means clustering, to identify similar groups of stars based on their proper motion components and trigonometric parallaxes. This approach facilitates the statistical determination of the members within the open cluster. The membership probability histogram is shown in Figure 4. Stars with membership probabilities $P \geq 0.5$ were considered potential cluster members.

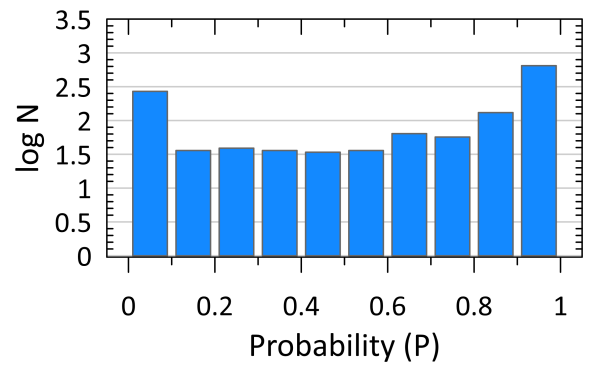


Figure 4. Distribution of cluster membership probabilities for the stars toward NGC 188.

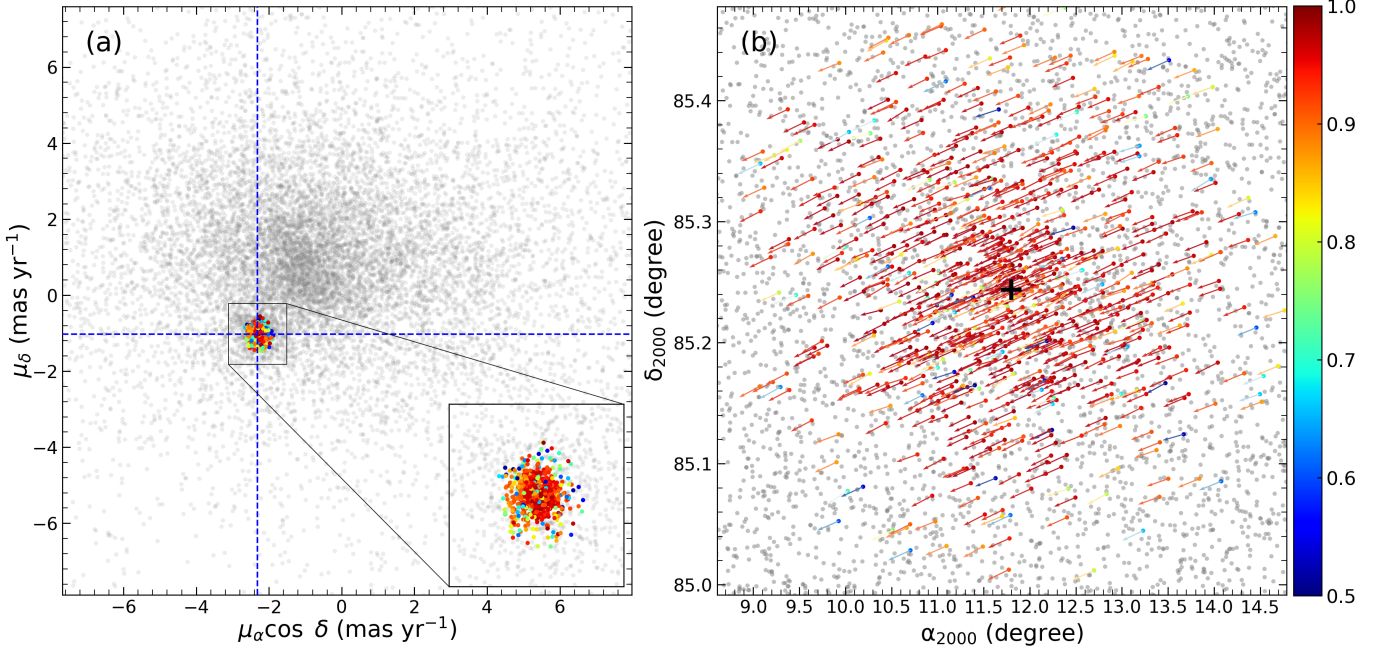


Figure 5. Vector Point Diagram (a) and proper-motion velocity vectors (b) of NGC 188. The colour scale in the right panel denotes membership probabilities over than 0.5. In panel (a), the magnified boxes reveal regions with a high concentration of member stars in the VPDs, and the mean proper motion values are indicated by the intersection of blue dashed lines. The center of equatorial coordinates of NGC 188 are marked by black cross-hairs in panel (b).

Through astrometric calculations and considering photometric limitations, 868 stars were identified as the most probable physical members of NGC 188. These stars not only have membership probabilities $P \geq 0.5$ but are also within the observational limiting radius ($r_{\text{lim}}^{\text{obs}}$) and satisfy the photometric completeness limit ($G \leq 20.5$ mag).

We computed the mean proper-motion components of the cluster for stars with membership probabilities $P \geq 0.5$ and illustrated their distribution throughout the cluster using the vector point diagram (VPD) in Figure 5. The cluster occupies a distinct region that is relatively separated from field stars. The mean values of the proper-motion components specific to the cluster are represented at the intersection of the blue dashed lines. The calculated mean proper-motion components for NGC 188 are $(\mu_{\alpha} \cos \delta, \mu_{\delta}) = (-2.314 \pm 0.002, -1.022 \pm 0.002)$ mas yr $^{-1}$, aligning well with recent studies in the literature (e.g., Cantat-Gaudin & Anders 2020; Dias et al. 2021; Hunt & Reffert 2023).

While trigonometric parallax measurements represent the most precise method for determining stellar distances, the existence of errors at the zero point in astrometric measurements introduces considerable uncertainty, particularly in distance determinations for distant objects. Recent studies (e.g., Lindegren et al. 2021; Huang et al. 2021; Riess et al. 2021; Zinn 2021) have proposed zero-point corrections utilising a multitude of objects with trigonometric measurements in the *Gaia* EDR3/DR3 database (Gaia Collaboration et al. 2021, 2023). Given that NGC 188 is situated at a distance of approximately 1.8 kpc (Dias et al. 2021; Hunt & Reffert 2023), we applied

a zero-point correction to the trigonometric parallaxes (ϖ) of the most likely cluster members ($P \geq 0.5$). This correction involved considering the value $\varpi_{\text{ZP}} = -0.025$ mas, as proposed by Lindegren et al. (2021), and employing the relation $\varpi_0 = \varpi - \varpi_{\text{ZP}}$ for each member star.

4.3. Astrophysical Parameters

4.3.1. Isochrone Fitting Method

To calculate the mean trigonometric parallax of NGC 188, we focused on stars with a relative parallax error smaller than 0.05. A histogram of the trigonometric parallaxes for the most likely members was plotted, and a Gaussian function was fitted to determine the mean trigonometric parallax of the cluster, as illustrated in Figure 6. The mean trigonometric parallax of NGC 188 was determined as $\varpi = 0.550 \pm 0.023$ mas. The linear distance of the cluster was computed using the equation $d(\text{pc}) = 1000/\varpi$ (mas). Consequently, the transformed trigonometric parallax yielded an estimated distance of $d_{\varpi} = 1818 \pm 76$ pc. We found this result to be in good agreement with values reported in the literature (Sarajedini et al. 1999; Cantat-Gaudin et al. 2018).

In determining the fundamental astrophysical parameters such as reddening, age, and distance of OCs, CMDs can be used as an important tool. In this study, most likely stars were projected on the $G \times (G_{\text{BP}} - G_{\text{RP}})$ CMD with their membership probabilities. The mean metallicity of NGC 188 was taken directly from literature to avoid parameter degeneration. We adopted the value of Casamiquela et al. (2021) for the mean

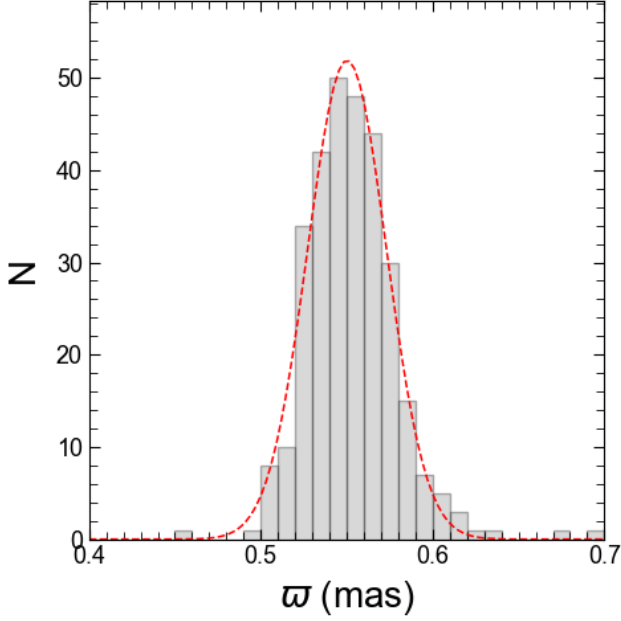


Figure 6. *Gaia* DR3-based trigonometric parallax histogram constructed from the most likely member stars of NGC 188. The Gaussian fit applied to the distributions is represented by the red-dashed curve.

metallicity of the NGC 188 as -0.030 ± 0.015 dex by analysing the high-resolution spectra of four member stars. In order to select the best-fit isochrone and obtain the astrophysical parameters, adopted metallicity ($[\text{Fe}/\text{H}] = -0.030 \pm 0.015$ dex) is converted to the mass fraction z by using the equation given by Bovy¹ that are available for PARSEC models (Bressan et al. 2012).

$$z_x = 10^{[\text{Fe}/\text{H}] + \log\left(\frac{z_\odot}{1 - 0.248 - 2.78 \times z_\odot}\right)} \quad (1)$$

and

$$z = \frac{(z_x - 0.2485 \times z_x)}{(2.78 \times z_x + 1)}. \quad (2)$$

where z_x and z_\odot are intermediate values where solar metallicity z_\odot was adopted as 0.0152 (Bressan et al. 2012). Using these equations, we derived the mass fraction value that corresponds to $[\text{Fe}/\text{H}] = -0.030 \pm 0.015$ dex as $z = 0.0142$.

By keeping metallicity constant and paying attention to the distance derived from the trigonometric parallaxes, we fitted theoretical PARSEC isochrones (Bressan et al. 2012) to the CMD and derived age, distance modulus, and reddening simultaneously. The fitting procedure was performed considering the distribution of most likely ($P \geq 0.5$) main-sequence, turn-off and giant members on cluster CMD. The best fitted isochrones of different ages ($t = 7.55, 7.65$ and 7.75 Gyr) scaled to the mass fraction $z = 0.0142$ with the distribution of the most likely members on the cluster's $G \times (G_{\text{BP}} - G_{\text{RP}})$ CMD is

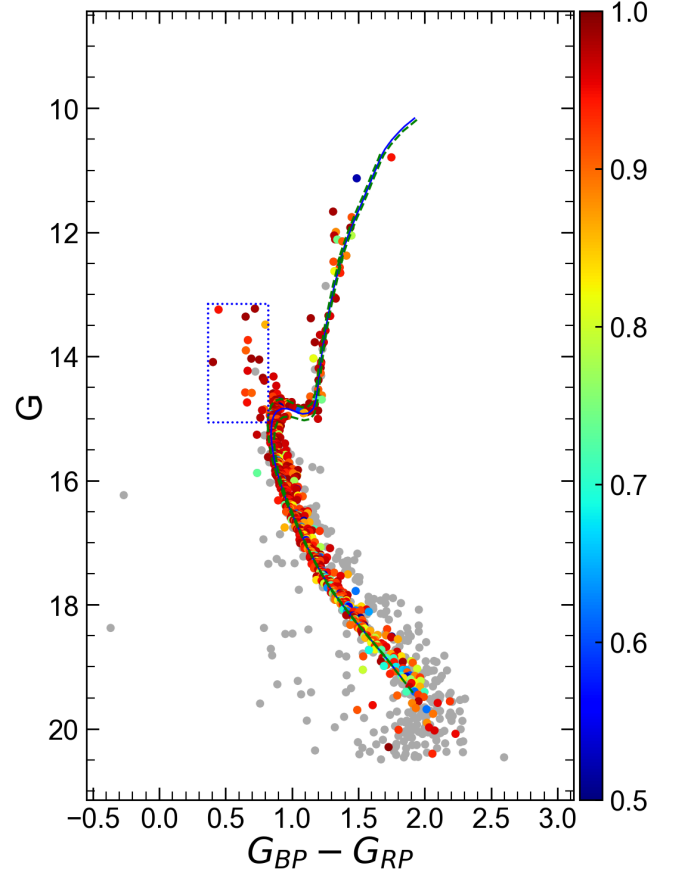


Figure 7. CMD of the NGC 188. Different colour scales and colourbar show the membership probabilities of stars with $P \geq 0.5$. Stars with probabilities $P < 0.5$ are demonstrated with filled grey circles. The best solution of the fitted isochrones and their errors are inferred as blue and purple lines, respectively. The age of the blue-lined isochrone matches with 7.65 ± 1.00 Gyr for the cluster. The BSs are marked within the blue dashed box.

shown in Figure 7. The best fitted isochrones imply that the morphology of the cluster in CMD was selected as $t = 7.65 \pm 1.00$ Gyr. The estimated age is comparable with the values of Bossini et al. (2019) and Cantat-Gaudin & Anders (2020).

The colour excess and isochrone distance values of NGC 188 corresponding to the isochrone age at $z = 0.0142$ were obtained as $E(G_{\text{BP}} - G_{\text{RP}}) = 0.066 \pm 0.012$ mag and $d_{\text{iso}} = 1806 \pm 21$ pc, respectively. As can be seen from the (see Table 1), colour excess and isochrone distances are consistent with most of the studies presented by different researchers. The errors in distance modulus and isochrone distance were obtained from the expression of Carraro et al. (2017), which takes into consideration the photometric measurements and colour excess with their uncertainties. To perform more precise comparisons with literature studies, $E(G_{\text{BP}} - G_{\text{RP}})$ was converted to the *UBV*-based colour excess $E(B - V)$ value. For this, we applied the equation of $E(G_{\text{BP}} - G_{\text{RP}}) = 1.41 \times E(B - V)$ given by Sun et al. (2021) and obtained the colour excess as $E(B - V) = 0.047 \pm 0.009$ mag. This result is in good agreement with the values given by Hunt & Reffert (2023), Cantat-Gaudin & Anders (2020), and Gao & Fang (2022) within the errors (see Table 1). Isochrone

¹ <https://github.com/jobovy/isodist/blob/master/isodist/Isochrone.py>

distance of NGC 188 derived from the isochrone fitting method agrees with most studies performed by different researchers (see Table 1) as well as the trigonometric parallax distance, $d_{\varpi} = 1818 \pm 76$ pc, obtained in this study.

4.3.2. SED Analysis

To conduct Spectral Energy Distribution (SED) analyses for the most likely member stars of NGC 188, flux values measured in various filters across a broad range of the electromagnetic spectrum are essential. As outlined in the previous sections, the number of stars with cluster membership $P \geq 0.5$ was established as 868 (see Sec. 4.2). Since SED analyses focus on determining the basic astrophysical parameters of individual stars, it is necessary to exclude stars in double, multiple, and variable categories among those with high cluster membership from the statistics. To achieve this, the equatorial coordinates and *Gaia* DR3 data of the 868 stars with high cluster membership were considered, and their stellar types and brightness changes were queried through the SIMBAD database.

The query results revealed that 93 stars in the list were classified as double or multiple, 10 were identified as variable stars, and 348 stars lacked sufficient brightness data for SED analysis. Consequently, these stars were excluded from the statistics. The *Gaia* archive (Gaia Collaboration et al. 2021, 2023) includes a Renormalised Unit Weight Error (RUWE) value for each source. This parameter indicates the quality of the astrometric solution for a given source in *Gaia*. Ideally, the RUWE value should be around 1.0 for sources where the single-star model fits the astrometric observations well. A value significantly greater than 1.0, such as >1.4 , could indicate that the source is non-single or otherwise problematic for the astrometric solution (Fitton et al. 2022). One giant, one subgiant and three dwarfs were excluded from the analysis after checking the RUWE values of the cluster members. SED analyses were successfully conducted for the remaining 412 single cluster member stars using the (ARIADNE; Vines & Jenkins 2022), and their basic astrophysical parameters were determined.

The outcomes of the SED analyses for three stars selected from different luminosity classes, along with the cornerplots illustrating the agreement of the main astrophysical parameters, are presented in Figure 8. Among the three analyzed stars, the evolved ones exhibited the best fit with the PHOENIX v2 model (Husser et al. 2013), while the dwarf star demonstrated the best fit with the Castelli and Kurucz model (Castelli & Kurucz 2003). This agreement is evident from the residual distributions in the bottom panel of the SED distributions for each star. Additionally, the cornerplots in the right panel of the SED distributions for each star indicate the absence of degeneracy between the parameters, with uncertainties at acceptable levels.

To assess the precision of the derived basic astrophysical parameters, we refer to the study by (Jacobson et al. 2011), who conducted spectral analyses of NGC 188. In their work,

Jacobson et al. (2011) analyzed the chemical abundances of evolved stars in 10 OCs using spectra obtained with the WIYN 3.5m telescope. Examining 31 stars in NGC 188, (Jacobson et al. 2011) identified 12 member stars that are common with the comparison conducted in our study. Among these stars, there are 11 red giants and a subgiant star. The star depicted in the panel of Figure 8a was analyzed in both studies. A comparison of the 12 stars, for which model atmosphere parameters (T_{eff} , $\log g$, and $[\text{Fe}/\text{H}]$) were determined using spectral and SED analysis, is presented in Figure 9.

In the analyses, the differences in effective temperature, surface gravity, and metal abundance obtained from the two studies, along with the standard deviations of these differences, were calculated as $\langle \Delta T_{\text{eff}} \rangle = 44$ K, $\langle \Delta \log g \rangle = 0.08$ cgs, and $\langle \Delta [\text{Fe}/\text{H}] \rangle = 0.01$ dex, respectively. The calculated mean differences and standard deviation values being sufficiently small provide crucial evidence that the model atmosphere parameters determined in the two studies are compatible with each other.

With the basic astrophysical parameters of the 412 SED analysed stars in hand, the absolute magnitudes and reddening-free colour indices of the stars were utilised to ascertain the luminosity classes. This was achieved by creating a more sensitive CMD. The distance relation used to determine the absolute magnitude (M_G) is given as follows:

$$M_G = G_0 - 5 \log d + 5, \quad (3)$$

where G_0 is the de-extinction apparent magnitude of the star and d is the distance determined from the SED analysis. Since SED analysis calculate the extinction value in the V band, selective absorption coefficients (A_{λ}/A_V) of 0.83627, 1.08337 and 0.63439 were used for the G , G_{BP} and G_{RP} bands, respectively, as defined by the *Gaia* photometric system (Cardelli et al. 1989). The following equations were taken into account in the de-extinction of magnitude:

$$\begin{aligned} G_0 &= G - 0.83627 \times A_V, \\ (G_{\text{BP}})_0 &= G_{\text{BP}} - 1.08337 \times A_V, \\ (G_{\text{RP}})_0 &= G_{\text{RP}} - 0.63439 \times A_V, \end{aligned} \quad (4)$$

After calculating the absolute magnitudes and de-reddened colour indices of the cluster member stars, $M_G \times (G_{\text{BP}} - G_{\text{RP}})_0$ diagram was generated Figure 10. As can be seen from the Figure 10, the morphology of the cluster is very distinct. The red giant arm of the cluster has an absolute magnitude of $-1 < M_G \text{ (mag)} \leq 3$ and a colour index $(G_{\text{BP}} - G_{\text{RP}})_0 > 0.95$ mag, while the lower giant arm has an absolute magnitude of $3 < M_G \text{ (mag)} \leq 3.75$ and a colour index of $0.95 < (G_{\text{BP}} - G_{\text{RP}})_0 \text{ (mag)} \leq 1.30$. The remaining stars on the CMD are classified as dwarf stars.

To analyse the differences between the basic astrophysical parameters of the member stars in different luminosity class of the NGC 188, the ranges of the luminosity classes above were taken into account. The parameter ranges of the stars in each luminosity classes and all member stars analysed by SED are

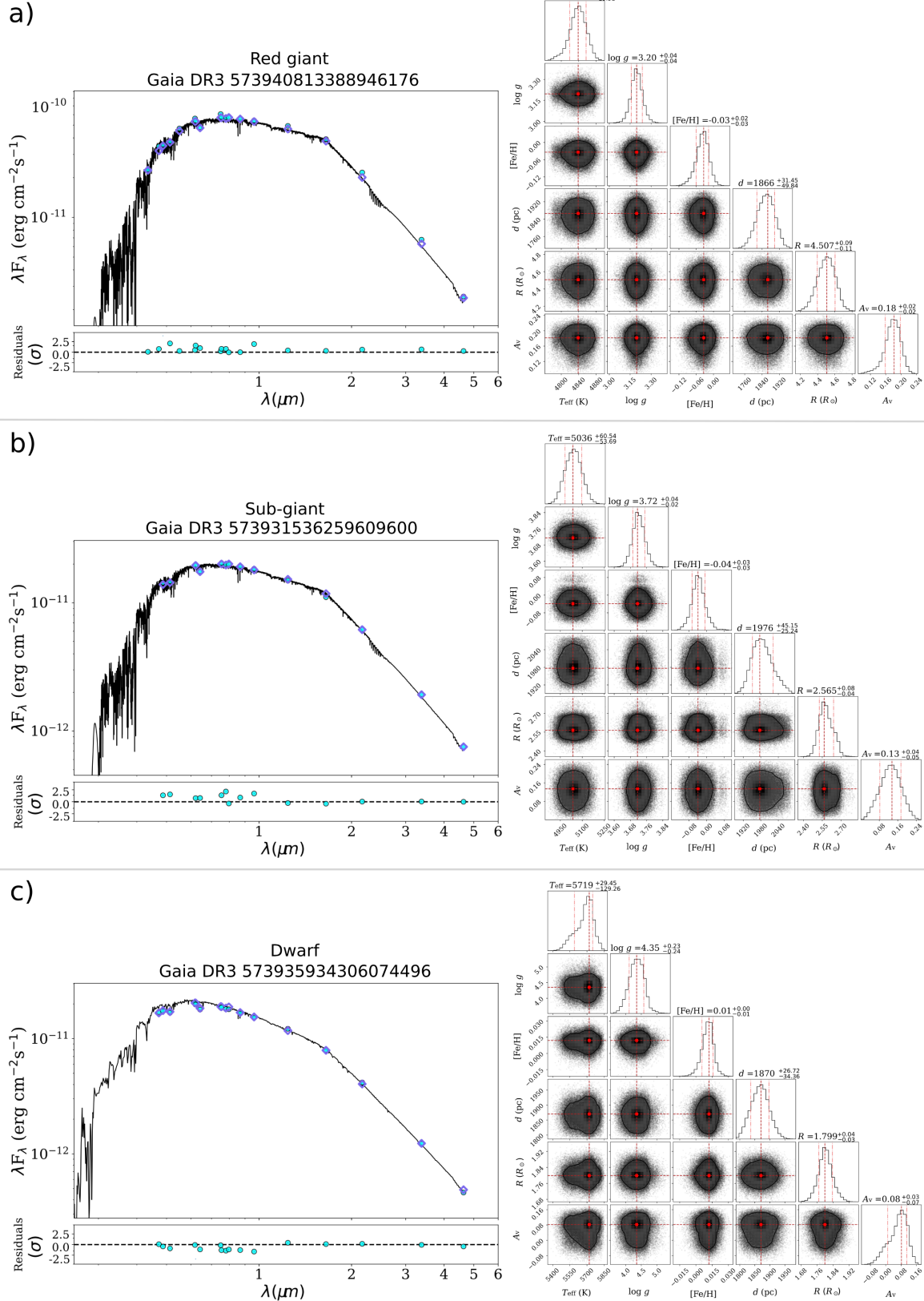


Figure 8. SED diagrams (left panels) with the best astrophysical parameter solution histograms and distributions (right panels) for three member stars with different luminosity classes. Panels (a), (b) and (c) show the SED analyses for red giant, sub-giant and dwarf member star, respectively.

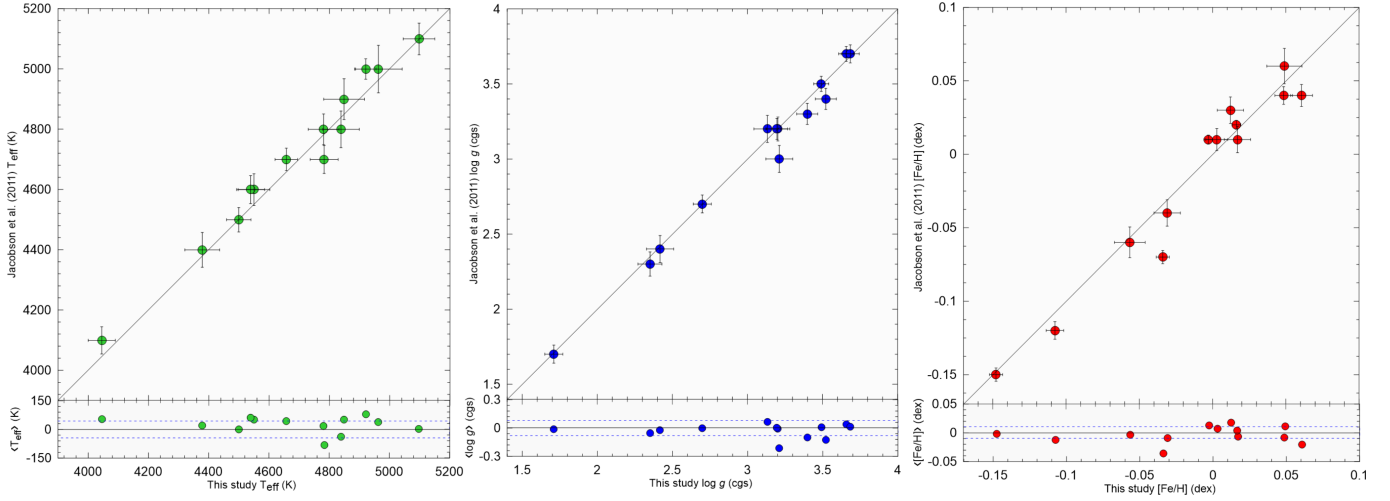


Figure 9. The comparison of the astrophysical parameters of the 12 stars spectral analysed by [Jacobson et al. \(2011\)](#) as members of NGC 188 with the results in this study.

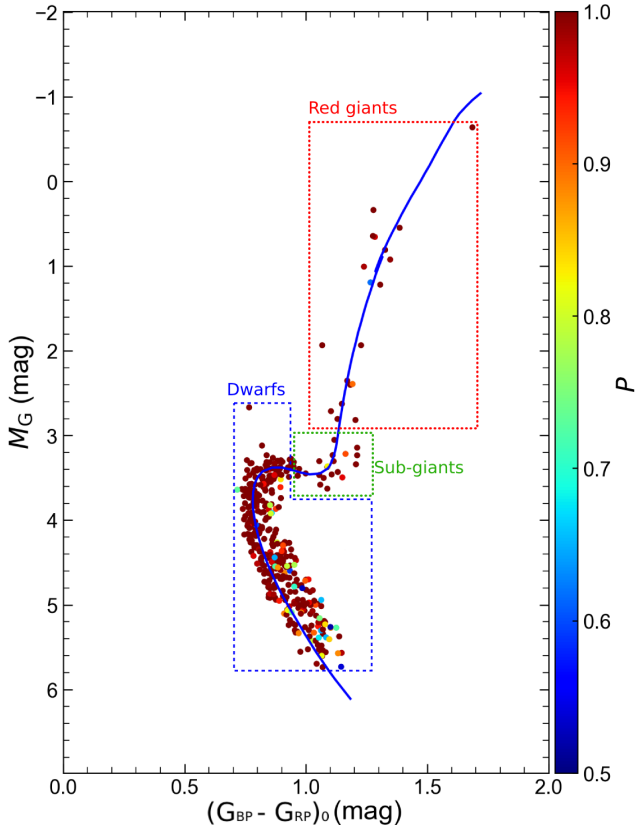


Figure 10. The diagram of $M_G \times G_{(BP-RP)_0}$ for NGC 188. Different colours and colour bar scales indicate the membership probabilities of stars with $P \geq 0.5$. The age of the blue line isochrone matches the age determined by the SED analysis for the cluster 412 members. The red-dashed area denotes red giant stars, the purple dashed area signifies sub-giant stars, and the blue dashed area represents dwarf stars.

listed in Table 3. As can be seen from the bottom row of Table 3, the numbers of red giant, sub-giant, and dwarf stars are 20, 18, and 374, respectively.

When the effective temperature and surface gravity obtained

by SED analysis are analysed according to the luminosity classes, they are compatible with the stellar evolution models. Evaluating the metal abundance variations across luminosity classes, sub-giant stars exhibit the smallest variation range with $\Delta[\text{Fe}/\text{H}] = 0.09$ dex, while dwarf stars present the largest variation range with $\Delta[\text{Fe}/\text{H}] = 0.28$ dex. Analysing dwarf stars based on their unit absolute luminosity ranges reveals an increase in the range of metal abundances from bright to faint magnitudes. This phenomenon may be attributed to the decreased sensitivity of faint stars in SED analyses.

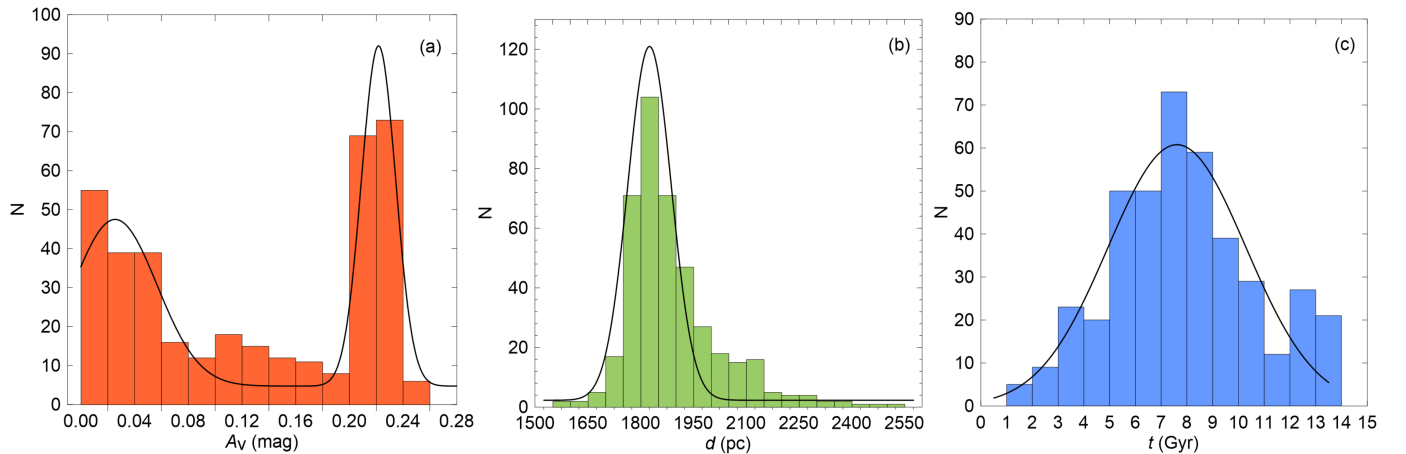
Considering the V -band extinction of the SED-analysed cluster member stars, a considerable variation is observed, ranging from 0 to 0.25 mag. This significant variation in extinction is evident across all luminosity classes, indicating the presence of differential reddening in the NGC 188 region. Similarly, the distances of SED-analysed cluster member stars range from 1562 to 2751 pc, with smaller ranges for evolved stars and larger ranges for dwarf stars. This discrepancy is attributed to the relatively decreased probability of cluster membership for fainter dwarf stars, leading to the inclusion of some field stars in the calculations.

Examining the masses of cluster member stars calculated using MESA Isochrones and Stellar Tracks (MIST; [Dotter 2016](#)) evolution models as a result of SED analyses, the range is found to be between 0.60 and 1.36 M_\odot . Evolved stars, as expected, exhibit a range of approximately 0.35 M_\odot , with the most massive stars falling within this group. Age determinations of the cluster member stars reveal a range between 1.11 and 13.39 Gyr, with dwarf stars exhibiting a large age range consistent with their position in the main-sequence band.

The most uncertain parameters used for age determination are extinction/colour-excess and distances. The histograms of the V -band extinction, distance, and age parameters obtained from the SED analyses of the member stars in NGC 188 are shown in Figure 11a. As seen in Table 3, the extinction values of the stars

Table 3. Parameters and ranges of values obtained from the best-fit SEDs for 412 member stars of the NGC 188.

Parameter	Red giants	Sub-giants	Dwarfs	All
T_{eff} (K)	[4044, 4963]	[4803, 5507]	[4085, 6075]	[4044, 6075]
$\log g$ (cgs)	[1.50, 3.72]	[3.40, 3.82]	[3.63, 5.61]	[1.50, 5.61]
[Fe/H] (dex)	[-0.11, 0.06]	[-0.07, 0.02]	[-0.09, 0.18]	[-0.11, 0.18]
A_V (mag)	[0.00, 0.25]	[0.01, 0.18]	[0.00, 0.25]	[0.00, 0.25]
d (pc)	[1766, 1947]	[1776, 2036]	[1562, 2751]	[1562, 2751]
M (M_{\odot})	[0.97, 1.36]	[0.97, 1.18]	[0.60, 1.24]	[0.60, 1.36]
R (R_{\odot})	[3.52, 31.06]	[2.08, 3.28]	[0.82, 2.56]	[0.82, 31.06]
t (Gyr)	[3.26, 10.54]	[5.66, 9.18]	[1.11, 13.39]	[1.11, 13.39]
N	20	18	374	412

**Figure 11.** Histograms representing the distribution of A_V , distance (d), and age (t) values of the 412 members of NGC 188 obtained by SED analysis. Black lines through the distributions indicate the standard Gaussian distribution.

were found to be in a wide range between 0 and 0.25 mag and it was suggested that a differential reddening might be possible. Indeed, when the V -band extinction histogram is analysed, a bi-modal distribution is found (Figure 11a). A bimodal fit was made to this distribution and the mode values were calculated to be $A_{V,1} = 0.026 \pm 0.025$ mag and $A_{V,2} = 0.223 \pm 0.017$ mag. This is evidence of differential extinction. When the distance histogram of all stars in the sample is analysed, it shows a distribution that can almost be described by a Gaussian distribution (Figure 11b). When a Gaussian fit is applied to the distribution, the most likely distance of the cluster is found to be 1855 ± 6 pc. Similarly, the age histogram of all stars is expressed by a Gaussian distribution and the most likely age of the cluster is calculated as 7.61 ± 0.23 Gyr (Figure 11c).

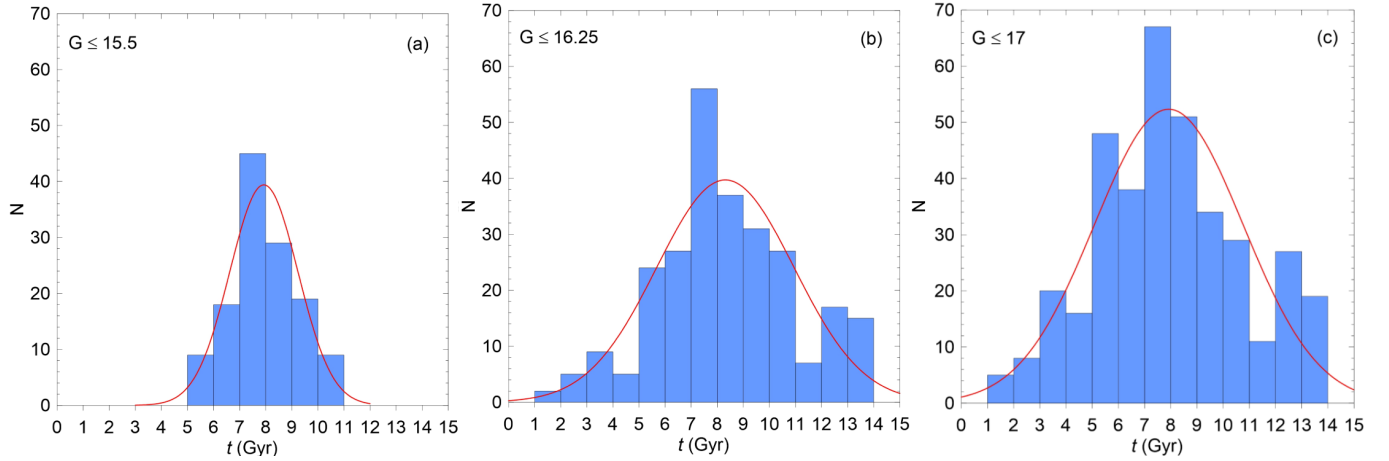
While the values of the extinction and distance parameters obtained from the SED analyses are concentrated in a narrow range, the range of the calculated ages is quite wide (Figure 11). Since the stars in this study are members of open clusters, their extinction, distances and ages are expected to be within a narrow range. However, the distribution of ages calculated in the analyses is wider than expected. This may be due to the fact that the stars used in the SED analyses are in a wide range of apparent sizes. Considering the increase in uncertainties in the

results of the SED analyses of faint stars, the ages were recalculated by dividing the sample of stars studied into three different subgroups in the $G \leq 15.5$, $G \leq 16.25$, and $G \leq 17$ mag intervals. The results are given in Table 4 and the age histograms at different apparent magnitude limits are shown in (Figure 12). Analysis of the histograms in Figure 12 shows that the mode values of the ages are very close in all three histograms, but the age distribution widens when faint stars are included in the calculations. This shows that the parameters obtained from SED analysis should be carefully evaluated, especially in open cluster studies, as fainter luminosities are included in the analyses.

Table 4 presents the median values of metal abundances, V -band extinction values, distance, and age for stars in different luminosity classes along with their errors. The last row of Table 4 summarises the median values calculated for 412 stars in NGC 188. The mean metal abundance is $\langle [\text{Fe}/\text{H}] \rangle = 0.00 \pm 0.03$ dex, the mean V -band extinction value is $\langle A_V \rangle = 0.11 \pm 0.09$ mag, the average distance is $\langle d \rangle = 1854 \pm 148$ pc, and the mean age is $\langle t \rangle = 7.78 \pm 0.23$ Gyr. Fitting the appropriate PARSEC isochrones to the CMD in Figure 10 by considering the values $[\text{Fe}/\text{H}]$, A_V , d , and t from the last row of Table 4 reveals precise representation of the entire CMD morphology.

Table 4. Mean values and errors of metallicity ($[Fe/H]$), V -band extinction (A_V), distance (d) and age (t) obtained from SED analysis of NGC 188 member stars according to luminosity class.

Region	N	$[Fe/H]$ (dex)	A_V (mag)	d (pc)	t (Gyr)
Red giants	20	-0.02 ± 0.04	0.14 ± 0.06	1841 ± 45	6.94 ± 0.45
Sub-giants	18	-0.03 ± 0.02	0.14 ± 0.05	1880 ± 67	6.93 ± 0.26
Dwarfs ($G \leq 15.5$)	129	0.01 ± 0.03	0.10 ± 0.09	1870 ± 95	7.84 ± 0.13
($G \leq 16.25$)	262	0.00 ± 0.03	0.11 ± 0.09	1852 ± 127	8.10 ± 0.24
($G \leq 17$)	374	0.00 ± 0.03	0.09 ± 0.10	1855 ± 154	7.81 ± 0.30
All	412	0.00 ± 0.03	0.11 ± 0.09	1854 ± 148	7.78 ± 0.23


Figure 12. Age histograms of main-sequence stars in three different G apparent-magnitude ranges: $G \leq 15.5$ (a), $G \leq 16.25$ (b), and $G \leq 17$ mag. Red lines through the distributions indicate the standard Gaussian distribution.

Comparing the median distance and age parameters of cluster member stars, it is observed that the results align closely with the values calculated with the Gaussian curve. However, the median V -band extinction obtained from the SED analysis does not exactly agree due to the presence of differential extinction in NGC 188.

To scrutinise the differential extinction within the cluster region more thoroughly, we contoured the V -band extinction values calculated from SED analysis for the 412 stars with high membership in the open cluster NGC 188, considering their positions in equatorial coordinates (Figure 13). Notably, the V -band extinctions in the upper right and lower right quadrants of the cluster center exhibit significant differences from those in the upper left and lower left quadrants. The analyses of V -band extinction, progressing in a clockwise direction, yield $\langle A_V \rangle = 0.171$ mag in region I, $\langle A_V \rangle = 0.042$ mag in region II, $\langle A_V \rangle = 0.175$ mag in region III, and $\langle A_V \rangle = 0.045$ mag in region IV. This observation underscores that stars with smaller right ascension values in the open cluster NGC 188 tend to have larger A_V values.

4.4. Blue Straggler Stars

Blue Straggler Stars (BSSs) found within open clusters deviate from the typical ageing trajectory, displaying characteristics that make them appear younger and bluer than to their counterparts in the surrounding region. Unlike the majority of stars in open clusters that follow established evolutionary pathways, BSSs challenge these norms within the cluster environment. The primary mechanisms contributing to BSS formation involve interactions within binary star systems and stellar collisions occurring in the dense cluster environment (Zinn & Dahn 1976; Hills & Day 1976). Theoretical frameworks propose mass gain through stellar collisions, inner binary mergers, or mass transfer during red giant phases, and ongoing research continues to explore these mechanisms (Webbink 1976; Leonard 1989). In Figure 7, the blue box highlights 19 stars with cluster membership $P \geq 0.5$ located on the blue side of the cluster's turn-off point, identifying them as high-probability BSSs in NGC 188.

In Rain et al. (2021), 22 BSSs were identified using *Gaia* DR2 (Gaia Collaboration et al. 2018) photometric and astrometric data. Since the membership analyses in this study are based on *Gaia* DR3 data, and we considered stars within the limiting

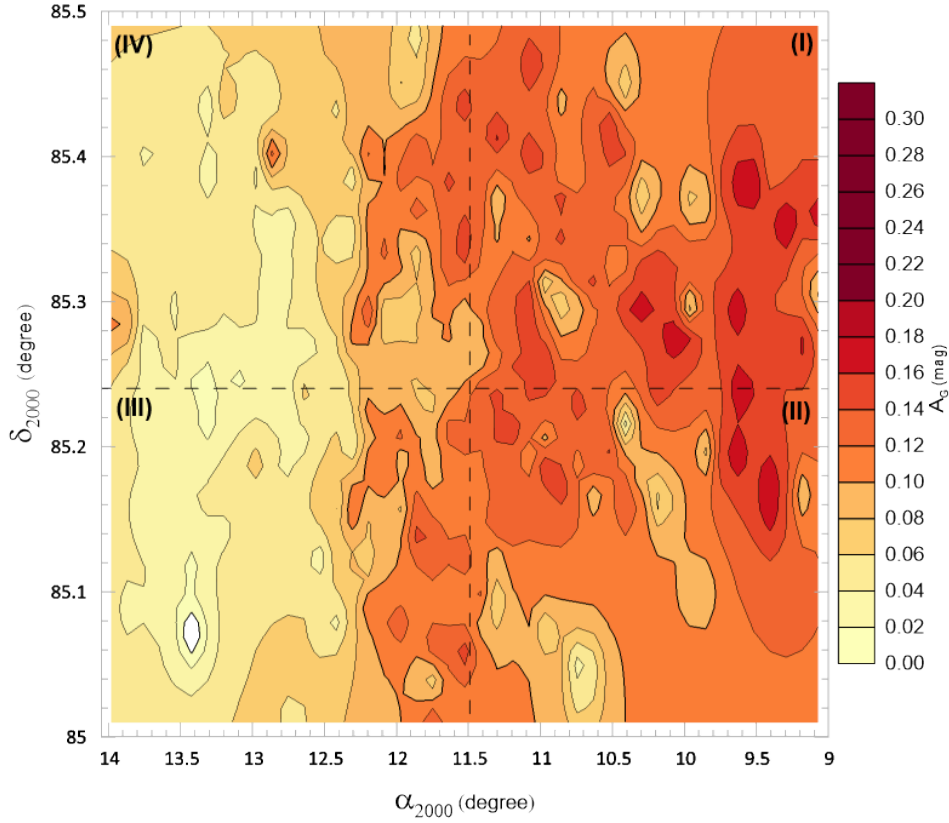


Figure 13. The contour plot of the A_V values of 412 members of NGC 188 obtained by SED analysis. The center of the cluster is marked by the midpoint of the dashed line.

radius ($r_{\text{lim}} \leq 15'$), the two BSSs identified by Rain et al. (2021) fall outside these limitations. The BSSs are depicted in Figure 7. Given that the formation mechanisms of BSSs are primarily associated with mass transfer in close binary systems (McCrea 1964) and stellar collisions (Hills & Day 1976), we exclude these stars in the SED analysis.

4.5. Kinematics and Dynamic Orbit Parameters

In order to determine the Galactic populations of OCs, it is imperative to conduct kinematic and dynamical analyses of their orbits (Taşdemir & Yontan 2023; Yontan & Canbay 2023). Detailed kinematic analyses of NGC 188 were carried out, encompassing the determination of its space velocity components, Galactic orbit parameters, and birth radii. These analyses utilized the MWPOTENTIAL2014 model from the Galactic dynamics library GALPY² package by Bovy (2015), implemented in the Python programming language. The galactocentric distance and orbital velocity of the Sun were set to $R_{\text{gc}} = 8$ kpc and $V_{\text{rot}} = 220$ km s⁻¹, respectively (Bovy 2015; Bovy & Tremaine 2012). The distance of the Sun from the Galactic plane was considered as $Z_0 = 25 \pm 5$ pc (Jurić et al. 2008). Radial velocity is a crucial parameter for constructing the orbit of a celestial object around the Galactic center. The mean radial velocity of

NGC 188 was calculated, taking into account the most likely cluster members with available radial velocity measurements in *Gaia* DR3. 68 stars were identified for this calculation. The mean radial velocity was determined using the equation provided by Carrera et al. (2022a), yielding $V_R = -41.6 \pm 0.12$ km s⁻¹. This result aligns well with findings from literature studies (see also Table 1). To perform orbit integration of NGC 188, the following parameters were used as input:

The central equatorial coordinates ($\langle \alpha, \delta \rangle$) = (00^h47^m20^s.96, $\delta = +85^\circ 15' 05''.27$) (Hunt & Reffert 2023), the mean proper-motion components ($\mu_\alpha \cos \delta = -2.314 \pm 0.002$, $\mu_\delta = -1.022 \pm 0.002$ mas yr⁻¹) determined in Section 4.2, the isochrone distance ($d_{\text{iso}} = 1806 \pm 21$ pc) from Section 4.3, and the radial velocity ($V_R = -41.6 \pm 0.12$ km s⁻¹) calculated in the study (see also Table 5). To infer the current likely position of NGC 188, the orbit of the cluster was integrated forward with an integration step from 5 Myr to 7.65 Gyr. Results of orbit integration process: apogalactic ($R_a = 9694 \pm 30$ pc) and perigalactic ($R_p = 8729 \pm 31$ pc) distances, eccentricity ($e = 0.05$), maximum vertical distance from the Galactic plane ($Z_{\text{max}} = 851$ pc), space velocity components ($U, V, W = 35.90 \pm 0.13, -18.82 \pm 0.25, -23.58 \pm 0.03$ km s⁻¹), and orbital period ($P_{\text{orb}} = 259$ Myr). Taking into account the space velocity component values (U, V, W)_⊙ = (8.83 ± 0.24, 14.19 ± 0.34, 6.57 ± 0.21) km s⁻¹

² See also <https://galpy.readthedocs.io/en/v1.5.0/>

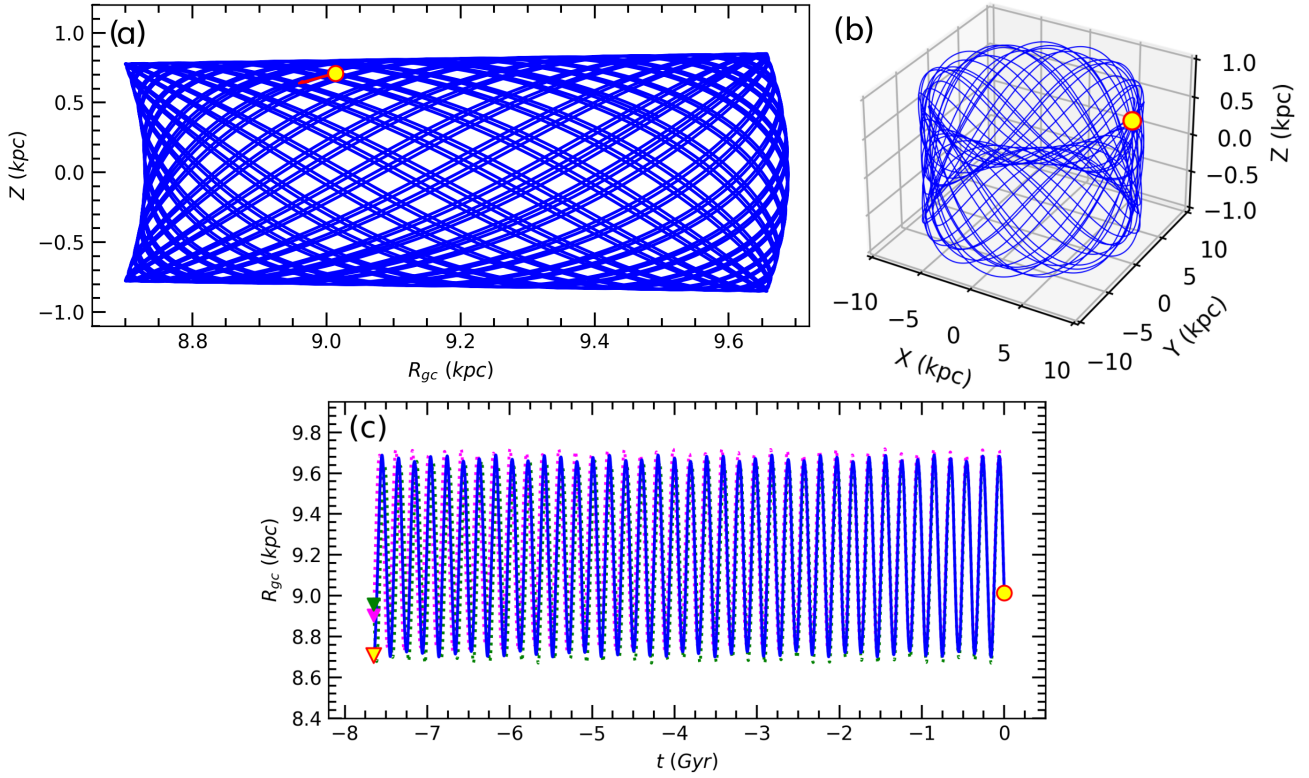


Figure 14. The Galactic orbits and birth radii of NGC 188 are illustrated on three different planes: $Z \times R_{gc}$ (a), $X \times Y \times Z$ (b), and $R_{gc} \times t$ (c). Present-day positions are denoted by filled yellow circles, while birth positions are indicated by filled triangles. The red arrow represents the motion vector of the cluster. Additionally, purple and pink dotted lines represent the orbit under consideration of errors in input parameters, with purple and pink-filled triangles indicating the lower and upper error estimates of the open cluster's birth locations, respectively.

of Coşkunoğlu et al. (2011), we applied a Local Standard of Rest (LSR) correction to the (U, V, W) components of NGC 188. Hence, we derived the LSR corrected space velocity components as $(U, V, W)_{LSR} = (44.73 \pm 0.27, -4.63 \pm 0.42, -17.01 \pm 0.21)$ km s⁻¹. Using these LSR results, we estimated the total space velocity as $S_{LSR} = 48.08 \pm 0.54$ km s⁻¹ (see also Table 5). The cluster reaches a maximum distance above the Galactic plane at $Z_{max} = 851 \pm 10$ pc, indicating that NGC 188 belongs to the old thin-disc component of the Milky Way (Ak et al. 2015).

The 3D motion of the cluster around the Galactic center is depicted in Figure 14b. As observed in the figure, NGC 188 follows an almost circular orbit around the Galactic plane, experiencing separation from the Galactic plane by ± 0.8 kpc during its motion. Figure 14c illustrates the distance of the cluster on the $R_{gc} \times t$ plane as a function of time, providing insights into how uncertainties in the input parameters impact the orbit of the cluster. Dynamical analysis reveals that NGC 188 was formed outside the solar circle, with a birth radius of $R_{Birth} = 8.71 \pm 0.01$ kpc.

5. CONCLUSION

In this study, detailed analyses of the NGC 188 open cluster were performed by using Gaia DR3 astrometric, photometric and spectroscopic data. We identified 868 most likely members for the cluster. Astrophysical parameters were derived via isochron fitting procedure to the CMD. In addition, we investigated the orbit of NGC 188 by utilising kinematic and dynamic analyses. In addition, except for similar cluster studies in the literature, the basic astrophysical parameters of 412 most likely members ($P \geq 0.5$) stars brighter than $G = 17$ mag were determined by SED analyses. The basic astrophysical parameters for NGC 188 were also obtained from the mean values of the SED analysis results and were compared with those obtained using the isochron fitting method. We concluded that the parameters determined from the two methods are in a good agreement. However, we observed a wide range of metallicity and V -band extinction values among the member stars, particularly in NGC 188, where we identified differential extinction for the first time in this study.

All parameters determined in the study are listed in Table 5. The main results of the study are summarised as follows:

Table 5. Fundamental parameters of NGC 188.

Parameter	Classic Method	SED Method
Astrometric Parameters		
$(\alpha, \delta)_{J2000}$ (Sexagesimal)	00:47:20.96, +85:15:05.27	
$(l, b)_{J2000}$ (Decimal)	122.8368, 22.3730	
f_{bg} (stars arcmin ⁻²)	2.832 ± 0.356	
f_0 (stars arcmin ⁻²)	12.229 ± 0.768	
r_c (arcmin)	2.183 ± 0.304	
r_{lim} (arcmin)	15	
r (pc)	7.88	
Cluster members ($P \geq 0.5$)	868	412
$\mu_\alpha \cos \delta$ (mas yr ⁻¹)	-2.314 ± 0.002	
μ_δ (mas yr ⁻¹)	-1.022 ± 0.002	
ϖ (mas)	0.550 ± 0.023	
d_ϖ (pc)	1818 ± 76	
Astrophysical Parameters		
$E(B - V)$ (mag)	0.047 ± 0.009	0.034 ± 0.030
$E(G_{BP} - G_{RP})$ (mag)	0.066 ± 0.012	—
A_V (mag)	0.146 ± 0.068	0.107 ± 0.091
A_G (mag)	0.123 ± 0.022	—
[Fe/H] (dex)	-0.030 ± 0.015*	0.00 ± 0.03
Age (Gyr)	7.65 ± 1.00	7.78 ± 0.23
$V - M_V$ (mag)	—	11.306 ± 0.007
$G - M_G$ (mag)	11.407 ± 0.025	—
d_{iso} (pc)	1806 ± 21	1854 ± 148
$(X, Y, Z)_\odot$ (pc)	(-906, 1403, 687)	(-915, 1418, 695)
R_{gc} (pc)	9015	9027
Kinematic & Dynamic Orbit Parameters		
V_R (km s ⁻¹)	-41.60 ± 0.12	
U_{LSR} (km s ⁻¹)	+44.73 ± 0.27	
V_{LSR} (kms ⁻¹)	-4.63 ± 0.42	
W_{LSR} (kms ⁻¹)	-17.01 ± 0.21	
S_{LSR} (kms ⁻¹)	48.08 ± 0.54	
R_a (pc)	9694 ± 30	
R_p (pc)	8729 ± 31	
z_{max} (pc)	851 ± 10	
e	0.052 ± 0.001	
P_{orb} (Myr)	259 ± 10	
R_{Birth} (kpc)	8.71 ± 0.01	

*Casamiquela et al. (2021)

1. From the RDP analyses, we determined the limiting radius by visual inspection as $r_{lim}^{obs} = 15'$.

2. Taking into account the results of the photometric completeness limit, membership probability analyses, and limiting

radius, we identified 868 most likely members with probabilities of $P \geq 0.5$ for NGC 188. These stars were used in the cluster analyses.

3. The mean proper motion components were obtained as $(\mu_\alpha \cos \delta, \mu_\delta) = (-2.314 \pm 0.002, -1.022 \pm 0.002)$ mas yr⁻¹.

4. 19 most likely BSS members were identified within the limiting radius of the NGC 188.

5. The metallicity value for the cluster was taken as $[\text{Fe}/\text{H}] = -0.030 \pm 0.015$ dex, as presented by Casamiquela et al. (2021). We transformed this value into the mass fraction $z = 0.0142$ and kept it as a constant parameter for age and distance estimation.

6. The isochrone fitting distance of NGC 188 was determined as $d_{\text{iso}} = 1806 \pm 21$ pc. This value is supported by the distance $d_{\varpi} = 1818 \pm 76$ pc, which is derived from mean trigonometric parallax. The SED analysis distance of the member of c stars in NGC 188 was obtained as $d = 1854 \pm 148$ pc.

7. The isochrone fitting method gives the age of the NGC 188 cluster as $t = 7.65 \pm 1.00$ Gyr while the SED analysis provides the mean age of the cluster determined $t = 7.78 \pm 0.23$ Gyr

8. Orbit integration was performed via MWPOTENTIAL2014 model. We concluded that NGC 188 orbits in a boxy pattern outside the solar circle, as well as the cluster is a member of the thin-disc component of the Milky Way. Moreover, the birth radius (8.71 ± 0.01 kpc) indicates that the forming region of the cluster is outside the solar circle.

9. NGC 188 V-band extinction analysis of 412 stars revealed distinct extinction patterns across the cluster's equatorial coordinates. Notably, the upper right and lower right quadrants displayed considerable deviation from the upper left and lower left ones. The examination resulted in varied V-band extinction averages, with a clear trend: stars with lower right ascension exhibited higher A_V values, indicating a notable correlation within the cluster.

10. SED analysis of the member stars revealed that determined effective temperatures and surface gravities align well with stellar evolution models across different luminosity classes.

11. The SED analysis revealed an age range of 1.11 to 13.39 Gyr. When dividing the main-sequence stars into three luminosity groups, it becomes apparent that the bright stars exhibit a narrow age range, whereas the range widens as we move towards the faint stars. This implies that the age values of faint open cluster stars require careful evaluation during SED analyses.

In this study, SED analyses of NGC 188 which is an old open cluster, demonstrate that with the increase in the number of photometric data, the fundamental astrophysical parameters of open clusters can be determined with greater precision.

Peer Review: Externally peer-reviewed.

Author Contribution: Conception/Design of study - DCD, S.T.; Data Acquisition - DCD, S.T., S.K., S.I.; Data Analysis/Interpretation - DCD, S.T., S.K., S.I.; Drafting Manuscript

- DCD, S.T., S.I.; Critical Revision of Manuscript - DCD, S.T.; Final Approval and Accountability - DCD, S.T., S.K., S.I.; Technical or Material Support - DCD, S.T., S.K., S.I.

Conflict of Interest: Authors declared no conflict of interest.

Financial Disclosure: This study has been supported in part by the Scientific and Technological Research Council (TÜBİTAK) 122F109

Acknowledgements: We are grateful to the referees for their valuable feedback, which improved the paper. Special thanks to Dr. Olcay Plevne for technical support. This research has made use of the WEBDA database, operated at the Department of Theoretical Physics and Astrophysics of the Masaryk University. We also made use of NASA's Astrophysics Data System as well as the Vizier and Simbad databases at CDS, Strasbourg, France and data from the European Space Agency (ESA) mission *Gaia*³, processed by the *Gaia* Data Processing and Analysis Consortium (DPAC)⁴. Funding for DPAC has been provided by national institutions, in particular, the institutions participating in the *Gaia* Multilateral Agreement.

LIST OF AUTHOR ORCIDS

D. C. Dursun <https://orcid.org/0000-0001-7940-3731>
 S. Taşdemir <https://orcid.org/0000-0003-1339-9148>
 S. Koç <https://orcid.org/0000-0001-7420-0994>
 S. Iyer <https://orcid.org/0009-0001-5220-0034>

REFERENCES




- Adams F. C., Lada C. J., Shu F. H., 1987, *ApJ*, **312**, 788
 Aizenman M. L., Demarque P., Miller R. H., 1969, *ApJ*, **155**, 973
 Ak T., Bilir S., Özdönmez A., Soyduğan F., Soyduğan E., Püsküllü Ç., Ak S., Eker Z., 2015, *Ap&SS*, **357**, 72
 Allard F., Homeier D., Freytag B., 2012, *Philosophical Transactions of the Royal Society of London Series A*, **370**, 2765
 Belloni T., Verbunt F., Mathieu R. D., 1998, *A&A*, **339**, 431
 Bossini D., et al., 2019, *A&A*, **623**, A108
 Bovy J., 2015, *ApJS*, **216**, 29
 Bovy J., Tremaine S., 2012, *ApJ*, **756**, 89
 Bressan A., Marigo P., Girardi L., Salasnich B., Dal Cero C., Rubele S., Nanni A., 2012, *MNRAS*, **427**, 127
 Bukowiecki Ł., Maciejewski G., Konorski P., Strobel A., 2011, *Acta Astron.*, **61**, 231
 Cantat-Gaudin T., Anders F., 2020, *A&A*, **633**, A99
 Cantat-Gaudin T., et al., 2018, *A&A*, **618**, A93
 Caputo F., Chieffi A., Castellani V., Collados M., Martinez Roger C., Paez E., 1990, *AJ*, **99**, 261
 Cardelli J. A., Clayton G. C., Mathis J. S., 1989, *ApJ*, **345**, 245

³ <https://www.cosmos.esa.int/gaia>

⁴ <https://www.cosmos.esa.int/web/gaia/dpac/consortium>

- Carraro G., Chiosi C., 1994, *A&A*, **287**, 761
- Carraro G., Costa E., 2007, *A&A*, **464**, 573
- Carraro G., Lia C., Chiosi C., 1998, *MNRAS*, **297**, 1021
- Carraro G., Sales Silva J. V., Moni Bidin C., Vazquez R. A., 2017, *AJ*, **153**, 99
- Carrera R., et al., 2022a, *A&A*, **658**, A14
- Carrera R., et al., 2022b, *A&A*, **663**, A148
- Casamiquela L., et al., 2021, *A&A*, **652**, A25
- Castelli F., Kurucz R. L., 2003, in *Modelling of Stellar Atmospheres*. p. A20, doi:10.48550/arXiv.astro-ph/0405087
- Chen L., Hou J. L., Wang J. J., 2003, *AJ*, **125**, 1397
- Coşkunoğlu B., et al., 2011, *MNRAS*, **412**, 1237
- De Meulenaer P., Narbutis D., Mineikis T., Vanevičius V., 2013, *A&A*, **550**, A20
- Demarque P. R., Larson R. B., 1964, *ApJ*, **140**, 544
- Demarque P., Green E. M., Guenther D. B., 1992, *AJ*, **103**, 151
- Dias W. S., Monteiro H., Caetano T. C., Lépine J. R. D., Assafin M., Oliveira A. F., 2014, *A&A*, **564**, A79
- Dias W. S., Monteiro H., Moitinho A., Lépine J. R. D., Carraro G., Paunzen E., Alessi B., Vilella L., 2021, *MNRAS*, **504**, 356
- Donor J., et al., 2018, *AJ*, **156**, 142
- Dotter A., 2016, *ApJS*, **222**, 8
- Elsanhoury W. H., Haroon A. A., Chupina N. V., Vereshchagin S. V., Sariya D. P., Yadav R. K. S., Jiang I.-G., 2016, *New Astron.*, **49**, 32
- Fitton S., Tofflemire B. M., Kraus A. L., 2022, *RNAAS*, **6**, 18
- Fornal B., Tucker D. L., Smith J. A., Allam S. S., Rider C. J., Sung H., 2007, *AJ*, **133**, 1409
- Friel E. D., 1995, *ARA&A*, **33**, 381
- Gaia Collaboration et al., 2016, *A&A*, **595**, A1
- Gaia Collaboration et al., 2018, *A&A*, **616**, A1
- Gaia Collaboration et al., 2021, *A&A*, **649**, A1
- Gaia Collaboration et al., 2023, *A&A*, **674**, A1
- Gao X., Fang D., 2022, *Ap&SS*, **367**, 87
- Glebbeeck E., Pols O. R., 2008, *A&A*, **488**, 1017
- Greenstein J. L., Keenan P. C., 1964, *ApJ*, **140**, 673
- Harris W. E., Pudritz R. E., 1994, *ApJ*, **429**, 177
- Hills J. G., Day C. A., 1976, *Astrophys. Lett.*, **17**, 87
- Hills S., von Hippel T., Courteau S., Geller A. M., 2015, *AJ*, **149**, 94
- Huang Y., Yuan H., Beers T. C., Zhang H., 2021, *ApJ*, **910**, L5
- Hunt E. L., Reffert S., 2023, *A&A*, **673**, A114
- Husser T. O., Wende-von Berg S., Dreizler S., Homeier D., Reiners A., Barman T., Hauschildt P. H., 2013, *A&A*, **553**, A6
- Jacobson H. R., Pilachowski C. A., Friel E. D., 2011, *AJ*, **142**, 59
- Janes K., Demarque P., 1983, *ApJ*, **264**, 206
- Janes K., Barnes S. A., Meibom S., Hoq S., 2014, *AJ*, **147**, 139
- Joshi Y. C., 2005, *MNRAS*, **362**, 1259
- Joshi Y. C., Dambis A. K., Pandey A. K., Joshi S., 2016, *A&A*, **593**, A116
- Jurić M., et al., 2008, *ApJ*, **673**, 864
- King I., 1962, *AJ*, **67**, 471
- King I. R., Bedin L. R., Piotto G., Cassisi S., Anderson J., 2005, *AJ*, **130**, 626
- Lada C. J., Lada E. A., 2003, *ARA&A*, **41**, 57
- Leonard P. J. T., 1989, *AJ*, **98**, 217
- Leonard P. J. T., Linnell A. P., 1992, *AJ*, **103**, 1928
- Lindegren L., et al., 2021, *A&A*, **649**, A4
- Lorenzo-Oliveira D., Porto de Mello G. F., Schiavon R. P., 2016, *A&A*, **594**, L3
- McClure R. D., Twarog B. A., 1977, *ApJ*, **214**, 111
- McCrea W. H., 1964, *MNRAS*, **128**, 147
- Netopil M., Oralhan İ. A., Çakmak H., Michel R., Karataş Y., 2022, *MNRAS*, **509**, 421
- Oke J. B., 1974, *ApJS*, **27**, 21
- Patenaude M., 1978, *A&A*, **66**, 225
- Piskunov A. E., Kharchenko N. V., Röser S., Schilbach E., Scholz R. D., 2006, *A&A*, **445**, 545
- Rain M. J., Ahumada J. A., Carraro G., 2021, *A&A*, **650**, A67
- Riess A. G., Casertano S., Yuan W., Bowers J. B., Macri L., Zinn J. C., Scolnic D., 2021, *ApJ*, **908**, L6
- Robitaille T. P., Whitney B. A., Indebetouw R., Wood K., Denzmore P., 2006, *ApJS*, **167**, 256
- Sandage A., 1962, *ApJ*, **135**, 333
- Sarajedini A., von Hippel T., Kozhurina-Platais V., Demarque P., 1999, *AJ*, **118**, 2894
- Song F.-F., Niu H.-B., Esamdin A., Zhang Y., Zeng X.-Y., 2023, *Research in Astronomy and Astrophysics*, **23**, 095015
- Soubiran C., et al., 2018, *A&A*, **619**, A155
- Spina L., et al., 2021, *MNRAS*, **503**, 3279
- Spinrad H., Greenstein J. L., Taylor B. J., King I. R., 1970, *ApJ*, **162**, 891
- Sun M., Jiang B., Yuan H., Li J., 2021, *ApJS*, **254**, 38
- Taşdemir S., Yontan T., 2023, *Physics and Astronomy Reports*, **1**, 1
- Tarricq Y., et al., 2021, *A&A*, **647**, A19
- Twarog B. A., Anthony-Twarog B. J., 1989, *AJ*, **97**, 759
- Uppgren A. R., Mesrobian W. S., Kerridge S. J., 1972, *AJ*, **77**, 74
- VandenBerg D. A., 1983, *ApJS*, **51**, 29
- VandenBerg D. A., Stetson P. B., 2004, *PASP*, **116**, 997
- Vines J. I., Jenkins J. S., 2022, *MNRAS*, **513**, 2719
- Wang J., Ma J., Wu Z., Wang S., Zhou X., 2015, *AJ*, **150**, 61
- Webbink R. F., 1976, *ApJ*, **209**, 829
- Worthey G., Jowett K. J., 2003, *PASP*, **115**, 96
- Yadav R. K. S., Dattatreya A. K., Rangwal G., Subramaniam A., Bisht D., Sagar R., 2024, *ApJ*, **961**, 251
- Yontan T., 2023, *AJ*, **165**, 79
- Yontan T., Canbay R., 2023, *Physics and Astronomy Reports*, **1**, 65
- Yontan T., et al., 2015, *Ap&SS*, **355**, 267
- Yontan T., et al., 2019, *Ap&SS*, **364**, 152
- Zheng Z., et al., 1999, *AJ*, **117**, 2757
- Zinn J. C., 2021, *AJ*, **161**, 214
- Zinn R., Dahn C. C., 1976, *AJ*, **81**, 527

The Fundamental Parameters and Evolutionary Status of V454 Aurigae

G. Yücel^{1*},  R. Canbay² , and V. Bakış³ 

¹Istanbul University, Faculty of Science, Department of Astronomy and Space Sciences, Beyazıt, 34119, İstanbul, Türkiye

²Istanbul University, Institute of Graduate Studies in Science, Programme of Astronomy and Space Sciences, 34116, Beyazıt, İstanbul, Türkiye

³Akdeniz University, Faculty of Science, Department of Space Sciences and Technologies, Konyaaltı, 07030, Antalya, Türkiye

ABSTRACT

Eclipsing binary systems have a unique feature that enables scientists to obtain precise fundamental star parameters, which opens up a greater area of astrophysics studies. In this study, we derived the fundamental parameters, evolutionary status, and birthplace of V454 Aur in the Galaxy by combining radial velocity, photometric, and spectral energy distribution data. We have updated the ephemerides and period of V454 Aur as $2458850.80136^{+0.00001}_{-0.00001}$ and $27.0198177^{+0.0000003}_{-0.0000003}$, respectively. We obtain $1.173^{+0.016}_{-0.016} M_{\odot}$ and $1.203^{+0.022}_{-0.026} R_{\odot}$ for the primary component and $1.045^{+0.015}_{-0.014} M_{\odot}$ and $0.993^{+0.034}_{-0.027} R_{\odot}$ for the secondary component. The effective temperatures for the components were accurately determined via SED data as 6250^{+150}_{-150} K and 5966^{+109}_{-89} K for the primary component and secondary component, respectively. The metallicity of the components is derived from evolutionary tracks, which implies a slightly higher metallicity than Solar metallicity. According to the analysis, the components of V454 Aur are in the main sequence. Our distance calculation for the system is 65.07^{+2}_{-3} pc and is in excellent agreement with *Gaia* astrometric data, which is $65.07^{+0.09}_{-0.09}$ pc. The current age of the system is $1.19^{+0.08}_{-0.09}$ Gyr, and it will start mass transfer between components in 5 Gyr from now on. Dynamical orbital analysis shows that V454 Aur follows a boxy pattern around the Galactic centre and is a member of the thin-disc component of the Galaxy. Considering the age and metallicity of this system, it was found to have formed just outside the Solar circle.

Keywords: Stars: binaries ; stars: fundamental parameters ; stars: evolution ; stars: kinematics

1. INTRODUCTION

In principle, to understand our Galaxy, and therefore the universe, and its evolution, we need to understand its cornerstone, which is stars. The evolution of a star is mostly based on its mass, and then its chemical composition. There are several ways to acquire the mass of a star, but among them, eclipsing binaries are the most accurate ones (Serenelli et al. 2021). Eclipsing binaries, in general, are the centre of astrophysics studies because they provide valuable information (mass, radius, temperature, etc.) of the component stars within 1–3% uncertainty rates, or mostly even better according to the quality of the data used in analysis (Torres et al. 2010; Prša 2020). The number of eclipsing binaries with known fundamental parameters is increasing every day, but this is not a reason to stop investigating new eclipsing binary systems and obtaining their parameters, since every known system is a source for several studies from stellar populations (e.g. Chabrier 2003; Moe & Di Stefano 2017) to empirical MLR studies (e.g. Benedict et al. 2016; Eker et al. 2015, 2018, 2024). Therefore, there is still a need to study eclipsing binaries and derive their fundamental parameters precisely.

V454 Aur (HD 44192, SAO 59016, Hip 30270, $l = 178^{\circ}.803546$, $b = 09^{\circ}.510553$) is a Northern Hemisphere detached eclipsing binary system. The variable star feature of V454 Aur was discovered by *Hipparcos* (Perryman et al. 1997). The first ground-based observation of V454 Aur was done by Griffin (2001) via obtaining photoelectric radial velocities (RVs). As a result, the spectroscopic orbit of V454 Aur was calculated. Later, Nordström et al. (2004) calculated the temperature, metallicity, and age of the star as 6025 K, -0.14 dex, and 5 Gyr, respectively, by using *ubvy* photometric data. These values were improved by Holmberg et al. (2009) and later on by Casagrande et al. (2011) for temperature, $\log g$, metallicity, and age as 6064 K, -0.08 dex, 4.43 dex, and 4 Gyr, respectively. Prša et al. (2022) have used *TESS* (Ricker et al. 2015) observations to calculate ephemerides and the period of V454 Aur and obtained the values of $2458850.778358 \pm 0.002306$ and 17.8883306 ± 0.0064858 days, respectively. However, they performed the analysis based on only one sector, the 20th. There has been no prior study of this system.

In this study, we combined radial velocity and photometric data with multiple sectors, which is provided by *TESS*, and obtained the fundamental parameters of V454 Aur for the first

Corresponding Author: G. Yücel E-mail: gokhannyucel@gmail.com

Submitted: 07.03.2024 • Revision Requested: 12.04.2024 • Last Revision Received: 26.04.2024 • Accepted: 28.04.2024 • Published Online: 05.06.2024



This article is licensed under a Creative Commons Attribution-NonCommercial 4.0 International License (CC BY-NC 4.0)

time in the literature. We studied its evolution scenarios and found the system's initial orbital parameters and kinematics, which tell us where this system was born.

This paper is structured as follows. In Section 2, we present the properties of the observational data used. In Section 3, the calculated fundamental parameters of the system are presented. In Section 4, we present a detailed evolutionary analysis. In Section 5, we present the kinematics of the system. Finally, in Section 6, we have discussed our comprehensive results.

2. DATA

2.1. Radial Velocities

Radial velocity data (RVs) used in this study, were taken from Griffin (2001). Details can be found in that paper, but we briefly give a summary here. Griffin (2001) observed V454 Aur in the years of 2000-2001, with a total of 65 observations for both components at Observatoire de Haute-Provence¹ with 1-m Swiss telescope, equipped with Coravel (Baranne et al. 1979) instrument. The RVs used in this study are given in Table 1.

2.2. Photometric Data

Photometric data, which are used in this study, have been obtained via *TESS*. Although the main purpose of *TESS* is that of finding exoplanets by looking at brightness changes of a star, it has also been a source of producing light curves of eclipsing binaries, which are also needed to analyse eclipsing binary systems (Prša et al. 2022).

TESS has observed V454 Aur in a total of five sectors, which are 20, 43, 44, 45, and 60 with exposure times 1800s, 600s, 600s, 600s, and 200s, respectively. *TESS* has also observed V454 Aur in sectors 71, 72, and 73, but those photometric data are not available.

We have used Lightkurve v2.4 (Lightkurve Collaboration et al. 2018) to acquire photometric data. Photometric data with 200s exposure time were used in the analysis wherever available, but missing parts were completed by other sectors. The photometric data used in this study are shown in Figure 1 by each sector.

3. FUNDAMENTAL PARAMETERS

3.1. Analysis of Ephemerides

In the literature, there is only one time of minimum measurement, which was obtained with *Hipparcos* (Perryman et al. 1997), for the system, which makes its long-term orbital period change study impossible. Nevertheless, *TESS* satellite obtained five consecutive measurements (sectors; see Figure 1),

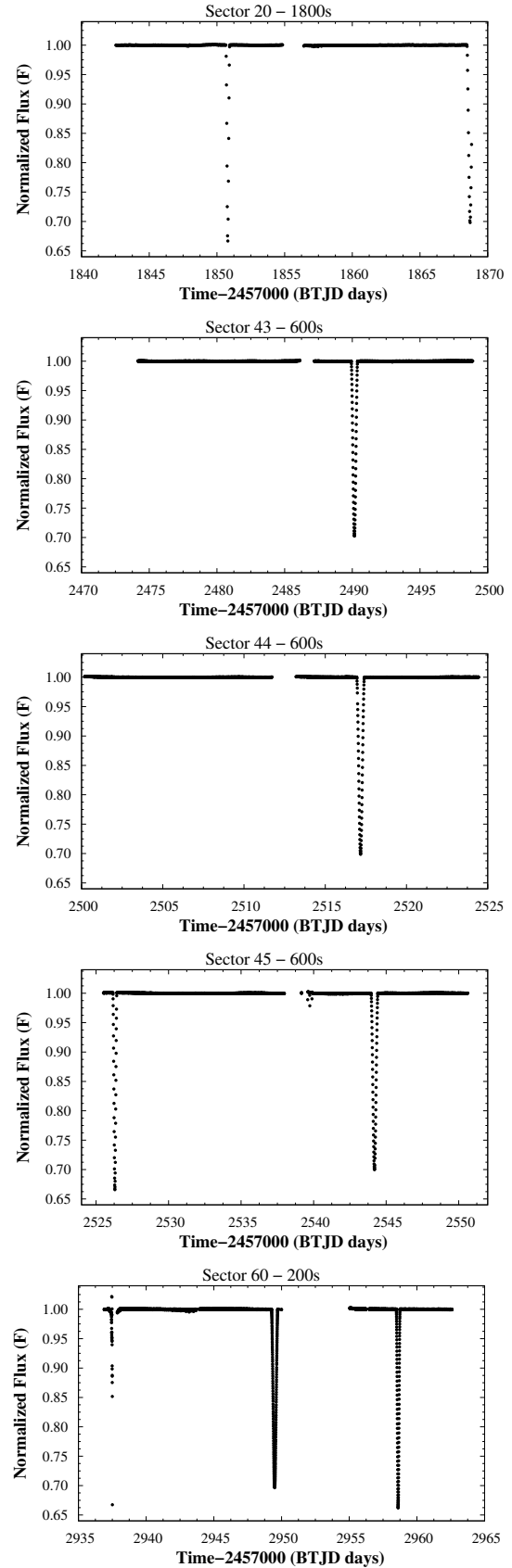


Figure 1. *TESS* observation of V454 Aur in five different sectors.

¹ <http://www.obs-hp.fr>

Table 1. The radial velocities that were used in this study.

HJD-2400000	RV ₁ (km s ⁻¹)	RV ₂ (km s ⁻¹)	HJD-2400000	RV ₁ (km s ⁻¹)	RV ₂ (km s ⁻¹)	HJD-2400000	RV ₁ (km s ⁻¹)	RV ₂ (km s ⁻¹)
51595.994	-29.3	-52.5	51852.055	-54.1	-24.5	51906.102	-54.1	-24.6
51602.935	-76.8	0.0	51852.097	-53.6	-27.0	51906.115	-54.6	-25.0
51604.912	-93.2	20.0	51852.149	-52.6	-26.3	51906.128	-54.3	-24.9
51606.817	-95.2	22.9	51852.199	-51.5	-29.5	51906.141	-54.8	-24.0
51607.009	-92.9	–	51852.253	-50.8	-31.2	51908.029	-21.2	-64.3
51607.936	-76.0	0.6	51861.198	-11.1	-73.4	51908.894	-13.2	-72.4
51609.912	-33.1	-48.2	51863.154	-16.7	-66.5	51916.051	-13.0	-71.2
51624.908	-38.9	-42.0	51865.156	-25.4	-58.7	51917.973	-19.3	-64.2
51627.947	-60.2	-18.1	51870.143	–	-27.3	51918.947	-24.4	-59.6
51628.889	-67.8	-9.8	51870.225	–	-25.5	51920.099	-29.4	-54.0
51639.886	-7.0	-77.0	51870.268	-54.0	-25.7	51922.976	-44.6	-36.0
51640.896	-5.2	-79.8	51878.126	-77.0	0.6	51924.956	-58.6	-19.9
51641.857	-5.4	-79.4	51880.176	-31.7	-47.5	51925.961	-67.1	-10.8
51657.870	-85.8	10.3	51881.096	-19.1	-62.7	51926.926	-74.4	-4.0
51660.892	-95.1	21.0	51887.089	-7.6	-76.2	51934.972	-21.8	-62.7
51812.171	-29.4	-51.4	51892.066	-23.7	-58.7	51936.957	-7.8	-77.3
51823.191	-93.3	18.8	51900.062	-76.2	-0.8	51946.977	-27.9	-53.8
51826.158	-32.3	-50.8	51906.057	-55.6	-23.8	51954.959	-84.2	8.5
51834.181	-10.9	-72.6	51906.068	-55.4	-24.0	51956.851	-97.7	24.7
51851.043	-78.2	1.7	51906.080	-55.0	-23.8	51981.946	-83.7	8.5
51851.972	-57.0	-22.0	51906.091	-55.3	-24.6			

and using *TESS* measurements allows us to determine the up-to-date ephemeris of the system. We measured the times of minima available in the *TESS* photometric data using the Kwee-Van Woerden method (Kwee & van Woerden 1956), which are presented in Table 2. Because the system has an eccentric orbit, primary and secondary ephemerides are calculated separately. The linear least-squares method to the $O - C$ data ($O - C = T - (T_0 + P \times E)$) yielded the following ephemerides:

$$T(\text{HJD}) = 2458850.80136(1) + 27.0198177(3) \times E \quad (1)$$

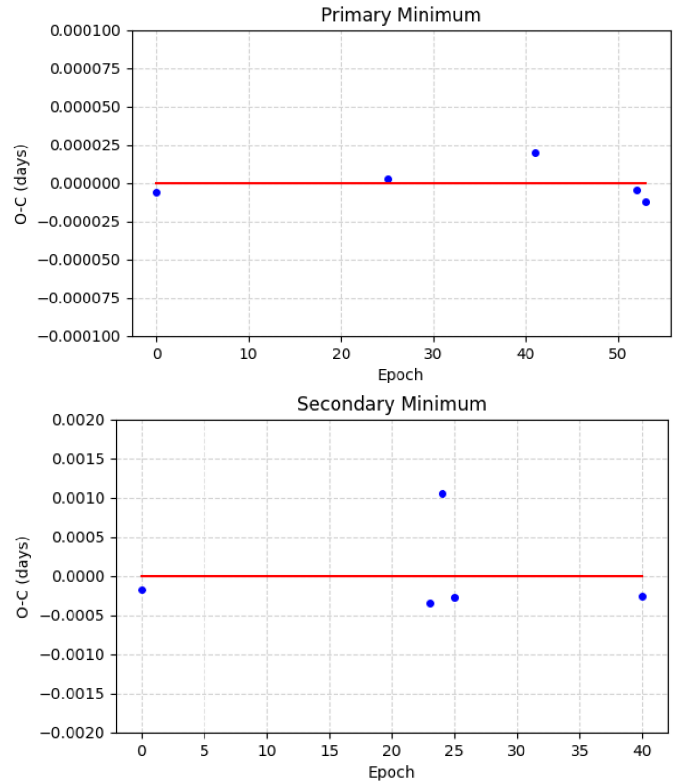
for the primary minimum,

$$T(\text{HJD}) = 2458868.69867(61) + 27.0198105(233) \times E \quad (2)$$

for the secondary minimum. The $O - C$ diagram is shown in Figure 2.

Table 2. The times of minima of V454 Aur extracted from *TESS* data.

Times of minima (HJD)	Component
2458850.80135	pri
2458868.69850	sec
2459490.15397	sec
2459517.17517	sec
2459526.29680	pri
2459544.19366	sec
2459949.49083	sec
2459958.61390	pri
2460255.83187	pri
2460282.85168	pri


Figure 2. $O - C$ diagram for primary and secondary minima.

3.2. Spectroscopic Orbit and Light Curve Modelling

Although the spectroscopic orbit of V454 Aur has been calculated by Griffin (2001), the system has been reanalysed with simultaneous solutions using both RV data and photometric data to obtain fundamental parameters such as mass, radius, temperature ratio, and the light contributions of both components

using Physics Of Eclipsing BinariEs v1.0² (PHOEBE, Prša & Zwitter 2005) which is based on Wilson-Devinney code (WD, Wilson & Devinney 1971; Wilson 1979, 1990; van Hamme 1993; van Hamme & Wilson 2003).

Since there is no indication in the photometric data of any mass transfer in the system, the analysis was performed in detached mode. During the analysis, conjunction time T_0 , orbital period P , and the temperature of the primary component were fixed (see the next section for how the primary component's temperature has been determined) and the following parameters were adjusted: mass ratio (q), eccentricity (e), the argument of periastris (w), semi-major axis (a), systemic velocity (V_γ), orbital inclination (i), temperature of secondary component (T_2), dimensionless surface potentials of both components ($\Omega_{1,2}$), and monochromatic luminosity (L_1). For the limb-darkening (LD) calculations, we adopted logarithmic LD laws. LD values were calculated from Fortran code written by Walter van Hamme³.

After the initial analysis, we used a custom Markov chain Monte Carlo (MCMC) sampler⁴ based on emcee (Foreman-Mackey et al. 2013) to improve the parameters of the components of V454 Aur and to determine the heuristic errors. The sampler ran with 128 walkers and 1000 iterations as conventional. The LC and spectroscopic orbit models are presented in Figure 3 and the fundamental parameters and heuristic errors for V454 Aur are presented in Table 3.

3.3. Component Temperatures

The *Gaia* DR3 trigonometric parallax of V454 Aur is $\varpi = 15.3669 \pm 0.0217$ mas, corresponding to a distance of 65.07 ± 0.09 pc. At this distance, it is expected to be a negligible interstellar extinction. Therefore, the observed $B-V$ colour indicates an extinction-free colour and helps in preliminary temperature estimation. The observed $B - V$ of V454 Aur is given to be 0.57 mag corresponding to a temperature of 5879 K using the colour- T_{eff} calibration table in Bakış & Eker (2022). It should be noted that this colour is the combined colour of two components, making the primary component seem cooler. To obtain a more reliable temperature estimation of the components, we obtained the SED data of V454 Aur and modelled it with the Planck curve as described in Bakış & Eker (2022). While modelling the SED data, the temperature ratio obtained from the LC analysis, the absolute radii of the components, and the distance to V454 Aur are fixed. In Figure 4, we show the SED data of V454 Aur and the best-fitting Planck curve. The temperatures of the components are determined to be 6250 K and 5966 K for the primary and secondary components, respectively. The corner plot of the posterior distribution of the fundamental parameters of V454 Aur is presented in Figure 5.

² <http://phoebe-project.org/1.0/download>

³ <https://faculty.fiu.edu/~vanhamme/ldfiles/ldinterpol.for>

⁴ <https://sourceforge.net/p/phoebe/mailman/message/33650955/>

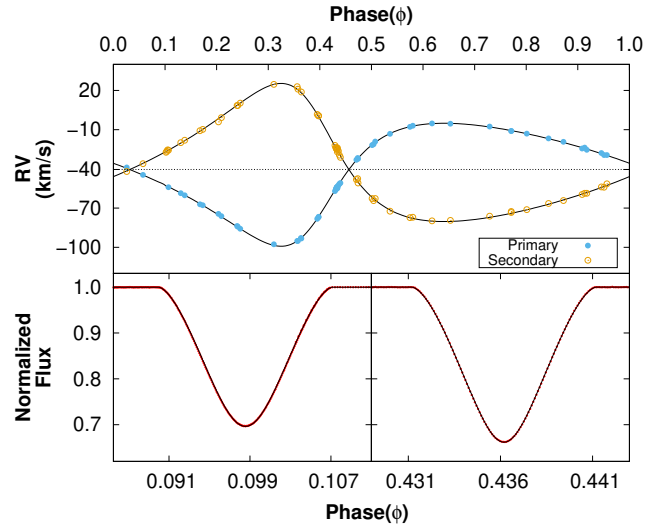


Figure 3. Observed RVs with best fitting radial velocity curves and photometric data with LC modelling. Blue and yellow circles represent the RVs of the primary and secondary components of V454 Aur, respectively. In LC modelling, red dots represent the photometric data and the black curve is the best LC model.

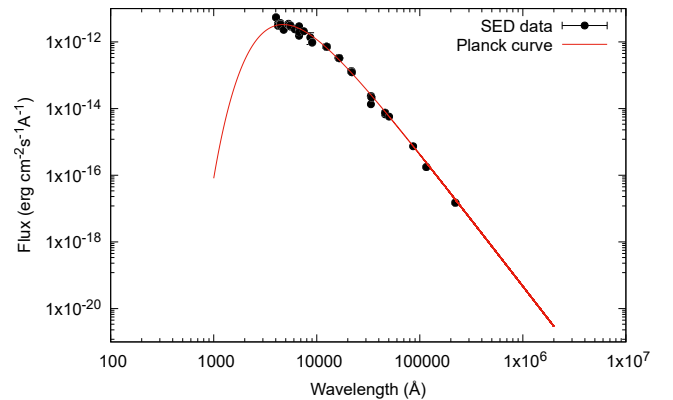


Figure 4. SED data and the Planck curve with binary parameters. The figure axes are in log scale. The SED data corresponds to within 1 arcsec around V454 Aur.

4. EVOLUTIONARY ANALYSIS

One of the scopes of this study is to determine the evolution scenario for V454 Aur using the fundamental parameters we obtained. In this regard, we have used the version of r23.05.1 of Modules for Experiments in Stellar Astrophysics (MESA Paxton et al. 2011, 2013, 2015, 2018, 2019; Jermyn et al. 2023) and MESA SDK v23.7.3 (Townsend 2024) to calculate the evolution of V454 Aur. MESA uses a bunch of microphysics data created by several researchers. The MESA EOS is a blend of the OPAL (Rogers & Nayfonov 2002), SCVH (Saumon et al. 1995), FreeEOS (Irwin 2004), HELM (Timmes & Swesty 2000), PC (Potekhin & Chabrier 2010), and Skye (Jermyn et al. 2021) EOSes. Radiative opacities are primarily from OPAL (Iglesias & Rogers 1993, 1996), with low-temperature data from Ferguson et al. (2005) and the high-temperature, Compton-scattering dominated regime by Poutanen (2017). Electron conduction opacities are from Cassisi et al. (2007) and Blouin et al. (2020).

Table 3. Binary stellar parameters and heuristic errors of V454 Aur.

Parameter	Symbol	Primary	Secondary
Spectral type	Sp	F1 V-IV	F1 V-IV
Ephemerides time (d)	T_0	2458850.80136 ^{+0.00001} _{-0.00001}	
Orbital period (d)	P	27.0198177 ^{+0.0000003} _{-0.0000003}	
Mass (M_\odot)	M	1.173 ^{+0.016} _{-0.016}	1.045 ^{+0.015} _{-0.014}
Radius (R_\odot)	R	1.203 ^{+0.022} _{-0.026}	0.993 ^{+0.034} _{-0.027}
Surface gravity (cgs)	$\log g$	4.345 ^{+0.025} _{-0.022}	4.465 ^{+0.031} _{-0.035}
Separation (R_\odot)	a	49.418 ^{+0.173} _{-0.167}	
Orbital inclination (°)	i	89.263 ^{+0.025} _{-0.027}	
Mass ratio	q	0.890 ^{+0.006} _{-0.005}	
Eccentricity	e	0.37717 ^{+0.00016} _{-0.00013}	
Argument of perigee (rad)	w	3.99763 ^{+0.00035} _{-0.00035}	
Light Ratio (<i>TESS</i>)	l/l_{total}	0.631 ^{+0.013} _{-0.018}	0.369 ^{+0.018} _{-0.013}
Temperature (K)	T_{eff}	6250 ^{+0.150} _{-0.150}	5966 ^{+0.109} _{-0.089}
Luminosity (L_\odot)	$\log L$	0.297 ^{+0.057} _{-0.061}	0.050 ^{+0.055} _{-0.056}
Metallicity	z	0.017 ^{+0.002} _{-0.002}	
Combined visual magnitude ¹	<i>TESS</i>	7.131 ^{+0.006} _{-0.006}	
Individual visual magnitude	<i>TESS</i> _{1,2}	7.631 ^{+0.022} _{-0.022}	8.213 ^{+0.038} _{-0.038}
Combined visual magnitude	V	7.65 ^{+0.01} _{-0.01}	
Individual visual magnitude	$V_{1,2}$	8.129 ^{+0.025} _{-0.025}	8.768 ^{+0.040} _{-0.040}
Combined colour index (mag)	$B - V$	0.57 ^{+0.03} _{-0.03}	
Colour excess (mag)	$E(B - V)$	0	
Bolometric magnitude	M_{bol}	4.010 ^{+0.163} _{-0.167}	4.625 ^{+0.220} _{-0.223}
Absolute visual magnitude	M_V	4.025 ^{+0.153} _{-0.157}	4.676 ^{+0.211} _{-0.215}
Bolometric correction (mag) ²	BC_{TESS}	0.440 ^{+0.006} _{-0.005}	0.490 ^{+0.009} _{-0.007}
Bolometric correction (mag) ³	BC_V	0.093 ^{+0.009} _{-0.008}	0.083 ^{+0.011} _{-0.006}
Systemic velocity (km s ⁻¹)	v_γ	-40.480 ^{+0.099} _{-0.104}	
Computed synchronisation velocity (km s ⁻¹)	v_{synch}	2.1 ^{+0.1} _{-0.1}	1.9 ^{+0.1} _{-0.1}
Age (Gyr)	t	1.19 ^{+0.08} _{-0.09}	
Distance (pc)	d	65 ⁺² ₋₃	
<i>Gaia</i> distance (pc)	d	65.07 ± 0.09	

¹Paegert et al. (2022),²Eker & Bakış (2023),³Bakış & Eker (2022)

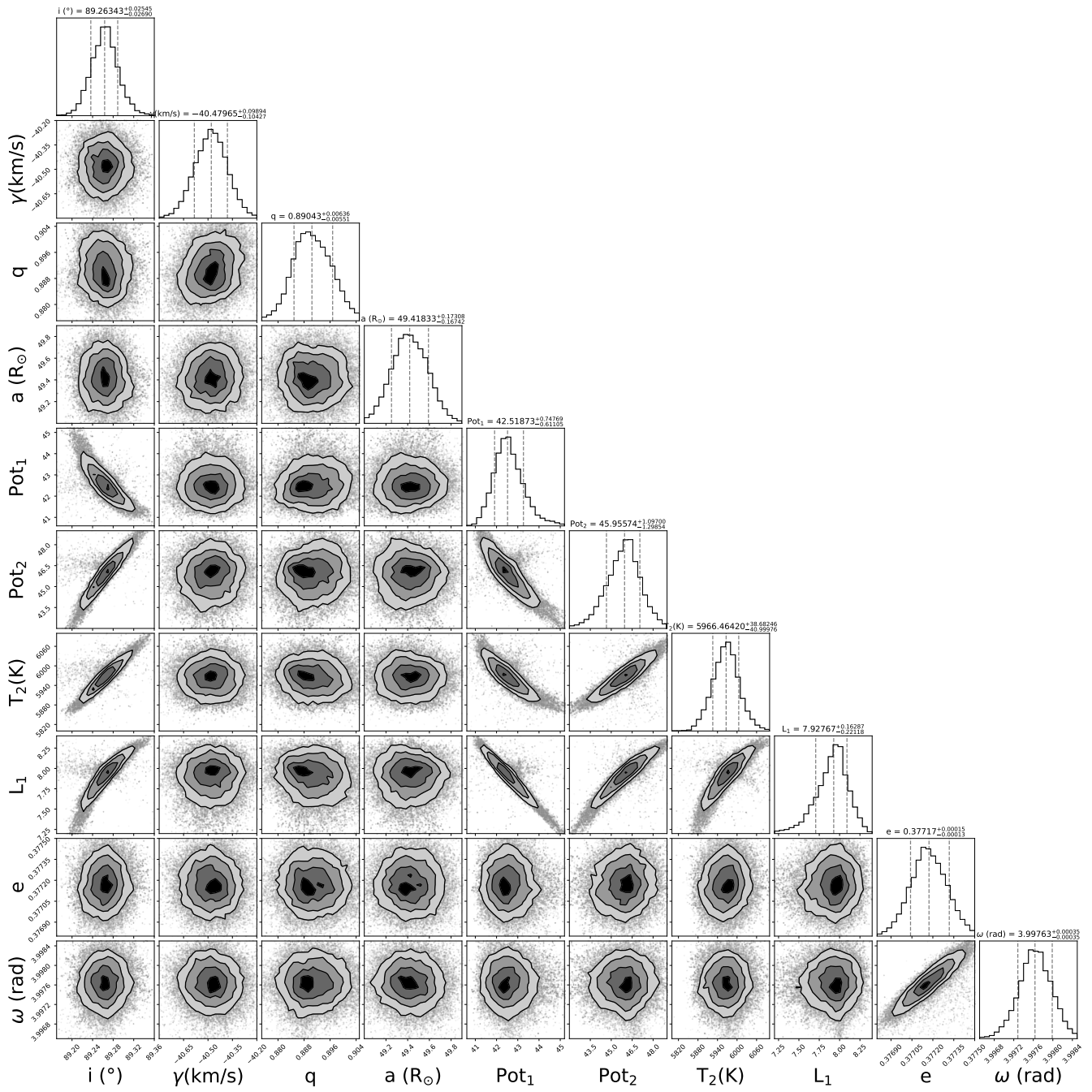


Figure 5. A corner plot of the posteriors for the fundamental parameters of V454 Aur.

Nuclear reaction rates are from JINA REACLIB (Cyburt et al. 2010), NACRE (Angulo et al. 1999) and additional tabulated weak reaction rates Fuller et al. (1985); Oda et al. (1994); Langanke & Martínez-Pinedo (2000). Screening is included via the prescription of Chugunov et al. (2007). Thermal neutrino loss rates are from Itoh et al. (1996), Roche lobe radii in binary systems are computed using the fit of Eggleton (1983). Mass transfer rates in Roche lobe overflowing binary systems are determined following the prescription of Ritter (1988), and so on.

The evolutionary scenario of V454 Aur was studied in two sections: single-star evolution and binary-star evolution.

4.1. Single-star evolution

To establish a well-calculated evolution scenario for a star or a system, the metallicity of the star/system must be known and calculations should be performed according to it. Because there is no spectroscopic data for V454 Aur, we have chosen evolution tracks to determine the metallicity of the systems. Eclipsing binary systems were born in the same stellar nurseries/associations, hence, the metallicity of the components of a binary system must be the same/identical. Considering that the system is detached and there is no mass transfer between components, the components can be treated as individual stars. By using MESA, by including the calculated mass of the components of V454 Aur, we built a grid of evolutionary tracks with different metallicities and, ZAMS lines, which are dashed lines. Our results are given in Figure 6 as $T_{\text{eff}} - \log L$, $T_{\text{eff}} - R$, and $T_{\text{eff}} - \log g$ planes. Hence, the metallicity (z) of the system was determined as $z = 0.017 \pm 0.002$. Both components of V454 Aur are in the main sequence and still burning hydrogen in their cores.

4.2. Binary-star evolution

The components of V454 Aur are on the main-sequence and the system is detached. Hence, the calculation of the evolution of the system with single-star evolution is agreeable. Nonetheless, to understand the evolution of the system from its formation to its end, it is necessary to evolve the system in binary form. MESA enables this option with its `binary` module. As a starting point, the initial orbital conditions must be calculated. In this regard, we have used a similar approach that has already been used in literature (Rosales et al. 2019; Soydogan et al. 2020; Yücel & Bakış 2022). We built a grid with starting different initial orbital periods and different initial orbital eccentricities and ran the evolution with each model until the orbital eccentricity dropped to the current eccentricity value of V454 Aur. Then, a χ^2 calculation was performed using the determined orbital period of the system, calculated radii, and temperature of the components with every model in the grid. In our calculations, we have activated the option of magnetic braking (Rappaport et al. 1983), since the components of V454 Aur

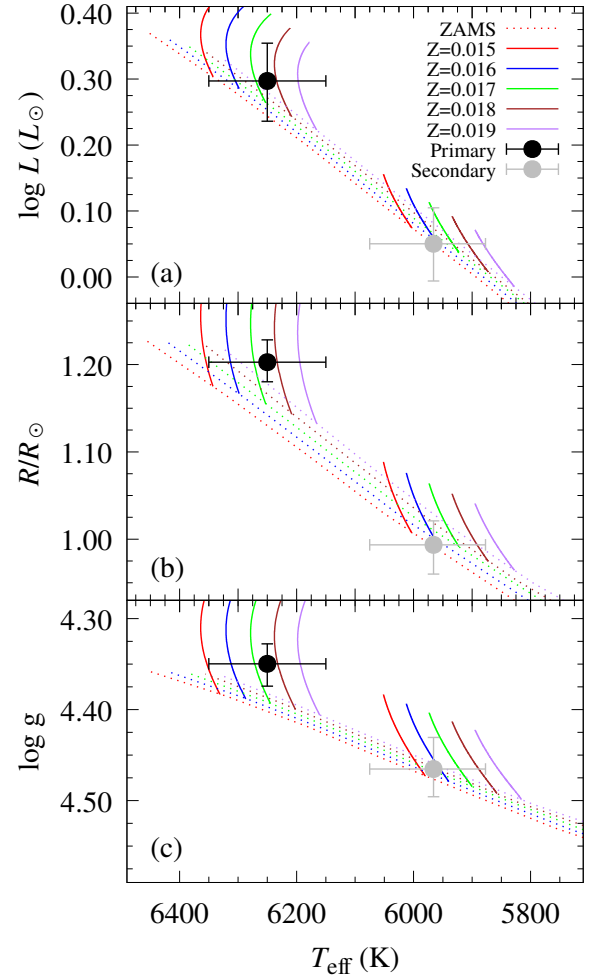


Figure 6. Single star evolutionary tracks with different metallicities for V454 Aur on (a) $T_{\text{eff}} - \log L$ plane, (b) $T_{\text{eff}} - R$ plane, and (c) $T_{\text{eff}} - \log g$ plane, respectively.

have convective atmospheres. For the tidal synchronisation, we used the “Orb_period” option, which synchronises the orbit relevant to the timescale of the orbital period. We also applied tidal circularisation, given by Hurley et al. (2002).

In the grid, the evolution models that the initial parameters change for the period and eccentricity between 27.020 and 27.040 d with an interval of 0.001 d and between 0.377190 and 0.377300 with an interval of 0.000005, respectively. We performed the evolution for each model and continued the evolution until eccentricity dropped to 0.377170, which is the up-to-date eccentricity value of V454 Aur. The best model gives, the lowest χ^2 , 0.00016, with initial orbital parameters for period and eccentricity of 27.021 and 0.377210, respectively (given in Figure 7).

Later, we started binary evolution with the determined initial orbital parameters and evolved the system until the primary star started mass transfer. According to our calculations, the age of the V454 Aur is 1.19 ± 0.09 Gyr. Taking the system as 6.23 Gyr, the mass transfer will start from the primary star, which will be on the red giant branch, to the secondary star, which will still

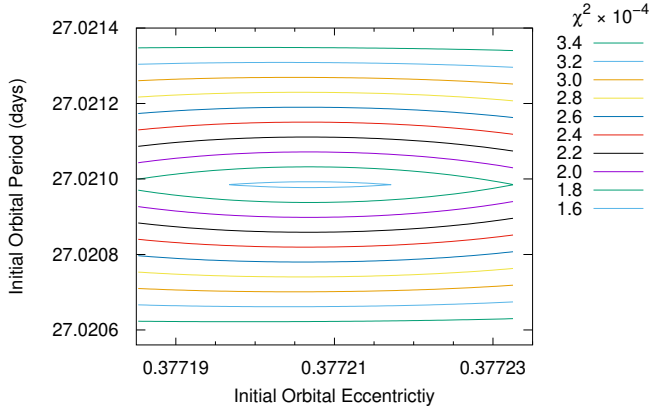


Figure 7. χ^2 map of the corresponding initial period for each initial orbital eccentricity of V454 Aur.

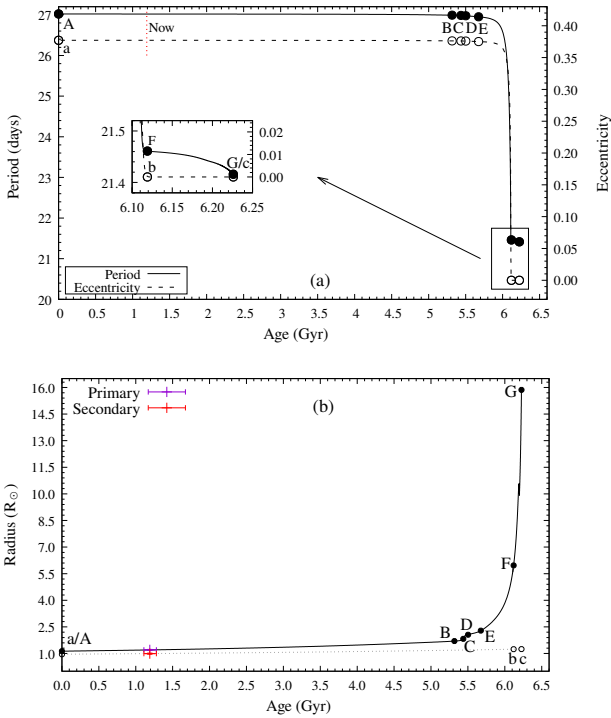


Figure 8. Change of orbital parameters (a), and radius of the components (b) of V454 Aur with time.

be on the main sequence. Changes in the orbital parameters and radii of the components during evolution are presented in Figure 8. Detailed evolution of both components of V454 Aur with timetables are given in Table 4 and shown in Figure 9.

5. KINEMATICS AND GALACTIC ORBIT PARAMETERS

At the beginning of the *Gaia* era, the sensitivity of astrometric measurements of stars in the Solar neighbourhood has increased. This enabled a more precise determination of the kinematic and dynamic orbital parameters of nearby stars. In this

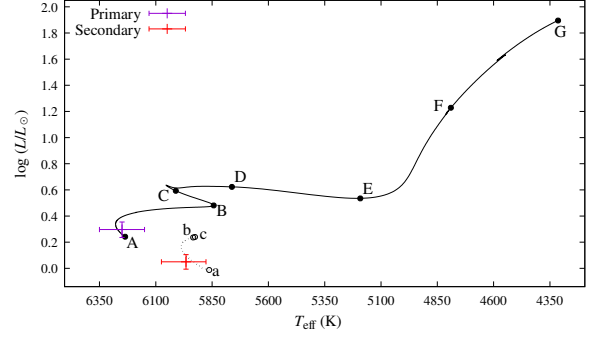


Figure 9. Evolution of V454 Aur on $T_{\text{eff}} - \log L/L_{\odot}$ diagram.

study, we have focussed on the analysis of V454 Aur, determining its space velocity components and Galactic orbital parameters. The proper motion components and trigonometric parallaxes of the system were obtained from the *Gaia* DR3 database (Gaia Collaboration et al. 2023), and the centre-of-mass velocities of the V454 Aur system, as determined in this study, are presented in Table 5.

The galpy code developed by Bovy (2015) was used to calculate the space velocity components for V454 Aur, and the uncertainties associated with these components were determined using the algorithm proposed by Johnson & Soderblom (1987). These space velocity components inherently incorporate biases due to the position of stars in the Milky Way and observations from the Sun. To correct for these biases, differential rotation and local standard rest (LSR) corrections have been applied to the velocity components of the stars. Differential rotational corrections for V454 Aur were applied using the equations mentioned by Mihalas & Binney (1981), obtaining velocity corrections of 0.04 and -0.15 km s^{-1} for the U and V space velocity components of the system, respectively. The W space velocity component, which is unaffected by differential rotation, was not corrected. For the LSR correction, the values of Coşkunoğlu et al. (2011) $(U, V, W)_{\odot} = (8.83 \pm 0.24, 14.19 \pm 0.34, 6.57 \pm 0.21) \text{ km s}^{-1}$ were considered, and the LSR values were extracted from the space velocity components for which a differential velocity correction was applied. The relation $S_{\text{LSR}} = \sqrt{U_{\text{LSR}}^2 + V_{\text{LSR}}^2 + W_{\text{LSR}}^2}$ was used to calculate the total space velocity (S_{LSR}) of the system, and the results are listed in Table 5. Considering the total space velocity and space velocity components of the V454 Aur, it is consistent with the value given for the young thin-disc population (Leggett 1992).

The galpy code (Bovy 2015) was also used to compute the Galactic orbital parameters of the V454 Aur. For the Galactic potentials needed for the Galactic orbit calculations, MWPotential2014 was used, which was created specifically for the Galaxy. For the system to form closed orbits around the Galactic centre, a timescale of 3 Gyr in 2 Myr steps was used. The Galactic orbital calculations resulted in the determination of several parameters, including the perigalactic distance (R_p),

Table 4. Detailed evolution of V454 Aur with time-stamps.

Comp	Mark	Evolutionary Status	Age (Gyr)	P (day)	e	Primary			Secondary		
						T_{eff} (K)	$\log L (L_{\odot})$	$R (R_{\odot})$	T_{eff} (K)	$\log L (L_{\odot})$	$R (R_{\odot})$
Pri	A	ZAMS	0	27.021	0.37721	6236	0.242	1.131	5863	-0.013	0.955
	B	Core contraction	5.32	26.991	0.37628	5843	0.481	1.699	5973	0.208	1.187
	C	TAMS	5.44	26.986	0.37615	6011	0.593	1.825	5969	0.213	1.194
	D	Thin H shell burning	5.50	26.978	0.37593	5762	0.623	2.056	5967	0.215	1.199
	E	Entering red giant phase	5.68	26.951	0.37519	5192	0.535	2.289	5959	0.221	1.210
	F	Circularisation of orbit	6.12	21.461	0	4790	1.228	5.968	5934	0.236	1.241
	G	Starting of mass transfer	6.23	21.416	0	4314	1.895	15.866	5926	0.240	1.248
Sec	a	ZAMS	0	27.021	0.37721	6236	0.242	1.131	5863	-0.013	0.955
	b	Circularisation of orbit	6.12	21.461	0	4790	1.228	5.968	5934	0.236	1.241
	c	Starting of mass transfer	6.23	21.416	0	4314	1.895	15.866	5926	0.240	1.248

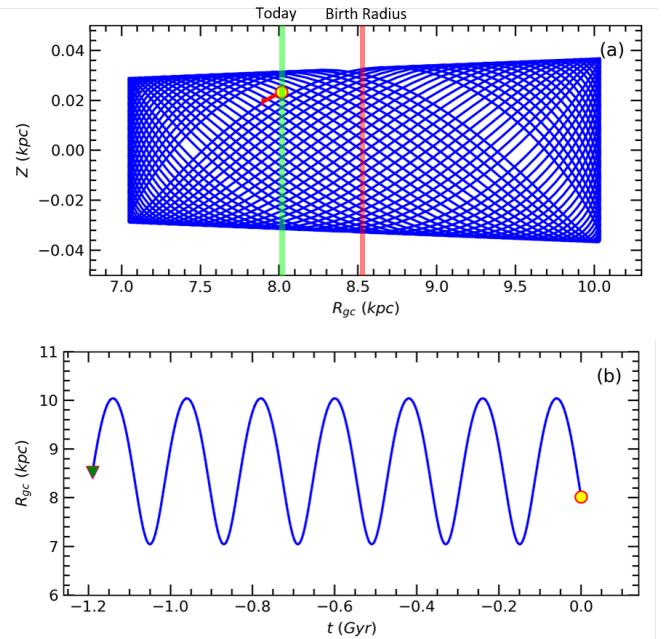
Table 5. Astrometric and radial velocity of V454 Aur and calculated space velocity components and Galactic orbital parameters of the system.

Star	α (J2000) (hh:mm:ss)	δ (J2000) (dd:mm:ss)	Input Parameters			Ref	V_{γ} (km s ⁻¹)	Ref
			$\mu_{\alpha} \cos \delta$ (mas yr ⁻¹)	μ_{δ} (mas yr ⁻¹)	ϖ (mas)			
V454 Aur	06:22:03.06	34:35:50.46	-0.514±0.025	-66.008±0.019	15.367±0.022	[1]	-40.48±0.10	[2]
Output Parameters								
Star	U_{LSR} (km s ⁻¹)	V_{LSR} (km s ⁻¹)	W_{LSR} (km s ⁻¹)	S_{LSR} (km s ⁻¹)	R_a (pc)	R_p (pc)	Z_{max} (pc)	e
V454 Aur	46.80±0.10	-4.61±0.03	-9.22±0.02	47.92±0.11	10038±40	7044±20	370±1	0.175±0.001

Ref: [1] Gaia Collaboration et al. (2023), [2] This study

apogalactic distance (R_a), maximum distance from the Galactic plane (Z_{max}), and eccentricity (e) of the Galactic orbits. These parameters are also listed in Table 5. The positions of the system according to their distances from the Galactic centre (R_{gc}) and perpendicular to the Galactic plane (Z) at different times are shown in Figure 10a. The galpy results show that the V454 Aur has a slightly flattened Galactic orbit. Moreover, the fact that the system is at $Z = 11$ pc ($Z = d \times \sin b$) from the Galactic plane indicates that V454 Aur may belong to the young thin-disc component of Milk Way (Tunçel Güçtekin et al. 2019).

Galactic orbits for the V454 Aur system on $Z \times R_{\text{gc}}$ and $R_{\text{gc}} \times t$ diagrams are shown in Figure 10. The panels in Figure 10 show side views of the V454 Aur motions as functions of distance from the Galactic centre and the Galactic plane, respectively (Tasdemir & Yontan 2023). In Figure 10b the birth and present-day positions of V454 Aur are shown with yellow-filled triangles and circles, respectively (Yontan et al. 2022). The eccentricity of the orbit of the V454 Aur does not exceed the value of 0.18. The distances from the Galactic plane reach a maximum at $Z_{\text{max}} = 370 \pm 1$ pc for V454 Aur. These results show that the V454 Aur belongs to the young thin disc of the Milky Way. The birthplace of the system was also investigated by running the binary system age ($t = 1.19 \pm 0.08$ Gyr) calculated in this work back in time using the galpy programme (Yontan & Canbay 2023). The birth radius of the


Figure 10. The Galactic orbits and birth radii of V454 Aur in the $Z \times R_{\text{gc}}$ (a) and $R_{\text{gc}} \times t$ (b) diagrams. The filled yellow circles and triangles show the current and birth positions, respectively. The red arrow is the motion vector of V454 Aur today. The green and pink dotted lines show the orbit when errors in input parameters are considered, whereas the green and pink filled triangles represent the birth locations of the V454 Aur based on the lower and upper error estimates.

binary system was determined as $R_{\text{Birth}} = 8.52 \pm 0.02$ kpc. These findings represent that the V454 Aur was born almost in the solar-abundance region around the Solar circle.

6. CONCLUSIONS

Eclipsing binary systems are the foundation for the studies of stellar astrophysics because they provide accurate stellar parameters that can be used in any area of astrophysics. In this study, we have derived, for the first time, the fundamental parameters of V454 Aur (HD 44192), including temperature, metallicity, and age, by combining photometric radial velocities, precise photometric data, and SED data. We calculated the mass of the components in V454 Aur better than 1.5% as $1.173 M_{\odot}$ and $1.045 M_{\odot}$ for the primary and secondary component, respectively, and the radii of the components better than 3% as $1.203 R_{\odot}$ and $0.993 R_{\odot}$ for the primary and the secondary component, respectively. Our distance calculation is in excellent agreement with the *Gaia* DR3 one (Gaia Collaboration et al. 2023), which is in the 2% error range, which indicates that our calculations are accurate. Mass-luminosity parameters that we have derived for the components are slightly smaller than Eker et al. (2018), which is expected considering the position of the V454 Aur on the main sequence. According to our evolution analysis, the components of V454 Aur are still in the main sequence and a little richer than solar metallicity, $z = 0.017$, and the system is far from mass transfer. The initial orbital parameters of the system were derived using the state-of-the-art evolutionary code MESA and evolutionary status in several phases were noted in Table 4. According to our calculations, the age of the system is $1.19^{+0.08}_{-0.09}$ Gyr, and it will start mass transfer between components in 5 Gyr when the primary component is in the red giant branch and the secondary component is still on the main-sequence. Calculations of detailed evolutionary steps for eclipsing binaries are important because these calculations generally could shed light on the properties of current semi-detached binaries.

Considering the dynamical orbital parameters and the age of the V454 Aur system, it was determined that it formed in a region around the Solar circle. This result is also consistent with the metal abundance assumed for the V454 Aur. There are still very few systems for which evolutionary phases and birthplaces have been revealed. We believe that determining the initial orbital properties of eclipsing binaries and the location of their birthplaces would help to understand the formation mechanism of eclipsing binaries in detail.

Peer Review: Externally peer-reviewed.

Author Contribution: Conception/Design of study - G.Y., R.C., V.B.; Data Acquisition - G.Y., R.C., V.B.; Data Analysis/Interpretation - G.Y., R.C., V.B.; Drafting Manuscript - G.Y., R.C., V.B.; Critical Revision of Manuscript - G.Y.; Final Approval and Accountability - G.Y.; Technical or Material Support - G.Y.

Conflict of Interest: Authors declared no conflict of interest.

Financial Disclosure: Authors declared no financial support.

Acknowledgements: We are grateful to the anonymous referees for their valuable suggestions. This paper includes data collected with the *TESS* mission, obtained from the MAST data archive at the Space Telescope Science Institute (STScI). Funding for the *TESS* mission is provided by the NASA Explorer Program. STScI is operated by the Association of Universities for Research in Astronomy, Inc., under NASA contract NAS 5–26555. This research has made use of the SIMBAD database, operated at CDS, Strasbourg, France. This work has made use of data from the European Space Agency (ESA) mission *Gaia* (<https://www.cosmos.esa.int/gaia>), processed by the *Gaia* Data Processing and Analysis Consortium (DPAC, <https://www.cosmos.esa.int/web/gaia/dpac/consortium>). Funding for the DPAC has been provided by national institutions, in particular, the institutions participating in the *Gaia* Multilateral Agreement. This research has made use of NASA’s Astrophysics Data System.

In addition to the Python packages referenced in section 3 and section 4, this research has made use of the following packages: Astropy (Astropy Collaboration et al. 2013, 2018, 2022), corner (Foreman-Mackey 2016), Matplotlib (Hunter 2007), NumPy (Harris et al. 2020), and SciPy (Virtanen et al. 2020).

LIST OF AUTHOR ORCIDS






G. Yücel	https://orcid.org/0000-0002-9846-3788
R. Canbay	https://orcid.org/0000-0003-2575-9892
V. Bakış	https://orcid.org/0000-0002-3125-9010

REFERENCES

- Angulo C., et al., 1999, *Nuclear Phys. A*, **656**, 3
- Astropy Collaboration et al., 2013, *A&A*, **558**, A33
- Astropy Collaboration et al., 2018, *AJ*, **156**, 123
- Astropy Collaboration et al., 2022, *ApJ*, **935**, 167
- Bakış V., Eker Z., 2022, *Acta Astron.*, **72**, 195
- Baranne A., Mayor M., Poncet J. L., 1979, *Vistas in Astronomy*, **23**, 279
- Benedict G. F., et al., 2016, *AJ*, **152**, 141
- Blouin S., Shaffer N. R., Saumon D., Starrett C. E., 2020, *ApJ*, **899**, 46
- Bovy J., 2015, *ApJS*, **216**, 29
- Casagrande L., Schönrich R., Asplund M., Cassisi S., Ramírez I., Meléndez J., Bensby T., Feltzing S., 2011, *A&A*, **530**, A138
- Cassisi S., Potekhin A. Y., Pietrinferni A., Catelan M., Salaris M., 2007, *ApJ*, **661**, 1094
- Chabrier G., 2003, *PASP*, **115**, 763
- Chugunov A. I., Dewitt H. E., Yakovlev D. G., 2007, *Phys. Rev. D*, **76**, 025028

- Coşkunoğlu B., et al., 2011, *MNRAS*, **412**, 1237
- Cybart R. H., et al., 2010, *ApJS*, **189**, 240
- Eggleton P. P., 1983, *ApJ*, **268**, 368
- Eker Z., Bakış V., 2023, *MNRAS*, **523**, 2440
- Eker Z., et al., 2015, *AJ*, **149**, 131
- Eker Z., et al., 2018, *MNRAS*, **479**, 5491
- Eker Z., Soyduğan F., Bilir S., 2024, *arXiv e-prints*, p. [arXiv:2402.07947](https://arxiv.org/abs/2402.07947)
- Ferguson J. W., Alexander D. R., Allard F., Barman T., Bodnarik J. G., Hauschildt P. H., Heffner-Wong A., Tamanai A., 2005, *ApJ*, **623**, 585
- Foreman-Mackey D., 2016, *The Journal of Open Source Software*, **1**, 24
- Foreman-Mackey D., Hogg D. W., Lang D., Goodman J., 2013, *PASP*, **125**, 306
- Fuller G. M., Fowler W. A., Newman M. J., 1985, *ApJ*, **293**, 1
- Gaia Collaboration et al., 2023, *A&A*, **674**, A1
- Griffin R. F., 2001, *The Observatory*, **121**, 315
- Harris C. R., et al., 2020, *Nature*, **585**, 357
- Holmberg J., Nordström B., Andersen J., 2009, *A&A*, **501**, 941
- Hunter J. D., 2007, *Computing in Science and Engineering*, **9**, 90
- Hurley J. R., Tout C. A., Pols O. R., 2002, *MNRAS*, **329**, 897
- Iglesias C. A., Rogers F. J., 1993, *ApJ*, **412**, 752
- Iglesias C. A., Rogers F. J., 1996, *ApJ*, **464**, 943
- Irwin A. W., 2004, *The FreeEOS Code for Calculating the Equation of State for Stellar Interiors*, <http://freeeos.sourceforge.net/>
- Itoh N., Hayashi H., Nishikawa A., Kohyama Y., 1996, *ApJS*, **102**, 411
- Jermyn A. S., Schwab J., Bauer E., Timmes F. X., Potekhin A. Y., 2021, *ApJ*, **913**, 72
- Jermyn A. S., et al., 2023, *ApJS*, **265**, 15
- Johnson D. R. H., Soderblom D. R., 1987, *AJ*, **93**, 864
- Kwee K. K., van Woerden H., 1956, *Bull. Astron. Inst. Netherlands*, **12**, 327
- Langanke K., Martínez-Pinedo G., 2000, *Nuclear Physics A*, **673**, 481
- Leggett S. K., 1992, *ApJS*, **82**, 351
- Lightkurve Collaboration et al., 2018, *Lightkurve: Kepler and TESS time series analysis in Python*, *Astrophysics Source Code Library* (ascl:1812.013)
- Mihalas D., Binney J., 1981, *Galactic astronomy. Structure and kinematics*
- Moe M., Di Stefano R., 2017, *ApJS*, **230**, 15
- Nordström B., et al., 2004, *A&A*, **418**, 989
- Oda T., Hino M., Muto K., Takahara M., Sato K., 1994, *Atomic Data and Nuclear Data Tables*, **56**, 231
- Paegert M., Stassun K. G., Collins K. A., Pepper J., Torres G., Jenkins J., Twicken J. D., Latham D. W., 2022, *VizieR Online Data Catalog: TESS Input Catalog version 8.2 (TIC v8.2)* (Paegert+, 2021), *VizieR On-line Data Catalog: IV/39*. Originally published in: 2021arXiv210804778P
- Paxton B., Bildsten L., Dotter A., Herwig F., Lesaffre P., Timmes F., 2011, *ApJS*, **192**, 3
- Paxton B., et al., 2013, *ApJS*, **208**, 4
- Paxton B., et al., 2015, *ApJS*, **220**, 15
- Paxton B., et al., 2018, *ApJS*, **234**, 34
- Paxton B., et al., 2019, *ApJS*, **243**, 10
- Perryman M. A. C., et al., 1997, *A&A*, **323**, L49
- Potekhin A. Y., Chabrier G., 2010, *Contributions to Plasma Physics*, **50**, 82
- Poutanen J., 2017, *ApJ*, **835**, 119
- Prša A., 2020, *Contributions of the Astronomical Observatory Skalnaté Pleso*, **50**, 565
- Prša A., Zwitter T., 2005, *ApJ*, **628**, 426
- Prša A., et al., 2022, *ApJS*, **258**, 16
- Rappaport S., Verbunt F., Joss P. C., 1983, *ApJ*, **275**, 713
- Ricker G. R., et al., 2015, *Journal of Astronomical Telescopes, Instruments, and Systems*, **1**, 014003
- Ritter H., 1988, *A&A*, **202**, 93
- Rogers F. J., Nayfonov A., 2002, *ApJ*, **576**, 1064
- Rosales J. A., Mennickent R. E., Schleicher D. R. G., Senhadji A. A., 2019, *MNRAS*, **483**, 862
- Saumon D., Chabrier G., van Horn H. M., 1995, *ApJS*, **99**, 713
- Serenelli A., et al., 2021, *A&ARv*, **29**, 4
- Soyduğan F., Soyduğan E., Aliçavuş F., 2020, *Research in Astronomy and Astrophysics*, **20**, 052
- Tasdemir S., Yontan T., 2023, *Physics and Astronomy Reports*, **1**, 1
- Timmes F. X., Swesty F. D., 2000, *ApJS*, **126**, 501
- Torres G., Andersen J., Giménez A., 2010, *A&ARv*, **18**, 67
- Townsend R., 2024, *MESA SDK for Linux*, [doi:10.5281/zenodo.10624843](https://doi.org/10.5281/zenodo.10624843), <https://doi.org/10.5281/zenodo.10624843>
- Tunçel Güçtekin S., Bilir S., Karaali S., Plevne O., Ak S., 2019, *Advances in Space Research*, **63**, 1360
- Virtanen P., et al., 2020, *Nature Methods*, **17**, 261
- Wilson R. E., 1979, *ApJ*, **234**, 1054
- Wilson R. E., 1990, *ApJ*, **356**, 613
- Wilson R. E., Devinney E. J., 1971, *ApJ*, **166**, 605
- Yontan T., Canbay R., 2023, *Physics and Astronomy Reports*, **1**, 65
- Yontan T., et al., 2022, *Rev. Mex. Astron. Astrofis.*, **58**, 333
- Yücel G., Bakış V., 2022, *MNRAS*, **516**, 2486
- van Hamme W., 1993, *AJ*, **106**, 2096
- van Hamme W., Wilson R. E., 2003, in *Munari U., ed., Astronomical Society of the Pacific Conference Series Vol. 298, GAIA Spectroscopy: Science and Technology*. p. 323

Effect of Annealing on Electronic Transport in Modulation-doped $\text{In}_{0.32}\text{Ga}_{0.68}\text{As}/\text{GaAs}$ Quantum Well Structures

A. Rajhi^{1,2} , M. Aydın^{1*} , Ö. Dönmez¹ , F. Sarcan¹ , and A. Erol¹ 

¹Istanbul University, Faculty of Science, Department of Physics, Vezneciler, 34134, İstanbul, Türkiye

²Al Zaytouna University, Faculty of Science, Department of Physics, Asalam, 325, Tarhuna, Libya

ABSTRACT

In this study, electronic transport properties of n-type modulation-doped $\text{In}_{0.32}\text{Ga}_{0.68}\text{As}/\text{GaAs}$ quantum well (QW) quasi 2D structures and the effects of post-growth rapid thermal annealing and growth temperature are determined. Electron Hall mobility and carrier concentration of $\text{In}_{0.32}\text{Ga}_{0.68}\text{As}/\text{GaAs}$ QW were determined using the Hall effect measurement at a temperature range between 4.2 K and 300 K. While the low-temperature electron mobility has temperature-independent behavior, electron mobility at high-temperatures deteriorates drastically. However, for low-temperature growth samples, electron mobility shows a slight increase at lower temperatures. The effects of annealing and growth temperature on electronic transport properties are investigated and compared in terms of carrier mobility, carried density, effective mass and scattering mechanisms. To determine the dominant scattering mechanisms in the 2D structures of $\text{In}_{0.32}\text{Ga}_{0.68}\text{As}/\text{GaAs}$, temperature-dependent Hall mobility results are fitted using an analytical model, considering all possible scattering mechanisms (interface roughness, alloy disorder, acoustic phonon, polar optical phonon and remote ionized impurity scattering) in the 2D samples. Magnetotransport (MR) measurements were carried out between 4.2 K and 50 K and the effective mass, Fermi level, and 2D carrier density were calculated by analyzing amplitudes of temperature dependence Shubnikov de Haas (SdH) oscillations. Our results indicate that the effects of annealing at 700°C-600s reduce interface roughness and alloy disorder scattering, thereby enhancing electron mobility. Post-growth thermal annealing improved electron mobility. Also, annealing increases the effect mass and causes a reduction in the electron concentrations of the $\text{InGaAs}/\text{GaAs}$ QW systems. Additionally, thermal annealing increases the effective electron mass while decreasing electron concentration.

Keywords: $\text{In}_{0.32}\text{Ga}_{0.68}\text{As}/\text{GaAs}$; 2D structures ; modulation doped structures ; electronic transport

1. INTRODUCTION

InGaAs alloy has been using in near-infrared applications as an active material for photodetectors and light emitters. The bandgap of the material can be tuned as a function of In concentration in the alloy. It has been shown in the literature that the band gap redshifts by 12 meV/In% (Petropoulos et al. 2011; Maspero et al. 2017; Lin et al. 2019). This tunability with In% concentration allows the desired bandgap in the active material for near-infrared optoelectronic device applications (Feng et al. 2005). Due to the increment in the lattice constant of alloy compared to GaAs host materials, substrate selection is critical (Matthews & Blakeslee 1974; Dahl 2002). While an InP substrate is suitable for the high In concentration, a GaAs substrate is suitable for the low In concentrations. InGaAs alloys grown by Molecular Beam Epitaxy (MBE) on GaAs require lower growth temperatures than those of growth on InP substrate to avoid defects, which cause poor electrical and optical properties such as low mobility, and low emission intensity (Mu-

raki et al. 1992; Toyoshima et al. 1993; Disseix et al. 1997). However, post-growth thermal annealing has been shown to have favorable effects on the electronic and optical properties of III-V group semiconductors (Ardali et al. 2021; Dönmez et al. 2020). Accordingly, rapid thermal annealing (RTA) provides a low-cost, simple, and powerful way to tune and improve the structural and optical qualities of nanostructures, such as bandgap energy, confinement, and absorption, and offers the potential to develop new types of devices and integrated optoelectronic circuits (Li et al. 2019). RTA is also used to reduce defects arising from low-growth temperatures by MBE (Kosogov et al. 1996). In a study on the effect of thermal annealing for InGaAs-GaAs strained-layer, it was shown that high temperature and prolonged thermal annealing have a significant effect on the diffusion coefficient (depending on annealing temperature, for 900°C it is about $8 \times 10^{-18} \text{cm}^2 \text{s}^{-1}$ and for 850°C it is about $8 \times 10^{-20} \text{cm}^2 \text{s}^{-1}$, respectively) (Kosogov et al. 1996; Joncour et al. 1985). It was reported that a blueshift occurred

Corresponding Author: M. Aydın **E-mail:** mustafaaydin@istanbul.edu.tr

Submitted: 05.10.2023 • **Accepted:** 19.12.2023 • **Published Online:** 05.06.2024



This article is licensed under a Creative Commons Attribution-NonCommercial 4.0 International License (CC BY-NC 4.0)

as the annealing time increased, attributed to the decrease in In alloy concentration. (Li et al. 2019; Aldridge et al. 2017; Kuphal 1984).

In this study, the effect of n-type modulation-doped thermal annealing at 700°C during 600 s on the electronic properties of In_{0.32}Ga_{0.68}As/GaAs quantum well (QW) structure grown at 475°C (TNL) and 580°C (TNH) was investigated. Hall Effect experiments between 4K and 300K were performed to analyze the electronic properties of n-type as-grown and annealed InGaAs/GaAs QWs grown at different temperatures. The results of Hall Effect experiments were analyzed taking into account the scattering mechanisms of interface roughness, alloy disorder, acoustic phonon, polar optical phonon and remote ionized impurity scatterings. MR experiments were performed between 4K and 50K. Shubnikov-de Haas (SdH) oscillations were observed in MR experiments. These oscillations were analyzed to determine the 2D carrier concentration, the position of the Fermi level, and the effective mass of all samples.

2. METHODS

2.1. Sample Growth and Fabrication

Samples were grown as reference examples to compare the electronic transport mechanism of the N-containing samples. For this reason, the growth process using Molecular Beam Epitaxy (MBE) was carried out at two different temperatures: the low temperature (475°C) at which the crystal quality of the nitrogen-containing structures obtained the best and the optimum temperature (580°C) of the GaAs-based samples. We have also studied the effect of growth temperature, investigated growth temperatures and the electronic transport mechanisms of the samples after thermal annealing. The samples were subjected to 600s thermal annealing at 700°C to investigate the effects of thermal annealing. The sample structure is illustrated in Figure 1. The samples were grown on a semi-insulating (SI) GaAs substrate that does not affect its electrical properties and acts as a passive substrate. The structure consists of an n-type doped GaAs barrier and undoped InGaAs layer that forms the QW. Si dopant concentration (N_D) was 10^{18}cm^{-3} . GaAs layers were grown at 580°C while the InGaAs layer forming QW was grown at 475°C for TNL and 580°C for TNH. Modulation doping was achieved by growing an undoped spacer GaAs layer with a thickness of 5nm between the doped barrier layer and the QW in order to spatially separate the carriers passing through the QW from the barrier, with their ionized parents in the barrier, and weaken the Coulomb interaction between them. The sample was then fabricated into a Hall Bar shape using a wet etching process. Hall bar dimensions are given in Figure 1b.

2.2. Theoretical Background: Analytic modeling of temperature dependence of electron mobility

This section will discuss several scattering mechanisms, such as acoustic phonon scattering (μ_{APH}), alloy disorder scattering (μ_{Alloy}), interface roughness scattering (μ_{IFR}), and remote

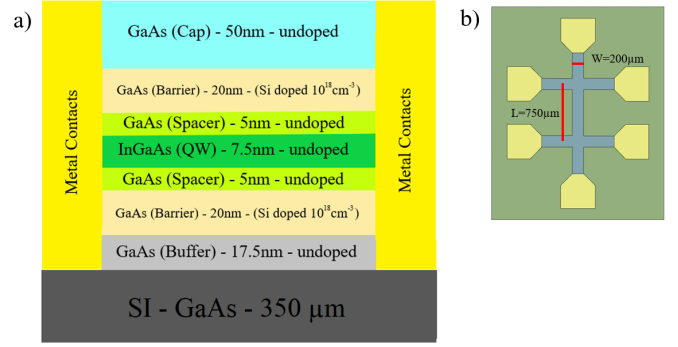


Figure 1. (a) Modulation-doped In_{0.32}Ga_{0.68}As/GaAs QW sample structure, (b) Fabricated Hall Bar shape and its dimensions.

impurity scattering (μ_{RI}), which play a significant role in determining carrier mobility in a semiconductor.

2.2.1. Interface Roughness Scattering

In layered structures like modulation-doped structures, interface roughness scattering is a crucial scattering mechanism due to imperfections at the interface between different materials. Because the sample is grown layer by layer, and the layers consist of different materials with different lattice constants and dielectric constants, roughness will occur at the interface between the layers, resulting in interface scattering. Interface roughness scattering mobility can be written as (Donmez et al. 2021, 2014),

$$\mu_{\text{IFR}} = \left(\frac{2\varepsilon_0\varepsilon_s}{n_{2D}\Delta\Lambda} \right)^2 \frac{\hbar^3}{e^3 m^*{}^2} \frac{1}{j_{\text{IFR}}(k)} \quad (1)$$

Here n_{2D} is the 2D carrier density, and Δ denotes the lateral size of the interface roughness, and Λ stands for the correlation length between fluctuations. The integral $J_{\text{IFR}}(k)$ is given by Zanato et al. (2004),

$$J_{\text{IFR}}(k) = \int_0^{2k} \frac{e^{-q^2\Lambda^2/4}}{2k^3(q + q_{2D})\sqrt{1 - (\frac{q}{2k})^2}} q^4 dq \quad (2)$$

where $q = 2 \sin(\theta/2)$, θ represents the scattering angle, and q_{2D} denotes the inverse screening length.

2.2.2. Alloy Disorder Scattering

Alloy fluctuation scattering is caused by potential fluctuations due to the random distribution of the atoms forming an alloy in the crystal. Alloy disorder scattering is given by

$$\mu_{\text{Alloy}} = \frac{16e\hbar^3}{3b_{\text{FH}} \times (1-x)m^*{}^2\Omega_0 U_{\text{Alloy}}^2} \quad (3)$$

where x is the alloy content, the primitive cell volume, Ω_0 , the effective mass of the carrier, m^* , for ternary alloys, the potential alloy, U_{Alloy} , and factor b_{FH} is the Fang-Howard expression (Donmez et al. 2021).

2.2.3. Acoustic Phonon Scattering

Acoustic phonons are divided into two branches: transverse and longitudinal acoustic phonons, depending on the transverse and longitudinal oscillations of atoms. The acoustic phonon scattering increases with temperature, because the density of phonons increases at higher temperature according to Bose-Einstein statistics. Acoustic phonon scattering includes deformation potential scattering and piezoelectric scattering.

Deformation Potential Scattering

The deformation potential limited mobility is defined by *Ridley* (Zanato et al. 2004) as

$$\mu_{DP} = \frac{16\rho e\vartheta_L^2\hbar^3}{3E_{DP}^2 k_B T m^{*2} b_{FH}} \frac{1}{j_{DP}(k)} \quad (4)$$

where ρ , E_{DP} , ϑ_L , b_{FH} are the crystal density, deformation potential, longitudinal acoustic phonon velocity and Fang-Howards expression, respectively. $J_{DP}(k)$ is given as

$$J_{DP}(k) = \int_0^{2k} \frac{1}{2\pi k^3 (q + q_{2D})^2 \sqrt{1 - (\frac{q}{2k})^2}} q^4 dq \quad (5)$$

Piezoelectric Scattering

The mobility limited by piezoelectric scattering is defined as (Donmez et al. 2021, 2014),

$$\mu_{PE} = \frac{\pi\varepsilon_0\varepsilon_s\hbar^3 k}{eK_{av}^2 k_B T m^{*2}} \frac{1}{j_{PE}(k)} \quad (6)$$

Here K_{av} is the average electromechanical coupling constant. $J_{PE}(k)$ is given as

$$J_{PE}(k) = \int_0^{2k} \frac{F(q)}{4k^2 (q + q_{2D})^2 \sqrt{1 - (\frac{q}{2k})^2}} q^3 dq \quad (7)$$

2.2.4. Polar Optical Phonon Scattering

Optical phonon scattering becomes more effective at higher temperatures. The mobility restricted by polar optical phonon scattering is expressed as (Donmez et al. 2021, 2014):

$$\mu_{PE} = \frac{4\pi\varepsilon_0\varepsilon_p\hbar^2}{e\omega_{PO}m^{*2}L} \left[\exp\left(\frac{\hbar\omega_{PO}}{k_B T}\right) - 1 \right] \quad (8)$$

where $\hbar\omega_{PO}$ is polar optical phonon energy and L quantum well width. ε_p is defined as

$$\varepsilon_p = \left[\frac{1}{\varepsilon_\infty} - \frac{1}{\varepsilon_s} \right]^{-1} \quad (9)$$

2.2.5. Remote Ionized Impurity Scattering

Remote ionized impurity scattering is caused by ionized doping atoms and is a Coulombic interaction between charge carriers in the QW and the ionized impurities in the barrier layer. Compared to the ionized impurity scattering, remote scattering is less effective in modulation-doped structures, where dopant atoms and carriers are spatially distant from each other, thus reducing scattering and improving electron mobility. The mobility limited by scattering of remote ionized impurity atoms is expressed as (Donmez et al. 2021, 2014),

$$\mu_{RI} = \left(\frac{64\pi\hbar\varepsilon_0 S_0^2 (2\pi n_{2D})^{3/2}}{e^3 m^*} \right)^2 \left[\frac{1}{L^2} - \frac{1}{(d_1 + L)^2} \right]^{-1} \quad (10)$$

where d_1 , L and S_0 are the spacer layer thickness, QW width and static constant, respectively. S_0 is defined as the screening constant (Donmez et al. 2020, 2014).

2.2.6. Matthiessen Rule

The effect of summing each kind of scattering center can be expressed with the assumption that each scattering mechanism is independent of each other, using the formula developed by Matthiessen as,

$$\frac{1}{\mu_{Total}} = \sum_i \frac{1}{\mu_i} \quad (11)$$

2.3. Theoretical Background: Analysis of Shubnikov-de Haas (SdH) Oscillations

In low-dimensional semiconductor systems, the energy difference between two subsequent Landau levels increases with the increasing magnetic field applied to the semiconductor in the growth direction. The Landau levels expand and approach the Fermi level, and if the magnetic field intensity is sufficient, the Landau levels pass through the Fermi level. As a result, oscillations occur at the density at the Fermi level, so the longitudinal resistivity (ρ_{xx}) oscillates. These oscillations are called Shubnikov-de Haas (SdH) oscillations.

$$\rho_{xx}(B) = \rho_{non-osc}(B) + \rho_{ocs}(B) \quad (12)$$

Experimental results provide the total of non-oscillating part and SdH oscillations. Considering that the effective mass and quantum lifetime can be different for each subband, the analytical expression for SdH oscillations is as follows (Coleridge 1990; Balkan et al. 1995):

$$\frac{\Delta\rho_{xx}}{\rho_0} \sim \sum_{i=1}^{\infty} D(i\chi) \exp\left(\frac{-i\pi}{\omega_c \tau_q}\right) \cos\left[\frac{2\pi(E_F - E_i)}{\hbar\omega_c} - i\pi\right] \quad (13)$$

where ρ_{xx} , ρ_0 , E_1 , E_F , ω_c and τ_q are oscillatory part of magnetoresistivity, magnetoresistivity, first sub-band energy, Fermi energy, cyclotron frequency and quantum lifetime, respectively.

i , represents the sub-bands. $\exp\left(\frac{-i\pi}{\omega_c \tau_q}\right)$ represents damping due to the broadening of the levels resulting from the collision of the Landau levels. $D(i\chi)$ describes the temperature damping as follows:

$$D(i\chi) = \frac{\chi}{\sinh \chi} \quad (14)$$

$$\chi = \frac{2\pi^2 k_B T}{\hbar \omega_c} \quad (15)$$

Assuming that the quantum lifetime of the electron is independent of temperature, the oscillation amplitude is expressed as

$$A(T, B_n) = C_1 \frac{2\pi^2 k_B T / \hbar \omega_c}{\sinh(2\pi^2 k_B T / \hbar \omega_c)} \quad (16)$$

where C_1 is constant. The ratio of the amplitudes of the oscillations at two different temperatures gives

$$\frac{A(T, B_n)}{A(T_0, B_n)} = \frac{T \sinh(2\pi^2 k_B T_0 m^* / \hbar \omega_c)}{T_0 \sinh(2\pi^2 k_B T m^* / \hbar \omega_c)} \quad (17)$$

The experimental data obtained for the variation of the relative amplitude with temperature are fitted to Equation 17 to obtain the effective mass with high accuracy. The position of the Fermi level and n_{2D} is also determined by Equation 18 using the slope of the inverse magnetic field plot versus the number of oscillation peaks.

$$\Delta_i \left(\frac{1}{B} \right) = \frac{e\hbar}{m^*(E_F - E_i)} = \frac{e}{\pi \hbar n_{2D}} \quad (18)$$

3. RESULTS

3.1. Low Magnetic Field Results

Hall measurements were conducted to determine carrier mobility and carrier concentration under a constant magnetic field in the temperature range of 4.2 to 300K.

Figure 2 a-b shows the temperature-dependent mobility and electron density of all samples. The temperature dependence of the electron mobility exhibits the well-known characteristic of modulation-doped structures. At low temperatures ($T < 77K$), electron mobility is almost the temperature-independent where ionized impurity scattering is dominant in conventional doped heterostructures. Thanks to the modulation doping, we observed that the mobility is very high for all samples at temperature lower than 77 K. The highest mobility ($43121 \text{ cm}^2 \text{ V}_s^{-1}$) for as-grown samples are observed for TNL at low temperatures ($T < 100K$) and the lowest mobility ($15362 \text{ cm}^2 \text{ V}_s^{-1}$) belongs to the TNH even though it was grown at almost the optimum growth temperature for InGaAs alloy. After the annealing process, the electron mobility of high-temperature growth samples improved and almost became equal to the mobility of as-grown and annealed low-temperature growth sample's

electron mobility. It is evident that thermal annealing causes a slight improvement at all temperature ranges of interest for the low-temperature growth sample. After annealing, the low-temperature electron mobility is almost the same for both TNLB and TNHB samples. Therefore, it can be inferred that annealing has a significant effect for the high-temperature growth sample. The temperature-dependent carrier concentration changes of samples with and without annealing are shown in Figure 2b. Considering the TNH sample, a slight gradual increase in carrier concentration with increased temperature was observed where the highest value is recorded as $2.92 \times 10^{12} \text{ cm}^{-2}$ at 300K. After thermal annealing, we noted a decrease in carrier concentration to $2.4 \times 10^{12} \text{ cm}^{-2}$ at 300K.

To compare the effect of growth temperature and also thermal annealing on carrier mobility, analytical calculations of temperature-dependent mobility changes of as-grown and annealed samples are given in Figure 3 considering all possible scattering mechanisms. For all samples, the low-temperature electron mobility was restricted by alloy and interface roughness scattering mechanisms. Scattering caused by polar optical scattering dominates the mobility in the high-temperature samples. The interface roughness scattering resulted from two parameters, the lateral size ($\Delta=1.9a$ for TNH and $1.3a$ for TNLB) and the correlation length (Λ), which is used as adjustable parameters to fit the experimental data.

In addition, the alloy potential was used to determine the alloy disorder scattering mechanism. The values obtained are given in Table 1. with the values for the reference sample.

Table 1. Alloy potentials and correlation lengths for n-type $\text{In}_{0.32}\text{Ga}_{0.68}\text{As}/\text{GaAs}$ samples.

Sample	U_{Alloy} (eV)	(Λ) (nm)
TNL	0.445	1.3
TNLB	0.3	0.9
TNH	0.537	29.8
TNHB	0.487	0.7

The match between the experimental and calculated values for electron mobility was obtained at low temperatures for all samples, as given in Figure 3. The best match was obtained in the as-grown samples over all temperature ranges a slight deviation between experimental and calculated mobility was observed at temperatures higher than 77K. Also, increasing electron mobility was observed after annealing. From Figure 3, decreased contribution was observed for alloy disorder scattering and interface roughness scattering after thermal annealing. The optimum electronic transport properties, characterized by the lowest alloy potential and correlation length, were observed for the low-temperature growth sample. Following thermal annealing, the interface roughness was reduced for this sample. Since the mobility is lower for the sample grown at a higher temperature, thermal annealing is more effective in smoothing the interface.

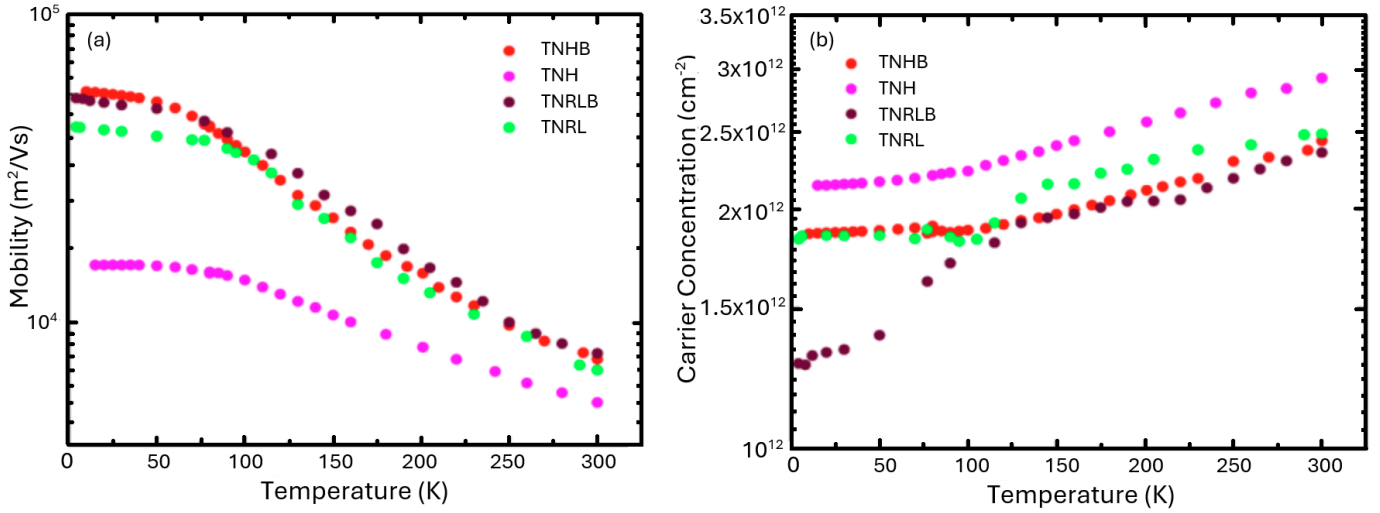


Figure 2. For all samples temperature-dependence of (a) Hall mobilities and (b) carrier concentrations.

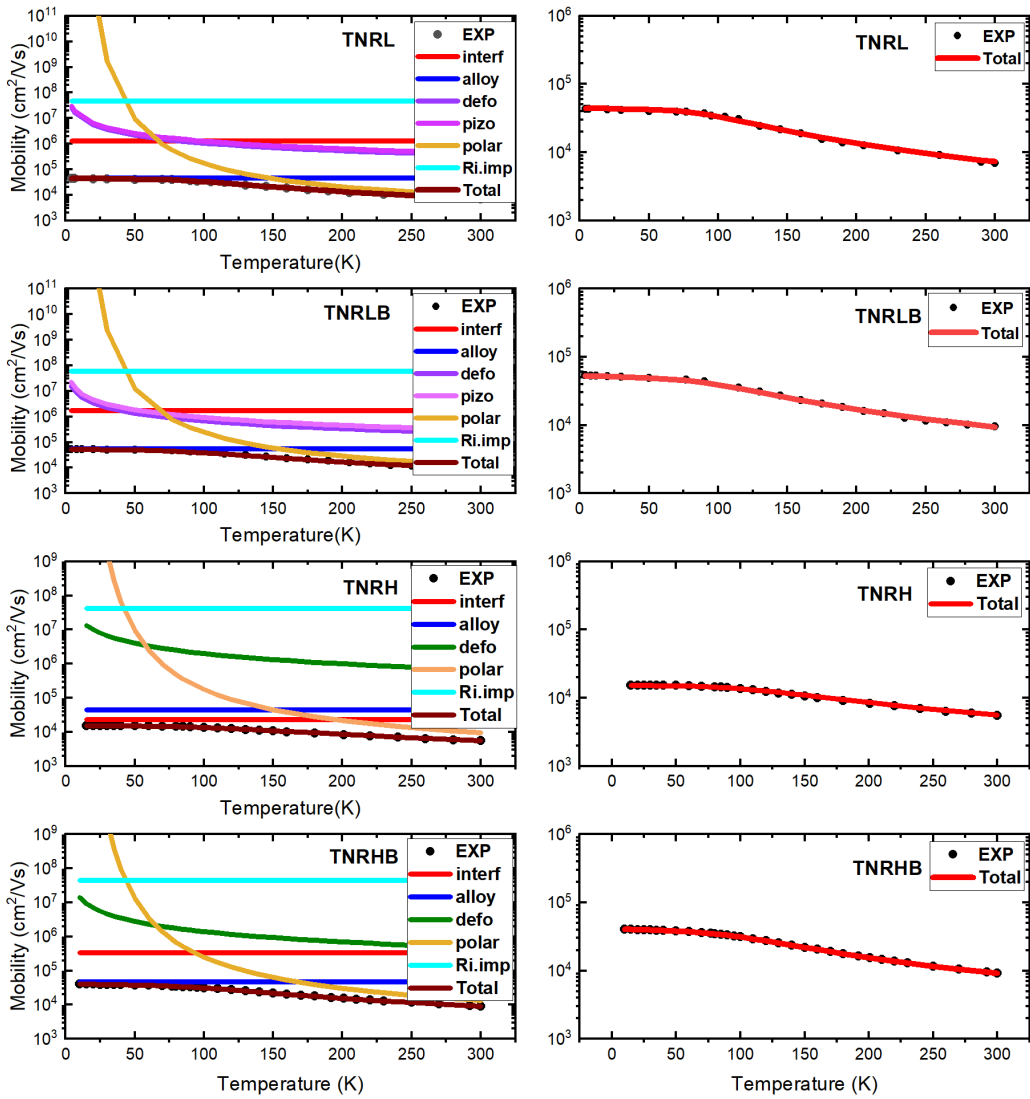


Figure 3. Analytical calculation of the temperature-dependent mobility of the samples.

Table 2. Variable parameters.

Parameters	Values
Optical phonon energy in GaInAs, $\hbar\omega_{po}$ (meV)	34
Optical phonon energy in GaAs, $\hbar\omega_{po}$ (meV)	35
Longitudinal acoustic phonon velocity, v_L (ms^{-1})	5087
Static dielectric constant, $\epsilon_s(\epsilon_0)$	13.9
High frequency dielectric constant, $\epsilon_\infty(\epsilon_0)$	11.11

Consequently, a significant enhancement was observed for the annealed high-temperature sample. Table 2 shows variable parameters used for calculation.

It has been reported that for In compositions greater than 0.2, InGaAs growth on GaAs results in In surface segregation at high-temperature growth. Thermal stability of InGaAs QW material requires low-temperature growth at around 400-500°C, but GaAs barrier material has to be grown at higher temperatures (around 580°C) (Toyoshima et al. 1993; Disseix et al. 1997). A strong temperature dependence of In segregation was revealed for InGaAs/GaAs QW structures with a segregation length of more than 30Å at temperatures above 600°C (Disseix et al. 1997). The surface segregation of In atoms drastically limits perfect abrupt interface between GaAs and InGaAs (Disseix et al. 1997). Despite several methods being used to solve this problem, the growth of high-quality InGaAs/GaAs QW structures remains a challenge. Therefore, we observed higher electron mobility for the sample grown at lower temperatures. However applying thermal annealing was found to be a solution to enhance mobility for high-temperature growth InGaAs/GaAs QW structures.

3.2. High Magnetic Field Results

MR measurements were carried out by sweeping the magnetic field value in the magnetic field range of 0-7T for TNL and TNLB samples and 0-18T for TNH and TNHB samples with different temperatures. SdH oscillations clearly appear at very low-magnetic fields due to the electron mobility values are so high for all samples as it can be seen in Figure 4. The MR curves for low-temperature growth as-grown (TNL) and annealed (TNLB) samples exhibit complicated characteristics, with both the period and shape of oscillations changing with increasing magnetic field. Experimentally observed magnetoresistance is the sum of classical magnetoresistance and SdH oscillations. To eliminate background magnetoresistance, the negative of the second derivative of the raw magnetoresistance data with respect to the magnetic field were taken, and are shown in Figure 5. The SdH oscillations in the second derivative of MR exhibit well-defined envelopes. As seen in Figure 4, the MR curve for high-temperature growth samples have a linearly increasing classical MR background with increasing magnetic field for the as-grown sample. For the annealed high temperature growth sample (TNHB), a slight deviation from linearity was observed above approximately 4T, while the

background MR characteristics exhibited linearity below 3.5T but deviated above 3.5T. Therefore, to be able to apply this second derivation method, only a low magnetic field range (<4T) was used for the samples apart from TNLB. As for TNLB, even at the low magnetic field range it was impossible to fit the oscillations using the standard expression given by Equation 14, but it is obtained well-defined SdH oscillations at higher magnetic field range, as seen in Figure 4b. However, the MR curves became more complicated at higher magnetic fields, as can be seen in Figure 4a, with an anomalous background MR. Even if the data is used to determine transport parameters of TNLB, it is clear these parameters cannot be compared with the transport parameters of other samples because they cannot be obtained at a similar magnetic field range. Effective electron mass values were obtained by proportioning the amplitudes of the SdH oscillations given in Figure 5 at a given magnetic field value and using Equation 17.

Figure 6 shows a plot of $\frac{1}{B}$ versus the peaks numbers for TNL and TNLB samples. Using the slopes of Figure 6 positions of Fermi level and N_{2D} (carrier concentration) for TNL and TNLB were obtained. All results obtained is given Table 3.

Table 3. Carrier density (N_{2D}), position of Fermi level and effective mass values obtained by analyzing SdH oscillations.

Sample	N_{2D} ($\times 10^{12} \text{ cm}^{-2}$)	$(E_F - E_i)$ (meV)	$m^*(m_0)$
TNL	1.74	71	0.057
TNLB	1.73	60	0.070
TNH	2.02	122	0.050
TNHB	1.92	82	0.055

4. CONCLUSION

Analysis of the temperature-dependent electron mobility showed that the 700°C thermal annealing had a significant improvement in the crystal structure. For the two samples grown at optimum and low growth temperature, the electronic properties of the sample at low growth temperature were superior in terms of electron mobility, alloy potential, and correlation length. Moreover, the post-growth thermal annealing at 700°C-600s improved the electronic properties of both samples at the growth temperature. According to the calculated transport parameters given in Table 3, the sample TNL had the lowest 2D carriers and the highest effective mass. Since the effective mass was larger, the density of states was higher, and therefore the Fermi level was smaller than those for TNH and TNHB samples. We exclude TNLB from the discussion because the analysis of this sample resulted in higher magnetic fields than the others. The 2D carrier density was the highest for TNH and the effective mass was the smallest, which resulted in the highest Fermi level. When the sample was annealed, 2D carrier density decreased and effective mass increased. The effective mass values became comparable for TNL and TNHB samples.

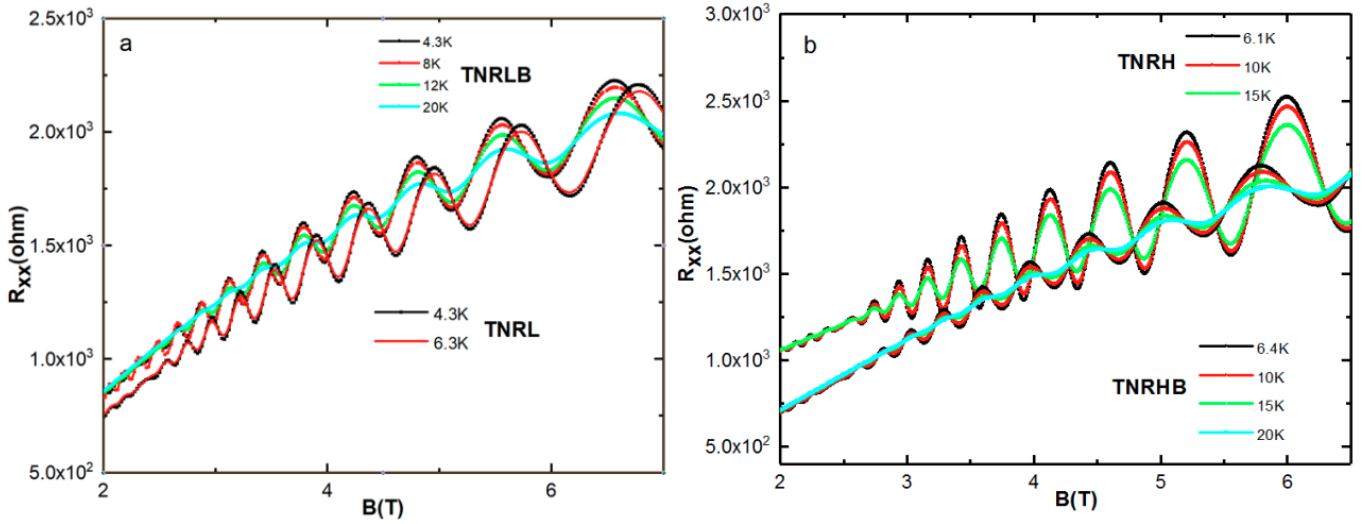


Figure 4. MR results of (a) TNL and TNLB, (b) TNH and TNHB.

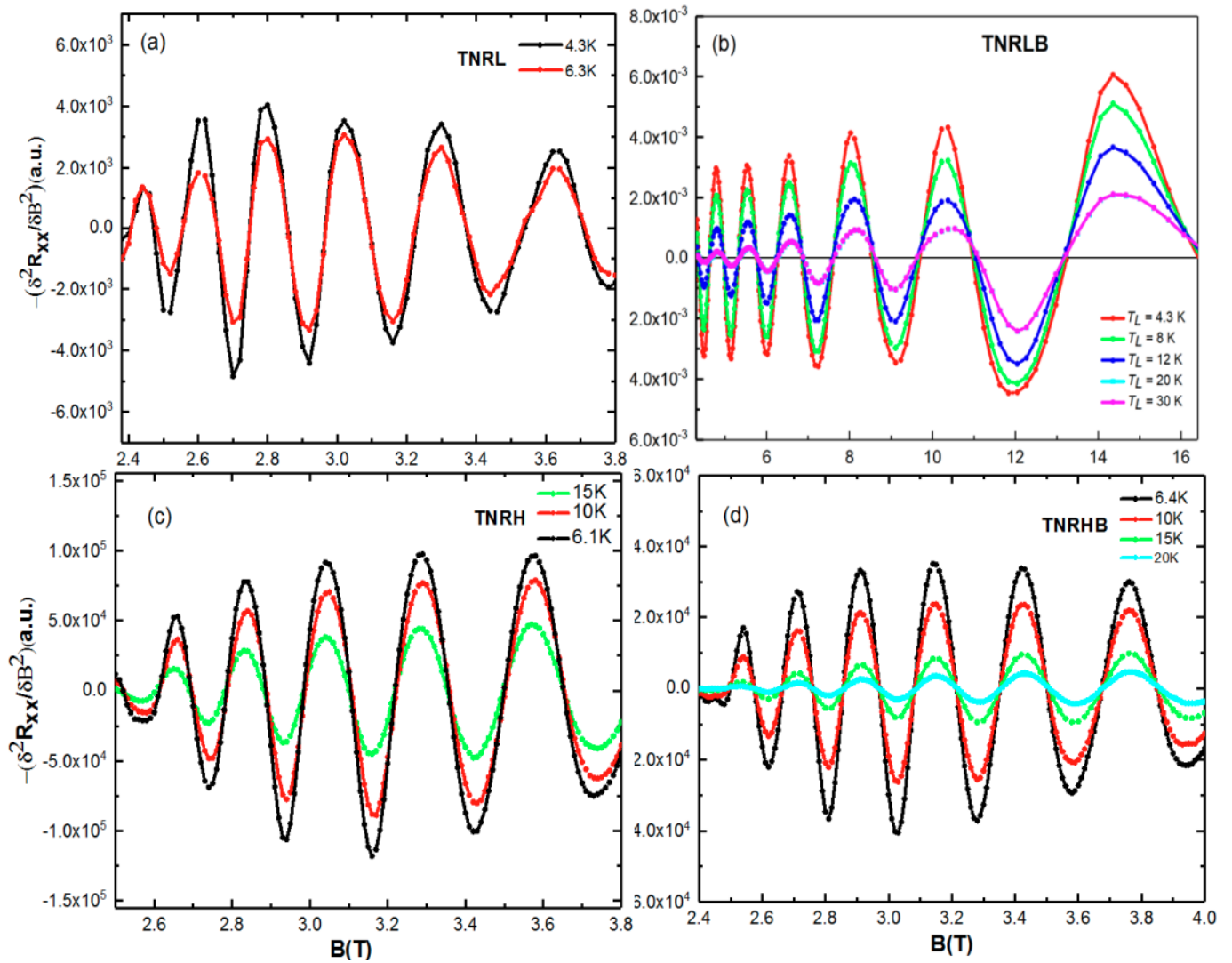


Figure 5. Negative second derivative of SdH oscillations for MR of (a) TNL, (b) TNLB, (c) TNH, and (d) TNHB.

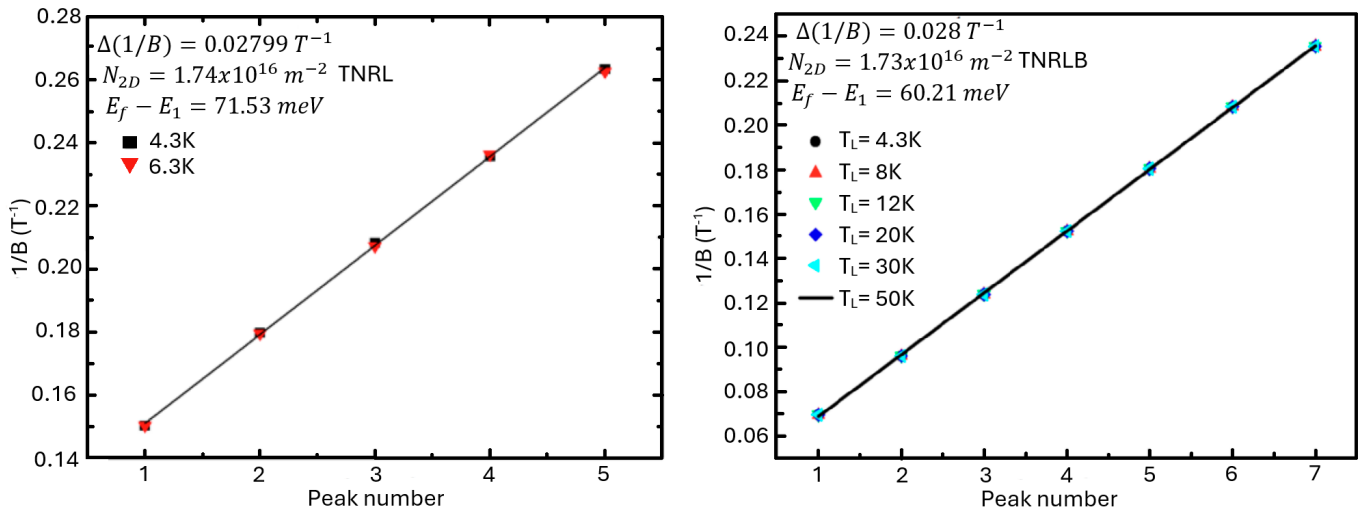


Figure 6. Plot of $1/B$ versus peak numbers for TNL (left panel) and TNLB (right panel).

The highest electron mobility for TNL sample was grown at a low temperature. The interface roughness for the TNL sample compared to the others was found to be the least. For all samples the alloy disorder scattering and interface roughness scattering were the prevailing scattering mechanisms. It was found that the alloy potential took a value of 0.445 eV for TNL and it was 0.537 eV for TNH. Following thermal annealing, an improvement in carrier mobility was observed. Additionally, a decrease in the correlation length was noted after the thermal annealing process, suggesting a reduction in interface roughness.

Peer Review: Externally peer-reviewed.

Author Contribution: Conception/Design of study - A.R., M.A., Ö.D., F.S., A.E.; Data Acquisition - A.R., M.A., Ö.D., F.S., A.E.; Data Analysis/Interpretation - A.R., M.A., Ö.D., F.S., A.E.; Drafting Manuscript - M.A., Ö.D., F.S., A.E.; Critical Revision of Manuscript - A.R., M.A., Ö.D., F.S., A.E.; Final Approval and Accountability - A.R., M.A., Ö.D., F.S., A.E.; Technical or Material Support - A.R., M.A., Ö.D., F.S., A.E.; Supervision - A.R., M.A., Ö.D., F.S., A.E.

Conflict of Interest: Authors declared no conflict of interest.

Financial Disclosure: This study was supported by the Scientific Research Projects Coordination Unit of Istanbul University (Project IDs: FBG-2022-38573, FBG-2021-37975, FBG-2018-30048).


LIST OF AUTHOR ORCIDS

A. Rajhi <https://orcid.org/0009-0009-1229-6965>
M. Aydın <https://orcid.org/0000-0002-1002-6007>
Ö. Dönmez <https://orcid.org/0000-0002-7635-3991>
F. Sarcan <https://orcid.org/0000-0002-8860-4321>
A. Erol <https://orcid.org/0000-0003-4196-1791>

REFERENCES

- Aldridge H., Lind A. G., Bomberger C. C., Puzyrev Y., Zide J. M., Pantelides S. T., Law M. E., Jones K. S., 2017, *Materials Science in Semiconductor Processing*, 62, 171
- Ardali S., Taganov S., Erol A., Tiras E., 2021, *Physica E: Low-Dimensional Systems and Nanostructures*, 125, 114344
- Balkan N., Çelik H., Vickers A. J., Cankurtaran M., 1995, *Physical Review B*, 52, 17210
- Coleridge P. T., 1990, *Semiconductor Science and Technology*, 5, 961
- Dahl D., 2002, *Solid State Communications*, 124, 825
- Disseix P., Leymarie J., Vasson A., Monier C., Grandjean N., Leroux M., Massies J., 1997, *Physical Review B - Condensed Matter and Materials Physics*, 55, 2406
- Donmez O., et al., 2014, *Semiconductor Science and Technology*, 29
- Donmez O., et al., 2020, *Semiconductor Science and Technology*, 35, 10
- Donmez O., et al., 2021, *Semiconductor Science and Technology*, 36, 11
- Feng G., Yoshimoto M., Oe K., Chayahara A., Horino Y., 2005, *Japanese Journal of Applied Physics, Part 2: Letters*, 44, 3
- Joncour M., Charasse M., Burgeat J., 1985, *Journal of Applied Physics*, 58, 3373
- Kosogov A. O., et al., 1996, *Applied Physics Letters*, 69, 3072
- Kuphal E., 1984, *Journal of Crystal Growth*, 67, 441
- Li W., et al., 2019, *Journal of Applied Physics*, 125
- Lin A., Doty M. F., Bryant G. W., 2019, *Phys. Rev. B*, 99, 075308
- Maspero R., Sweeney S. J., Florescu M., 2017, *Journal of Physics Condensed Matter*, 29, 075001
- Matthews J. W., Blakeslee A., 1974, *Journal of Crystal Growth*, 27, 118
- Muraki K., Fukatsu S., Shiraki Y., Ito R., 1992, *Applied Physics Letters*, 61, 557
- Petropoulos J. P., Zhong Y., Zide J. M., 2011, *Applied Physics Letters*, 99
- Toyoshima H., Niwa T., Yamazaki J., Okamoto A., 1993, *Applied Physics Letters*, 63, 821
- Zanato D., Gokden S., Balkan N., Ridley B. K., Schaff W. J., 2004, *Semiconductor Science and Technology*, 19, 427

Investigation of Adsorption of the Cardiotonic Drug Milrinone Onto Montmorillonite: An FTIR and Raman Spectroscopic Study

S. Akyuz^{1*} 

¹Istanbul Kültür University, Science and Letters Faculty, Physics Department, 34156, Bakirkoy, İstanbul, Türkiye

ABSTRACT

Milrinone is a cardiotonic drug that is used for the treatment of congestive heart failure. Clay minerals are widely used materials as a low-cost nanocarriers in designing drug delivery systems. Drug-clay interaction is important since it affects drug action. Montmorillonite, a clay mineral with high adsorption and swelling properties, is useful as a low-cost nanocarrier in designing drug delivery systems. The adsorption of a molecule on a clay surface, or formation of intercalates, gives rise to changes in the vibrational wavenumbers of the adsorbed molecule. In this study, interaction between the adsorbed milrinone molecules and montmorillonite was investigated by FT-IR and Raman spectrometry. The X-ray diffraction patterns of montmorillonite before and after treatment with milrinone showed a significant change in the $d(001)$ reflectance of clay. This reflection peak shifted to a lower angle due to the adsorption of milrinone onto the clay. The result indicated the intercalation of the milrinone molecules by increasing the interlayer spacing of the clay. Vibrational spectroscopic results indicated that intercalated milrinone interacted with clay by direct or indirect coordination (through water molecules) to exchangeable cations or the Lewis acidic centers.

Keywords: Clays; Milrinone; Montmorillonite; FTIR; Raman

1. INTRODUCTION

Milrinone (C₁₂H₉N₃O), a phosphodiesterase-3 inhibitor, is used for the short-term treatment of heart failure (Young & Ward 1988). It is a positive inotropic cardiotonic agent that acts as selective phosphodiesterase 3 inhibitor in cardiac and vascular smooth muscle. Milrinone acts as a vasodilator, by helping alleviate increased pressures (afterload) on the heart, thus improving its pumping action. It was approved by the FDA on December 31, 1987 (Shipley et al. 1996).

Montmorillonite, an expandable type of clay mineral, has a 2:1 layered structure consisting of one octahedral sheet and two tetrahedral sheets (T:O:T). The layers have a small net negative charge due to isomorphous substitution of ions in the framework. This negative charge is compensated by interlayer hydrated cations, which are known as exchangeable cations. The interlayer space can expand by the adsorption of a suitable solvent or organic molecules. It is well known that wide variety of organic molecules can intercalate between the interlayer regions of expandable clays and increase the interlayer region (Theng 1974; Schulze 2005).

Vibration frequencies of molecules are determined by infrared (IR) and Raman spectroscopy. Since molecular vibrational frequencies change depending on molecular interactions,

we investigate the interaction mechanism of milrinone with the clay framework.

2. MATERIAL METHOD

The natural montmorillonite sample was sourced from the Çankırı region of Anatolia, Turkey. Details on its chemical composition are provided in our previous study (Akyuz & Akyuz 2008). Milrinone (solid state) was reagent grade (Sigma Aldrich Chemicals) and used as received. Milrinone treated clay was prepared analogous method described (Akyuz & Akyuz 2008).

The FT-IR spectra of KBr discs were recorded on a Bruker Tensor 27 FT-IR spectrometer. Spectral data were collected over 4000–400 cm⁻¹ spectral range based on averaging 200 scans with a resolution of 1 cm⁻¹. The micro-Raman spectra of the powdered sample was recorded on a Jasco NRS-3100 μ -Raman spectrometer (1200 lines/mm grating and high sensitivity cooled CCD). A 532 nm line of the diode laser was used as the excitation wavelength. The XRD spectra of the starting montmorillonite and milrinone treated montmorillonite were recorded on a Rigaku D/Max 2200 powder X-ray diffractometer using Cu K α radiation.

Corresponding Author: S. Akyuz E-mail: s.akyuz@iku.edu.tr

Submitted: 21.03.2024 • Accepted: 25.04.2024 • Published Online: 05.06.2024



This article is licensed under a Creative Commons Attribution-NonCommercial 4.0 International License (CC BY-NC 4.0)

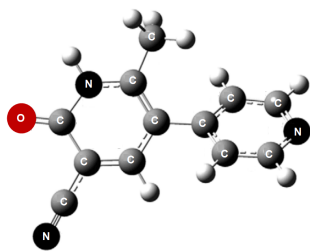


Figure 1. Molecular model of milrinone.

3. RESULTS AND DISCUSSION

The XRD pattern of starting montmorillonite indicated a basal spacing of 12.0 Å, which increased to 16.0 Å after treatment with milrinone. The increase in the basal spacing indicates formation of intercalates (Aguzzi et al. 2007; Borrego et al. 2018). The result clearly demonstrates the effective inclusion of drug in the interlayer spaces of the montmorillonite.

Clay minerals contain hydroxyl groups that can easily bond with water molecules through H-bonding interaction. These hydroxyl groups can also react with organic groups via H-bond bridges, either directly or indirectly through water bridges. These interactions are detected by the IR and Raman spectroscopy thanks to their vibrations in the infrared region.

Recently Esme (2017) calculated the optimized structure of milrinone using DFT/B3LYP/6-31G(d,p) level of theory. The molecular model of milrinone according to Esme (2017) is shown in Figure 1. Milrinone can interact through its ring nitrogen, cyano group nitrogen and/or carbonyl group oxygen. To determine the interaction mechanism of milrinone molecules adsorbed by montmorillonite, the vibrational wavenumbers of adsorbed milrinone were examined in comparison with the wavenumbers of milrinone in solid phase, taking into account the coordination effects via ring nitrogen, CN group nitrogen and > C=O group oxygen. The FTIR spectra of starting montmorillonite (untreated montmorillonite), milrinone treated montmorillonite and solid milrinone are given in Figure 2, comparatively. As seen in Figure 2, milrinone bands are clearly observed in the IR spectrum of milrinone treated montmorillonite, shifted compared to the solid phase. The result indicated that milrinone interacts with the clay, thereby becoming chemisorbed. Additionally, we observed slight alteration in the vibrational wavenumber of the asymmetric Si-O stretching mode of montmorillonite due to adsorption of milrinone (see upper frame of Figure 2). In previous studies it was shown that the Si-O stretching mode frequency was significantly affected by changes in swelling and orientation of the clay platelets and shifted to higher wavenumbers due to intercalated organic molecules (Katti & Kati 2006; Akyuz & Akyuz 2008). In our study the Si-O asymmetric stretching wavenumber observed at 1032 cm⁻¹ in the IR spectrum of montmorillonite was observed at 1041 cm⁻¹ in that of milrinone treated montmorillonite.

When a ligand coordinates through the oxygen of a carbonyl

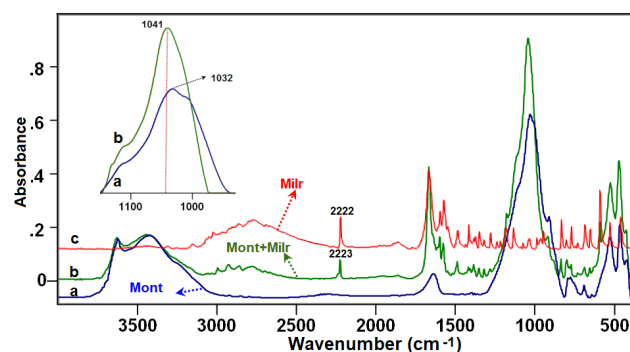


Figure 2. The FTIR spectra of montmorillonite (a), milrinone treated montmorillonite (b) and solid milrinone (c). Upper frame is the detailed 1100-1000 cm⁻¹ region of untreated (a) and milrinone treated (b) montmorillonite.

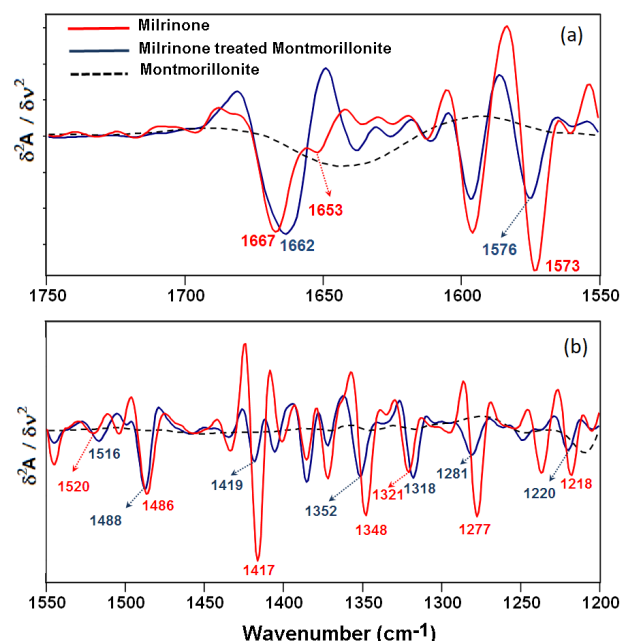


Figure 3. The 1700-1550 cm⁻¹ (a) and 1550-1200 cm⁻¹ (b) regions of the second derivative profiles of montmorillonite (dashed line), milrinone (red line) and milrinone treated montmorillonite (dark blue line).

group, a negative shift in the $\nu(\text{C}=\text{O})$ wavenumber of the coordinated molecule compared to the free ligand is expected. On the other hand, coordination through pyridine ring nitrogen of the ligand alters particularly the ring stretching vibrations. Dines et al. (2003) investigated the adsorption of 2-chloropyridine on oxide surfaces by vibrational spectroscopy and it was reported that the ring stretching vibrations around 1400-1600 cm⁻¹ increase in wavenumber upon hydrogen bond formation or adsorption at Lewis acid sites. In our previous study, the effect of the coordination of the pyridine ring nitrogen on the vibrational frequencies was calculated on the pyridinecarboxamide-Al(OH)₃ model compound (Akalin et al. 2005). It was found that in addition to the ring stretching vibrations around 1400-1600 cm⁻¹, the ring deformation modes around 1000 cm⁻¹, 800 cm⁻¹, and 400 cm⁻¹ were also the most sensitive modes to the coordination through pyridine ring nitrogen.

The IR absorption bands are relatively broad, due to over-

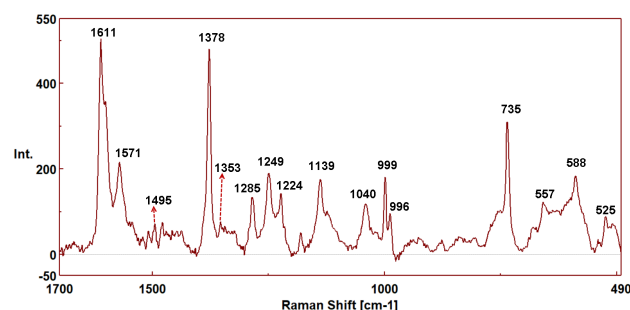
Table 1. Some vibrational wavenumbers (cm^{-1}) of solid milrinone and adsorbed milrinone onto montmorillonite.

Assignment	Milrinone	Milrinone	Adsorbed milrinone		
	This study	(Esme 2017)	This study		
	IR	IR	Ra	IR	Ra
$\nu\text{C=O}$	1667	1666	–	1662	–
νring	1595	1595	1606	1609	1611
νring	1573	1573	1568	1576	1571
$\delta\text{CH}(\text{ring})$	1486	1487	1485	1488	1495
νring	1373	1372	1375	1385	1378
δCH	1348	1349	1347	1352	1353
$\delta\text{CH}(\text{ring})$	1277	1279	1282	1281	1285
νring	1218	1219	1219	1220	1224
τring	989	988	960	–	999-996

*Obscured by the strong SiO stretching band (IR) of the clay. ν = bond stretching; δ = in plane angle bending; τ = torsion vibrations.

lapping several vibrational modes. In this study, we utilized the second derivative of the absorption spectrum as a resolution enhancement technique. This approach helps distinguish overlapping bands in the IR spectrum and clearly delineate the frequency alterations in milrinone due to its interaction with the clay framework. Figure 3 shows the second derivative profile of solid phase milrinone in comparison with that of adsorbed milrinone onto montmorillonite. The second derivative profile of the pure montmorillonite was also added to Figure 3 for comparison.

The C=O stretching mode of milrinone is observed at 1667 cm^{-1} in the solid phase, whereas it appears at 1662 cm^{-1} in the adsorbed phase (see Figure 3a). This shift indicates that the carbonyl oxygen of the adsorbed molecule engages in H-bonding interactions. On the other hand, ring stretching vibrations of milrinone determined at 1573 cm^{-1} and 1486 cm^{-1} in the second derivative profile of the IR absorption spectrum of milrinone were observed at 1576 cm^{-1} and 1488 cm^{-1} in that of milrinone treated montmorillonite (see Figure 3b). Similar shifts were also predicted upon formation of H-bonding through pyridine (Akyuz & Akyuz 2010) and pyrimidine (Des-texhe et al. 1994) ring nitrogen. The coordination sensitive vibrational modes of milrinone are tabulated in Table 1. The vibrational wavenumbers of adsorbed milrinone show coordination effects through both ring nitrogen and carbonyl oxygen. The results indicate that adsorbed milrinone molecules are coordinated through both the ring nitrogen and carbonyl oxygen lone pairs. Investigations of clay-organic complexes by Raman spectroscopy have the advantage that the strong SiO stretching and bending modes observed in the IR spectrum, were not observed in Raman spectrum, due to being weak scatter of silica. Thus, the Raman spectrum of a clay-organic complex, mainly involves organic molecule's vibrations. Figure 4 shows the Raman spectrum of milrinone treated montmorillonite. We compared adsorbed milrinone bands with those of solid milrinone given by Esme (2017) (see Table 1).

**Figure 4.** The Raman spectrum of milrinone treated montmorillonite.

4. CONCLUSION

In this study, the interaction of milrinone, a cardiotoxic drug used to reduce cardiac contractility, with montmorillonite was investigated using vibrational spectroscopy. The comparison of the XRD patterns of untreated- and milrinone treated montmorillonite indicated that as a result of the interaction of clay with the drug, diffraction pattern of montmorillonite shows significant changes. The reflection corresponding to $d(001)$ of montmorillonite shifted to lower angles after interaction with the drug. The interlayer spacing (basal spacing) of untreated clay was determined as 12.0 \AA . As a result of the adsorption of milrinone, the basal spacing of the milrinone-treated clay increased to 16.0 \AA . The result clearly indicates that the intercalation of milrinone molecules in the montmorillonite interlayer spacing. The comparison of the IR and Raman spectra of the adsorbed milrinone to those of solid milrinone elucidated the interaction mechanism of the milrinone with the clay framework. The results indicated that the adsorbed milrinone molecules on montmorillonite are coordinated through both nitrogen and oxygen ends to exchangeable cations directly or indirectly through water bridges.

Peer Review: Externally peer-reviewed.

Conflict of Interest: Author declared no conflict of interest.

Financial Disclosure: Author declared no financial support.




LIST OF AUTHOR ORCIDS

S. Akyuz <https://orcid.org/0000-0003-3313-6927>

REFERENCES

- Aguzzi C., Cerezo P., Viseras C., Caramella C., 2007, [Applied Clay Science](#), 36, 22
- Akalin E., Yilmaz A., Akyuz S., 2005, [Journal of Molecular Structure](#), 244, 881
- Akalin E., Akyuz S., Akyuz T., 2007, [Journal of Molecular Structure](#), 834, 477
- Akyuz S., Akyuz T., 2008, [Vibrational Spectroscopy](#), 48, 229
- Akyuz S., Akyuz T., 2010, [Vibrational Spectroscopy](#), 53, 136
- Borrego-Sánchez A., Carazo E., Aguzzi C., Viseras C., Sainz-Díaz C. I., 2018, [Applied Clay Science](#), 160, 173
- Destexhe A., Smets J., Adamowicz L., Maes G., 1994, [Journal of Physical Chemistry](#), 98, 1506
- Dines T. J., MacGregor L. D., Rochester C. H., 2003, [Spectrochimica Acta A](#), 59, 3205
- Esme A., 2017, [Indian Journal of Pure & Applied Physics](#), 55, 478
- Katti K., Katti D., 2006, [Langmuir](#), 22, 532
- Massaro M., Colletti C. G., Lazzara G., Riela S., 2018, [Journal of Functional Biomaterials](#), 9, 58
- Rocha M. C., Galdino T., Trigueiro P., Honorio L.M.C. et al., 2022, [Pharmaceutics](#), 14, 796
- Schulze D. G., 2005, [Clay Minerals \(Ed: Hillel, D.\) in Encyclopedia of Soils in the Environment](#), Elsevier, 246
- Shipley J. B., Tolman D., Hastillo A., Hess M. L., 1996, [The American Journal of the Medical Sciences](#), 311, 286
- Theng B. K. G., 1974, [The Chemistry of Clay Organic Reactions](#), Hilger, London, 1974
- Young R. A., Ward A., 1988, [Drugs](#), 36, 158

Fundamentals of Stars: A Critical Look at Mass-Luminosity Relations and Beyond

Z. Eker^{1*} , F. Soyduğan^{2,3} , and S. Bilir⁴ 

¹Akdeniz University, Faculty of Sciences, Department of Space Sciences and Technologies, 07058, Antalya, Türkiye

²Çanakkale Onsekiz Mart University, Faculty of Sciences, Department of Physics, 17100, Çanakkale, Türkiye

³Çanakkale Onsekiz Mart University, Astrophysics Research Center and Ulupınar Observatory, 17100, Çanakkale, Türkiye

⁴İstanbul University, Faculty of Science, Department of Astronomy and Space Sciences, 34119, Beyazıt, İstanbul, Türkiye

ABSTRACT

Developments on various relations among stellar variables such as the main sequence empirical mass-luminosity (MLR), mass-radius (MRR) and mass-effective temperature (MTR) relations were reviewed. Conceptual changes in their understanding and usages were discussed. After its discovery, MLR was treated as one of the fundamental secrets of the cosmos. Differences between fundamental laws and statistical relations were used to understand long-term developments of MLR, MRR and MTR. Developments show a break point, initiated by Andersen (1991), in the line of progress. Before the break when reliable data were limited, MLR and MRR were calibrated using M , L , and R of binary components of all kinds visual, spectroscopic, and eclipsing for two purposes: *i*) to obtain mean mass, mean luminosity, and mean radius, *ii*) to estimate M and R of single stars. By the time of the break, the number of solutions from detached double-lined eclipsing binaries (DDEB) giving accurate M and R within a few percent levels are increased. Parameters from very close, semi-detached, and contact binaries were excluded for refinement, however, MLR and MRR diagrams were found insufficient to derive MLR and MRR functions because the dispersions are not only due to random observational errors but also due to chemical composition and age differences. Then, a new trend was adopted by replacing classical MLR and MRR with empirical M and R predicting relations. Thus, the purpose one was suppressed also because the new trend found a fruitful application in determining M and R of exoplanet hosting single stars.

Keywords: Stars: fundamental parameters; Stars: luminosity and mass functions; Galaxies: luminosity function and mass functions; Cosmology: miscellaneous

1. INTRODUCTION

Accuracy and precision of observational parameters of stars are crucial not only for improving stellar structure and evolution theories but also for fundamental astrophysics, Galactic and extragalactic studies, and ultimately even for cosmological models because stars and galaxies are the primary building blocks of the universe. Fundamental and statistical relations are essential for understanding physical events occurring in various parts of the universe. The fundamental relations are the relations like Stefan-Boltzmann law ($L = 4\pi R^2 \sigma T_{\text{eff}}^4$) which are characterised by at least two properties; *i*) how various properties of stars are related, e.g. how the luminosity of a star is related to its radius and effective temperature; *ii*) validity is not limited by certain conditions, that is, it applies to all stars and radiating surfaces as long as the source of radiation is thermal. The statistical relations, on the other hand, may not work in all possible cases; appropriate statistical conditions are required.

A good example is the kinetic temperature. A temperature is a physical quantity that is measured in the macroworld but does not exist in the microworld. This is because temperature is a statistically defined quantity implying an average kinetic energy per particle in a substance, which could be a solid, liquid, or gas. The definition of kinetic temperature indicates that a single particle or insignificant number of particles cannot be associated with any temperature. For example, when we talk about air temperature, it indicates the average kinetic energy per air particle, which can be written as:

$$\frac{1}{2} m \langle v^2 \rangle = \frac{3}{2} kT \quad (1)$$

where m and $\langle v^2 \rangle$ are the mean mass and root-mean-square (rms) speed of particles. They are not physical quantities but average values. Increasing the speed of the substance itself by moving it faster, e.g., putting it on a quick aeroplane, does

Corresponding Author: Z. Eker E-mail: eker@akdeniz.edu.tr

Submitted: 17.11.2023 • **Revision Requested:** 28.01.2024 • **Last Revision Received:** 07.02.2024 • **Accepted:** 09.02.2024 • **Published Online:** 11.06.2024



This article is licensed under a Creative Commons Attribution-NonCommercial 4.0 International License (CC BY-NC 4.0)

not change its temperature. Therefore, equation (1) cannot be written for a randomly chosen particle (or a few particles), i.e., the right-hand side does not exist except for a group of particles satisfying the implied statistic.

Similarly, the mass–luminosity relation (MLR) in the form ($L \propto M^\alpha$), which is defined so far for main-sequence stars, is a statistical relation similar to equation (1), which indicates how main-sequence luminosities are related to main-sequence masses. Because it is not valid for non-main sequence stars, depending upon expected accuracy, it may also not be valid for an individual star. Therefore, it is the relation devised for estimating a typical mass from a typical luminosity, or vice versa.

Consequently, inter-related mass-luminosity (MLR), mass-radius (MRR), and mass-effective temperature relations (MTR) of Eker et al. (2018) are all statistical relations, which should not be treated like fundamental relations. While the bolometric correction – effective temperature relation (BC- T_{eff}) of Flower (1996); BC- T_{eff} and BC-mass relations of Eker et al. (2020, 2021b); Bakış & Eker (2022); Eker & Bakış (2023) are all statistical relations that should not be confused by fundamental relations; otherwise, unexpected results or upsetting errors in the computed quantities become unavoidable.

One cannot say “statistical relations are less valuable than fundamental relations”. On the contrary, a statistical relation could be more valuable; even more practical, or easier to use, e.g., calculating the total energy of a gas as the mean energy per particle multiplied by the number of particles in the gas. Otherwise, the probability of each particle having a certain kinetic energy and the number of particles having this energy are required before integrating them over all possible kinetic energies. Similarly, using an MLR is more practical for determining the masses and luminosity of galaxies, which are the key parameters for determining dark matter in galaxies. Otherwise, to obtain the total mass and total luminosity of the galaxy in question, one would have to add up the individual masses and luminosities of the stars in the galaxy, which is impractical.

Moreover, there could be various astrophysical studies demanding MLR, MRR, and MTR in addition to stellar astrophysics. Live examples such as cometary research (Wysoczańska et al. 2020a,b), Oort clouds (Baxter et al. 2018), heliophysics and planetary habitability (Schrijver et al. 2019), exoplanet investigations (Berger et al. 2020; Arora & Hasegawa 2021; Burt et al. 2021; Caballero et al. 2022; Dattilo et al. 2023), planetary nebula (Munday et al. 2020; Aller et al. 2020), open clusters (Ilin et al. 2021; Akbulut et al. 2021; Yontan et al. 2021, 2023; Yontan 2023), dark matter searches (Garani & Palomares-Ruiz 2022; Peled & Volansky 2022) and quasars (Albert et al. 2021), neutron stars (Yuan et al. 2022), black holes (Gomel et al. 2021a,b), general relativity (Lalremruati & Kalita 2021), gravitational lensing (Ramesh et al. 2022; Pietroni & Bozza 2022) and even search for extra-terrestrial intelligence (SETI, Kerins 2021; Kerins et al. 2023), which all used at least

one of the statistical relations MLR, MRR and MTR of Eker et al. (2018).

Apparently, differentiation between fundamental and statistical relations is important from an astrophysical perspective. Recognizing statistical relations is even more important; otherwise, using them as fundamental relations would be misleading. Unfortunately, some authors such Malkov (2003, 2007), Henry (2004) and Gafeira et al. (2012) including Eker et al. (2015) did not hesitate to call MLR “fundamental law”, “sufficiently fundamental to be applicable to many areas of astronomy”, “one of the most famous empirical law” and “one of the fundamental secrets of the cosmos”. On the contrary, Andersen (1991) and Torres et al. (2010) preferred not to define a MLR and preferred displaying the $\log M - \log L$ diagram without a function (MLR) fitting to the data because the scatter on the diagram is not due to observational random errors but most likely due to abundance and evolutionary effects. Andersen (1991) claims “...departures from a unique relation is real”. If there is no unique function to represent the data on the diagram, why bother to defining one?

Therefore, this review article is dedicated to investigating the evolution of the statistical functions MLR, MRR, and MTR, starting from their discovery until today, and attempting to explain why such quarrels occurred and whether it is possible to resolve conflicts by identifying the nature of the relation. Moreover, the presentation of their conceptual advances and realising whether they were perceived as fundamental laws or statistical relations will benefit to the astronomical community. Developing such a conscious analysis would result in a better understanding of their previous usages and future studies.

2. OVERVIEW

Calibrations of MLR, MRR, and MTR require predetermined accurate stellar parameters such as mass (M), luminosity (L), radius (R), and effective temperature (T_{eff}). The most critical parameter among them is L because it is not an observable quantity; that is, neither a telescope nor a detector to observe the total radiation of a star at all frequencies (Bakış & Eker 2022; Eker & Bakış 2023). Fortunately, there are only one direct and two indirect methods to calculate L of a star (Eker et al. 2021c). The first method is a direct one because it uses independently determined observational R and T_{eff} of a star to calculate its L directly from its radiating surface area ($4\pi R^2$) and bolometric flux (σT_{eff}^4), which is commonly known as the Stefan-Boltzmann law ($L = 4\pi R^2 \sigma T_{\text{eff}}^4$). The other two methods are indirect because the first method, which provides L of a star from its M , requires a predetermined classical MLR in the form of $L \propto M^\alpha$, while the second method, which supplies L of the star from its apparent brightness and distance requires a pre-determined BC- T_{eff} relation. Unfortunately, the indirect methods are useless without their predetermined relations, and thus, one has no other choice but to use the Stefan-Boltzmann

law to produce the earliest sample of L values for the first calibration of MLR, MRR, and MTR.

Assuming that the sample L values are ready, the next most critical parameter is stellar M to establish not only MLR but also MRR and MTR because sequentially required R and T_{eff} should have been already used in computing L of the sample stars. However, like L of a star, M of a star is also not observable. This fact makes the parameter M even more critical because only the masses of binaries (or multiple systems) could be calculated using Kepler's Third Law from the observed orbital semi-major axis and the orbital period, which could be deduced from the observed orbits of visual binaries (or multiple systems) or from the radial velocity curves of double-lined eclipsing spectroscopic binaries. Stellar spectra do not provide orbital inclinations; thus, spectroscopic binaries without eclipses cannot provide component masses unless orbital inclinations are available independently.

Eclipsing binaries are ideal objects for collecting observed radii of stars, whereas the single stars are null, except the ones close in distance and large enough where interferometry could be useful. Although binarity adds complications to the estimation of component effective temperatures, the eclipsing binaries are still advantageous for revealing the most accurate effective temperatures and temperature ratios from the depths of minima if the effective temperature for one of the components is estimated correctly.

Visual binaries (multiple systems too) and double-lined eclipsing binary systems are the only objects provided M from Kepler's third law, with R from eclipses. On the other hand, there is almost no other way to obtain accurate masses and radii of single stars except seismic analysis where mass and radii data for solar-like pulsating stars (e.g. [Gaulme et al. 2016](#); [Bellinger et al. 2019](#)) are obtained. Considering some basic information and data knowledge about this research topic, we must now start reviewing the statistical relations starting from the most prominent one: MLR.

2.1. Revisiting MLR

The famous stellar mass-luminosity relation (MLR) was discovered empirically in the middle of the first half of the 20th century by [Hertzsprung \(1923\)](#) and [Russell et al. \(1923\)](#) independently using masses and absolute brightness of a very limited number of visual binaries. Eclipsing binaries were included later in the statistics. In his MLR, [Eddington \(1926\)](#) was able to use 13 eclipsing binaries together with 29 visual binaries and five Cepheids, which were available to him at that time, while [McLaughlin \(1927\)](#) increased the number of eclipsing systems to 41 in his plots.

By the time of the mass-luminosity relation was discovered, there were only three kinds of brightness measurements: 1) Visual magnitudes (m_v) from the brightness observations of stars by eye. 2) Photographic magnitudes (m_p) measured from the sizes of star images on photographic plates. 3) Bolometric

magnitudes (m_b) as heat measurements, which could be coming from galvanometric, bolometric, or radiometric observations of stars. It was thought that bolometric magnitudes coming from the heat measurements of stars represent the total radiation output (luminosity) best. Therefore, assuming that stars are hot spheres of gases, [Eddington \(1926\)](#) formulated a theoretical relation between the mass and absolute bolometric magnitude of a star. Furthermore, he continued to confirm his theoretical relation using the existing data [Eddington \(1926, page 154\)](#) from binaries. [Gabovits \(1938\)](#) agreed [Eddington \(1926\)](#) after twelve years by re-examining the mass- M_{Bol} data again and declared "We conclude that, as revealed by our selected first-class data, the stars (chiefly of the main-sequence) probably follow a strict mass-luminosity law". On the other hand, having larger data sets including visual binaries, spectroscopic binaries, Hyades and Trumpler stars, and white dwarfs, [Kuiper \(1938\)](#) was rather suspicious of accepting the mass-luminosity relation as a law because he commented "It is doubtful whether this mean relation has any physical significance" after discussing it on a $\log M - M_{\text{Bol}}$ diagram.

MLR has been updated and revised many times until a major break occurred at the very beginning of the last decade of the 20th century on the issue of whether it is a statistical relation or a fundamental law. Looking at the developments before this break would be useful to understand it better. [Petrie \(1950a,b\)](#) used 93 spectroscopic binary systems, [Strand & Hall \(1954\)](#) studied 23 visual binaries, [Eggen \(1956\)](#) investigated 34 visual binaries, [McCluskey & Kondo \(1972\)](#) considered 40 visual binaries and 35 eclipsing systems, [Cester et al. \(1983\)](#) gathered 45 visual and 40 spectroscopic binaries, [Griffiths et al. \(1988\)](#) analysed 72 detached main-sequence binaries, 25 detached OB, 6 resolved binaries and 23 visual binaries when revising the MLR relations. [Demircan & Kahraman \(1991\)](#) preferred to study masses and luminosities of 70 eclipsing binaries (140 stars) only, including the main sequence components of detached and semi-detached binaries as well as the components of OB-type contact and near contact binaries. [Karetnikov \(1991\)](#) used 303 eclipsing systems of different types. At this point, we must keep in mind that the observational data was very limited, therefore, the authors combined different kinds of binaries, whether they are eclipsing or not, without differentiating between detached, semi-detached, and contact systems. This was done to increase the statistical reliability of MLRs calibrated.

Those early generation relations, including the very earliest ones, were demonstrated mass-absolute magnitude diagrams mostly, some with the best fitting function, and some without a fitting curve. Considering the classical form $L \propto M^\alpha$ of MLR, first [Eggen \(1956\)](#) intended to define the power of mass (α) so he expressed $L = \mu^{3.1}$, where μ is the total mass of a double-star system defined as $\mu = a^3/P^2\pi^3$ from the Kepler's Harmonic Law. Then, [McCluskey & Kondo \(1972\)](#) preferred to use a relation in the form $M \propto L^\beta$, where M and L are the masses and luminosities of the components while α and β are the constants to be determined by the data on various mass-

absolute bolometric magnitude diagrams. Accordingly, Cester et al. (1983); Griffiths et al. (1988) and Demircan & Kahraman (1991) preferred to study MLR on a mass-luminosity diagram for defining unknown constants on the classical form ($L \propto M^\alpha$) of MLR either by fitting a curve to all data or dividing the mass range into two regions as low- and high-mass stars, or three regions as the high, intermediate or Solar, and low-mass stars, in order to determine the inclinations (power of M) and zero point constants of the linear MLRs on the $\log M - \log L$ diagram.

2.1.1. Is MLR a Fundamental Relation?

The major break on the concept and splitting practises on the purpose of calibrating an MLR was triggered by Andersen (1991) who collected 45 detached double-lined eclipsing binary (DDEB) systems (90 stars) having both masses and radii accurate within 2%, which were the most accurate stellar data of the time. Selecting only DDEB stars was not intended to reject the reliability of the other sources for determining masses and radii; only because M and R from DDEB were considered the most reliable.

Andersen (1991) rejected calibrating any form of MLR function to fit data on the $\log M - \log L$ diagram. The diagram displayed by him is without a fitting curve (MLR) because the scatter from the curve is certainly not only due to random observational errors but also due to abundance and evolutionary effects. He exclaimed: “At first glance, the mass-luminosity diagram shows a tight, well-defined mean relation. Closer inspection, taking individual uncertainties into account, reveals that departures from a unique relation are real”. Then, if there is no unique curve expressible by a function to represent data, why bother drawing one?

In very early times, especially after its discovery, MLR was claimed to be one of the most prominent empirical laws of nature by Eddington (1926) and Gabovits (1938) and commonly used by researchers either reckoning L of a star from its M or estimating M of a star from its L , at least until the middle of the 20th century, and perhaps until Andersen (1991). This practice was extremely useful for single stars because there was no other observational way to directly access their masses, but the absolute bolometric magnitudes of the ones with known parallaxes were rather easy to obtain using a proper bolometric correction (BC), and then their masses were estimated from a predetermined bolometric magnitude-mass relation. The method was even helpful in double-checking trigonometric parallaxes of single stars and even eclipsing binaries with light curve solutions giving R and T_{eff} of the components, thus L values are compatible by the Stefan-Boltzmann law. Those very early times were a period in astrophysics when nuclear reactions were not fully established and understood correctly. The discovery of nuclear reactions in the cores of stars is attributed to Sir Arthur Eddington (Bahcall 2000) a few years before the discovery of MLR by Hertzsprung (1923) and Russell et al. (1923).

Astronomers waited until 1932 for the discovery of neutrons

(Chadwick 1933) to study and fully understand hydrogen fusion as a main source of stellar energy. Only after the CNO cycle was established by Hans Bethe and Von Weizsacher (Clayton 1968), and only a year later, the p-p chain reactions were suggested by Bethe (1939), there were the solutions of stellar structure equations with the nuclear energy, which placed our theoretical understanding of the evolution of stars with evolutionary tracks on a solid ground (Clayton 1968). The empirically discovered MLR was confirmed later theoretically in the sense that mass (M) is the prime parameter that determines the internal structure, size (R), and luminosity (L) of a star not only for the time span of the main sequence but also throughout the star's lifetime until its death, where its initial chemical composition can cause little variation. Therefore, the scatter on a $\log M - \log L$ diagram for field main-sequence stars is not only due to observational errors but also due to various ages and chemical compositions.

Additionally, at least until the middle of the 20th century, maybe until about the middle of its second half, but certainly not until Andersen (1991), the observational accuracy was not high enough to differentiate theoretical (true) L and M of stars, which are marked on a Hertzsprung Russell (H-R) diagram to form evolutionary tracks. As long as the observational accuracies of L and M are much lower than the uncertainty of error bars covering the full thickness of the main sequence, astronomers did not suspect inconsistency between the predicted and observed quantities using an MLR. It was normal for them to be satisfied, as in the case of fundamental law.

By the time of Andersen (1991), who collected the most accurate M and L data from DDEB, there were sufficiently accurate masses and luminosities; thus, one can deduce that the scatter on the $\log M - \log L$ diagram is not only due to observational errors of M and L but also due to abundance and evolutionary effects. Andersen (1991) felt something was not right, that is, there must be a problem in treating classical MLR in the form $L \propto M^\alpha$ as a fundamental relation. Andersen thought that such a fundamental relation must not only fit the data uniquely but also must contain the other parameters involving the chemical composition and evolution.

Being influenced by the common usage, a kind of paradigm not easy to be free off, Andersen (1991) was expecting, like the others before him, to obtain the mass of a single star from its luminosity within acceptable accuracy [ideally $\pm 5\%$ see Andersen (1991) page 93]. However, with a mean MLR in the form $L \propto M^\alpha$ for the main-sequence stars, this was not possible anymore due to improved observational techniques with higher accuracy in both L and M values available to him. Nevertheless, he succeeded in this aim about two decades later by replacing $\log L$ with a function including observational parameters T_{eff} , surface gravity ($\log g$), and relative iron abundance $[\text{Fe}/\text{H}]$ to incorporate evolution (age) and chemical composition as

$$\log M = a_1 + a_2 X + a_3 X^2 + a_4 X^3 + a_5 (\log g)^2 + a_6 (\log g)^3 + a_7 [\text{Fe}/\text{H}], \quad (2)$$

in a new review paper, in which [Torres et al. \(2010\)](#) was the leading author; where $X \equiv \log T_{\text{eff}} - 4.1$ as a parameter that contains the most effective variable, T_{eff} , related to the luminosity with its fourth power in the Stefan-Boltzmann law, and a 's which are the calibrated coefficients $a_1 = 1.5689 \pm 0.058$, $a_2 = 1.3787 \pm 0.029$, $a_3 = 0.4243 \pm 0.029$, $a_4 = 1.139 \pm 0.240$, $a_5 = -0.1425 \pm 0.011$, $a_6 = 0.01969 \pm 0.0019$, and $a_7 = 0.1010 \pm 0.058$. This is a function providing 6.4% accuracy for main-sequence and evolved stars above $0.6M_{\odot}$. It is obvious that such a function cannot be drawn on a $\log M - \log L$ diagrams but provides stellar M as the classical MLR but is much more accurate not only for main-sequence stars but also for giants and sub-giants. Thus, both [Andersen \(1991\)](#) and [Torres et al. \(2010\)](#) presented their $\log M - \log L$ diagrams without a fitting function.

Incorrect diagnoses are natural to be continued by incorrect treatments. First, classical MLR in the form of $L \propto M^{\alpha}$ is a statistical relation devised for estimating a typical mass from a typical luminosity, or vice versa, and not for estimating M or R of a single star, even if it was once used to estimate M of a star from its L . Therefore, It is not right to diagnose the classical MLR as one of the fundamental relations to calculate the mass of a star from its luminosity. It is not right to look for a relation that gives the mass of a star from other stellar observational parameters for replacing MLR. It is not right to call this relation MLR if it provides M of a star from the other parameters even if L is included in the right-hand side of the equal sign, except if the right-hand side contains only L as a variable. It is not right to claim that there is no uniquely fitting function to the data on $\log M - \log L$ the diagram despite a tight, mean relation between M and L as if the least squares method would fail to produce one.

Nevertheless, [Andersen \(1991\)](#)'s exclamation had a noticeable consequence in stellar astrophysics. It appears as if a main cause of deviation in understanding, definition, and usage of newly defined MLR functions from the main path, which was continued by [Ibanoglu et al. \(2006\)](#) and [Eker et al. \(2015, 2018\)](#) where statistical relation between masses and luminosities of main-sequence stars was kept in the form $L \propto M^{\alpha}$.

2.1.2. Mass Predicting Relations of the Deviated Path

[Andersen \(1991\)](#)'s objection was very effective in the literature that some authors ([Malkov 2003, 2007](#); [Torres et al. 2010](#)) also presented their empirical mass-luminosity diagrams without a curve fitting to the data. [Gafeira et al. \(2012\)](#) just gave mass-luminosity relations for main sequence FGK stars without displaying them on a mass-luminosity diagram. [Fernandes et al. \(2021\)](#), which compared results to [Torres et al. \(2010\)](#), could be considered as a new improved version of [Gafeira et al. \(2012\)](#). [Fernandes et al. \(2021\)](#), thus, did not display mass-luminosity relations on the mass-luminosity diagram.

Various kinds of mass-predicting empirical relations were calibrated, and most of them were erroneously called MLR.

[Gorda & Svechnikov \(1998\)](#) choose the form $M_{\text{Bol}} = a + b \log M$, where M_{Bol} is the absolute bolometric magnitude and M is the mass. [Henry & McCarthy \(1993\)](#) preferred $\log M = aM_{\xi} + b$ for infrared colours, where M_{ξ} indicates absolute magnitudes at the J , H , and K bands, and $\log M = aM_V^2 + bM_V + c$ for the V band to express various MLR with unknown coefficients a , b , and c to be determined by the data on various diagrams. The former relation in the form $M_{\text{Bol}} = a + b \log M$ could be justified to be named mass-luminosity relation since M_{Bol} of a star is directly related to its luminosity, but a relation in the form $\log M = aM_{\xi} + b$, is definitely not a mass-luminosity relation. Such relations should be called mass-absolute brightness relations to avoid confusion.

The style of expressing V -band mass-absolute brightness relation as second-degree polynomials covering masses $0.6 M_{\odot}$ to $22.89 M_{\odot}$ is continued by [Xia & Fu \(2010\)](#) who calibrated it within two regions: one for $M_V < 1.05$ mag ($2.31 < M/M_{\odot} < 22.89$) and other for $M_V > 1.05$ mag ($0.60 < M/M_{\odot} < 2.31$) using the dynamical masses and V -band absolute magnitudes of 203 main-sequence stars, but the relation is still called MLR. The accuracy of the predicted masses is estimated to be within 5%. The style of displaying mass (M/M_{\odot}) versus absolute magnitude data in which the absolute magnitudes are in the visual and the K -bands is continued by [Benedict et al. \(2016\)](#) for the low end of the main sequence ($M < 0.6M_{\odot}$) but in different functional forms predicting masses as accurate as $\pm 0.035M_{\odot}$ in the region $M = 0.2M_{\odot}$. Similarly, both direct (absolute magnitude for a given mass) and inverse (mass for a given absolute magnitude) relations of [Benedict et al. \(2016\)](#) are better known as empirical mass-brightness relations rather than mass-luminosity relations. The empirical data of [Benedict et al. \(2016\)](#) are also compared to the theoretical mass-absolute brightness curves of age 1 Gyr of [Baraffe et al. \(2015\)](#) and [Dotter \(2016\)](#). K -band data fit better than the V -band data.

Mass-Absolute visual magnitude [$M_V - (\log m)$], mass-luminosity [$\log L - (\log m)$], mass-temperature [$\log T_{\text{eff}} - (\log m)$], and mass-radius [$\log R - (\log m)$] relations and corresponding inverse relations are calibrated for the intermediate-mass stars in the mass range $1.4 < M/M_{\odot} < 12$ by [Malkov \(2007\)](#) in forms of polynomials with empirically determined coefficients from the fundamental parameters of stars collected from DDEB and visual binaries. Similar empirical relations were studied later from a wider perspective by [Moya et al. \(2018\)](#) using a set of observational parameters M , R , T_{eff} , g (surface gravity), ρ (mass density), and $[\text{Fe}/\text{H}]$ of 934 stars of eclipsing binaries and single stars observed by asteroseismology and interferometry where two thirds of the stars are on the main sequence. A total of 576 linear combinations of T_{eff} , L , g , ρ , and $[\text{Fe}/\text{H}]$ (and logarithms) were used as independent variables to estimate M and R , but [Moya et al. \(2018\)](#) presented only 38 of them with regression statistics $\text{adj-}R^2$ higher than 0.85. Accuracy better than 10% was achieved in almost all cases of 38 equations. The term ‘‘empirical relations’’ used by [Moya et al. \(2018\)](#), and the names of relations given by [Malkov \(2007\)](#)

are proper and consistent in comparison to the names used for the mass predicting relations in the previous paragraph.

Using $\log L/L_\odot$, $[\text{Fe}/\text{H}]$, and star age/ age_\odot as free variables, [Gafeira et al. \(2012\)](#) suggested three different equations so that one can choose one according to the availability of data. The simplest is first, which is a third-degree polynomial without a constant term, having X , where $X \equiv \log L/L_\odot$. The second equation adds $[\text{Fe}/\text{H}]$ as a new variable in another third-degree polynomial into the equation in addition to the first. The third equation combines three third-degree polynomials, where the third uses the relative age ($\text{age}/\text{age}_\odot$) of the star as a variable. With all the parameters, the third relation looks like equation (2) given above by [Torres et al. \(2010\)](#). That is, the part $a_1 + a_2X + a_3X^2 + a_4X^3$ is replaced by $0.0219(\pm 0.023) \log L/L_\odot + 0.063(\pm 0.060)(\log L/L_\odot)^2 - 0.119(\pm 0.112)(\log L/L_\odot)^3$ while the part $a_7[\text{Fe}/\text{H}]$ is replaced by $+0.079(\pm 0.031)[\text{Fe}/\text{H}] - 0.122(\pm 0.119)[\text{Fe}/\text{H}]^2 - 0.145(\pm 0.234)[\text{Fe}/\text{H}]^3$ at last the part $+a_5(\log g)^2 + a_6(\log g)^3$ is replaced by $+0.144(\pm 0.062)(\text{age}/\text{age}_\odot) - 0.224(\pm 0.104)(\text{age}/\text{age}_\odot)^2 - 0.076(\pm 0.045)(\text{age}/\text{age}_\odot)^3$. Adding age and metallicity improved the mass estimation (15% to 5%) for FGK stars ([Gafeira et al. 2012](#)). However, only the first equation could be called MLR, but not the other two, which are better to be called mass-luminosity-metallicity relation and mass-luminosity-metallicity-age equation, respectively. Nevertheless, [Fernandes et al. \(2021\)](#) corrected this by changing the name “the mass and radius-luminosity-metallicity-age relations” in the new version, which was calibrated by 56 stars with metallicity and mass in the ranges $-0.34 < [\text{Fe}/\text{H}] (\text{dex}) < 0.27$ and $0.66 < M/M_\odot < 1.8$ from the DEBCat catalogue¹. The estimated accuracy in the new version is 3.5% and 5.9% in predicting M and R of single stars, respectively. [Serenelli et al. \(2021\)](#) commented: “[Gafeira et al. \(2012\)](#) provided three relations for the stellar mass, but only two of them can be easily applied”.

[Serenelli et al. \(2021\)](#) studied mass determination methods from a wider perspective, including all existing techniques older and newer; involving spectroscopy and/or photometry; theoretical or observational and at last summarised them in a figure (Figure 16 of [Serenelli et al. 2021](#)) where one can see their applicable ranges of stellar mass as well as the accuracy and precision of the predicted masses. Despite deceiving examples as summarised in the three paragraphs above, [Moya et al. \(2018\)](#) were careful not to use the word “MLR” for naming their “empirical relations”, which are established to estimate M and R only. While [Fernandes et al. \(2021\)](#) constantly called their similar functions MLR and claimed: “for single nearby Solar-type stars, the luminosity can be obtained observationally, but not the mass”, opposing the fact that the luminosity of a star is actually not an observable parameter because there is no telescope/detector to observe at all wavelengths. Call-

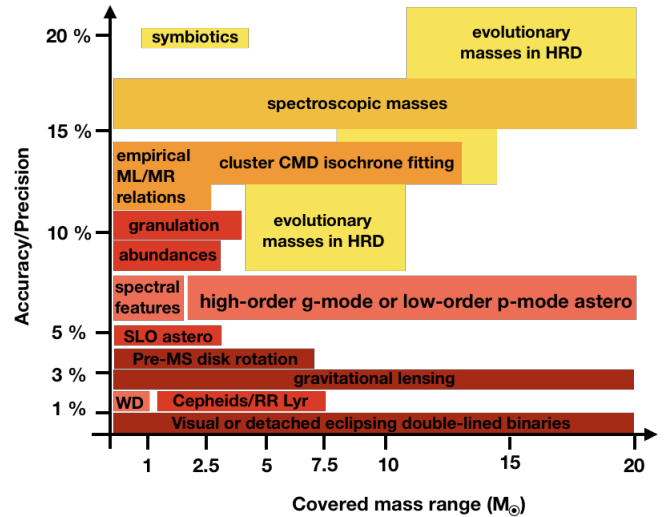


Figure 1. Mass ladder summarising the capacity of various methods to obtain stellar masses (credit to [Serenelli et al. 2021](#)).

ing these M or R predicting relations ML/MR would be a main source of confusion among readers. For example, “empirical ML/MR relations” marked in Figure 16 of [Serenelli et al. \(2021\)](#) at an accuracy/precision in between 10% and 15% for stars $M < 2.5M_\odot$, wherein the caption “ML/MR for mass-luminosity and mass-radius relations” is written clearly, could be confusing to a careful reader.

This is because: Is it possible for [Serenelli et al. \(2021\)](#) using ML/MR to indicate both the empirical relations of [Moya et al. \(2018\)](#) and the classical mass-luminosity/mass-radius relations (MLR/MRR) of [Eker et al. \(2018\)](#)? According to Figure 1 (Figure 16 of [Serenelli et al. 2021](#)) the answer would be “yes” because the relations of [Moya et al. \(2018\)](#) are not marked as “empirical relations” on the figure, and it is not possible to forget them because they cover one of the very important sections of the review (Section 4.4), where the M predicting relations of other authors are summarised and compared to their counterparts in [Moya et al. \(2018\)](#) (see Table 1). However, [Serenelli et al. \(2021\)](#) declared “All the relations except two (those with the largest number of dimensions) have precision better than 5%”. If the answer is “yes”, then, another problem arises: “If ML/MR in Figure 1 implies both classical MLR/MRR and the new M/R predicting relations, why the precision for the ML/MR is marked to be from 10% to 15% while M/R predicting relations are said to have precisions better than 5%?”.

It is possible that ML/MR in Figure 1 were actually marked from 3% to 15%, but this region on the figure is shadowed by various other methods of predicting stellar mass. Then another conceptual problem comes out: Only similar quantities can be compared. It is not right to compare the accuracy/precision of the empirical relations of [Moya et al. \(2018\)](#), which are solely devised for predicting masses of single stars, to the accuracy/precision of the classical MLR, which is primarily devised to establish as a statistical relation between typical masses and luminosities of main-sequence stars. It is inconsistent and

¹ <https://www.astro.keele.ac.uk/jkt/debcats/>

Table 1. Mass predicting empirical relations of other authors are compared with their counterparts in Moya et al. (2018) (credit to Serenelli et al. 2021).

Ref.	Relation	Acc/Prec	Ref.	Corresponding relation	Acc/Prec
T10	$M = f(X, X^2, X^3, \log^2 g, \log^3 g, [\text{Fe}/\text{H}])$	7.4/52.9	M18	$M = f(T_{\text{eff}}, \log g, [\text{Fe}/\text{H}])$	7.5/3.4
G12	$M = f(\log L, \log^2 L, \log^3 L)$	14.0/0.6	M18	$\log M = f(\log L)$	10.1/0.1
G12	$M = f(\log L, \log^2 L, \log^3 L, [\text{Fe}/\text{H}], [\text{Fe}/\text{H}]^2, [\text{Fe}/\text{H}]^3)$	8.9/0.8	M18	$\log M = f(\log L, [\text{Fe}/\text{H}])$	9.9/0.9
M07	$M = f(\log L, \log^2 L)$	11.2/—	M18	$\log M = f(\log L)$	10.08/0.13
E18	$\log L = f(\log M)$	33.3/6.9	M18	$\log L = f(\log M)$	31.9/0.6

References: T10 (Torres et al. 2010), G12 (Gafeira et al. 2012), M07 (Malkov 2007), E18 (Eker et al. 2018), M18 (Moya et al. 2018).

meaningless to compare E18 with M18 in Table 9 of Serenelli et al. (2021) (see Table 1). Similarly, it is scientifically inconsistent if empirical ML/MR in Figure 1 indicates classical MLR/MRR as well, rather than the empirical relations of Moya et al. (2018). This is because Eker et al. (2018) declared: “(classical) MRR and MTR functions, as well as the MLR functions, are needed by the astronomical community for practical purposes. These include the need to be able to estimate a typical luminosity, radius, and T_{eff} for main-sequence stars of a given mass”. Which is definitely different from the purpose of predicting M or R of single stars all over the H-R diagram?

After having M and R predicting relations, further calculations are required for a meaningful comparison. First, calculate M , R , and then L (if not used as input variable) for main-sequence stars only. Then, plot $\log M - \log L$ and $\log M - \log R$ diagrams and fit the preferred functions (ML or MR) using the least squares method. Finally, ML/MR becomes comparable to MLR/MRR of Eker et al. (2018). Why bother doing that, if there are many reliable direct methods of obtaining M , R , and L of main-sequence stars within accuracy 1% and a few % respectfully from radial velocity and light curves of DDEB stars, which are marked in the bottom of Figure 1 covering the full ranges of stellar masses. Thus, ML/MR is incompatible with classical MLR/MRR (Figure 1).

2.1.3. Recognition of statistical MLRs

The classical form of MLR ($L \propto M^\alpha$) appreciated by Cester et al. (1983), Griffiths et al. (1988), Karetnikov (1991) and Demircan & Kahraman (1991) before the break initiated by Andersen (1991). This classical form continued by Ibanoglu et al. (2006) when comparing mass-luminosity relations for detached and semidetached Algols despite Andersen (1991)’s exclamation. The most recent examples are by Eker et al. (2015, 2018). The classical or any other form reducible to the classical ($L \propto M^\alpha$) has the advantage of being easy to interpret with a value given to the power of M , which is known to change by the energy generation rate per star mass at the cores of stars. Thus, the derivative of MLR function (dL/dM), the inclination of a line, on the $\log M - \log L$ diagram is the value of alpha. On the other hand, the real advantage is not only that it works in both directions (M from L , or L from M), but also because it permits

one to relate typical masses and luminosities of main-sequence stars in general.

Obviously, the statistically determined relationship between M and L for the main-sequence stars is not true for a single star. This is because L , R , and T_{eff} of a star change with time, while M of the star stays constant (an evolutionary effect) because mass loss of main-sequence stars (especially for the ones cooler than B spectral types) is too small; thus, mass loss is usually ignored (Daszyńska-Daszkiewicz & Miszuda 2019; Bressan et al. 2012). Moreover, there is a metallicity effect that also changes L , R , and T_{eff} slightly, therefore, stellar structure and evolution models use chemical composition and M as the two basic free parameters for computing L , R , and T_{eff} , which stands for the output of an internal structure model to be confirmed externally. Finally, it can be concluded that any kind of relation between M and L of a single star cannot easily be deduced from evolutionary tracks or isochrones. However, the distribution of available stellar luminosities on H-R diagrams or on $\log M - \log L$ diagrams clearly shows that there must exist, at least a statistical, one-to-one relation between a typical mass and typical luminosity of main-sequence stars. However, if L and M were totally independent, identification of main-sequence stars on the H-R diagram would not be possible. In fact, the main-sequence stars were first recognised just according to their extraordinary positional appearance, even on very primitive H-R diagrams. Because of their distinct positions, they were named main-sequence stars, which are still actively used. After all, it is obvious to everyone now that as soon as main-sequence luminosities are placed on a $\log M - \log L$ diagram, a one-to-one relation between M and L shows itself clearly with high-level statistical significance.

What has actually happened so far is that; the statistical relation between stellar M and L for main-sequence stars is so strong and obvious that it was discovered even before the stellar structure and evolution theory was fully established. That was the first reason why it had been evaluated as one of the fundamental secrets of the cosmos, similar to the H-R diagram itself (why are stars not distributed evenly on the surface of the H-R diagram but mostly gathered on the main sequence?). The second reason was that the observational accuracy of those early years of astrophysics was not sufficient to distinguish it as

a statistical relation; therefore, it was treated as a fundamental relation even though some serious objections mentioned above have occurred. Nevertheless, no one has yet clearly declared that MLR is just a statistical relation.

Andersen (1991) totally rejected the existence of a real relation between M and L of the main-sequence stars because, according to him, a unique relation (like a Planck law, keeping T_{eff} constant, the deviations from the Planck curve are only due to random errors of observed intensities) does not exist since deviations from a fitting curve (MLR) is not just only due to random observational errors of L and M , but also due to chemical composition and age differences. Eker et al. (2015, 2018) defended the existence of an MLR relation by claiming that any sample of data could be expressed by a unique relation because a unique fit of a curve on sample data is guaranteed by the least squares method.

However, this defence occurred intuitively because the distinction between MLR as a fundamental or statistical relation was not yet fully established. Even Eker et al. (2015) said “One of the fundamental secrets of the cosmos, the famous stellar mass–luminosity relation (MLR), was discovered empirically ...”. Only later, Eker et al. (2018) declared “The main-sequence MLR is one of the fundamentally confirmed and universally recognised astronomical relations”.

How to solve non-uniqueness problems attributed to the light curves of spotted stars, which is a type of problem Andersen (1991) pointed out against MLR, was discussed first by Eker (1999). The same principles adopted by Eker et al. (2018) for defending the uniqueness of MLR, MRR, and MTR functions from the most accurate masses and luminosities of 509 main-sequence stars as the components of DDEB in the Solar neighbourhood of the Milky Way. There could be three types of non-uniqueness problems. According to Eker et al. (2018), there is no non-uniqueness problem of type I because the preferred function expressing MLR is a power law ($L \propto M^\alpha$). There should not be a non-uniqueness problem of type II also because there exist many methods like the least squares for one to achieve a unique fit and determine its coefficients uniquely. Finally, the problem of type III does not exist either because the parameter space of MLR is so simple that there is always one correlation between L and M , that is, there is only one L value for a given M and vice versa in the case of inverse MLR. The most general approach to non-uniqueness problems was recently applied to main sequence BC- T_{eff} relations by Eker et al. (2021b) when discussing the chronic zero-point problems of the BC scale, which is important for obtaining accurate L of single stars from apparent magnitudes if distances are known.

Apparently, there is no non-uniqueness problem associated with classical MLR, but one may still run into problems of obtaining accurate L from a given M or vice versa. Such problems are inevitable because classical MLR is not devised solely for obtaining accurate L from an accurate M or vice versa. The main obstacle for obtaining accurate M of a single star from its L using classical MLR is not because of the absence of a

unique function (Andersen 1991), but because of the degeneracy induced by stellar structure and evolution theory (Eker et al. 2018). This is because, theoretically, there are an infinite number of L values for a main-sequence star of given M depending on its chemical composition and age. Thus, varying chemical composition and ages are not necessary to cause non-uniqueness to an existing MLR. On the contrary, the chemical composition and age of a star break inferred degeneracy to obtain accurate L , M , and R , which appear on classical MLR and MRR functions as only variables. Therefore, one must conduct further investigation on evolutionary tracks. Knowing the mass and chemical composition of a star, the correct track will be chosen. By knowing the age, both L and R will be read on the track. If the age is not known, then either L or R must be known to read the age of the star on the track. Stellar structure and evolution theory is useful for determining the accurate mass of a single star from its accurately determined $[\text{Fe}/\text{H}]$ and L , where the value of R could also be obtained if T_{eff} of the star is known accurately.

Without distinguishing them from a fundamental relation, Eker et al. (2015) calibrated four linear MLR functions covering the mass range $0.38 < M/M_\odot < 32$, using masses and luminosities of 268 main-sequence stars selected from 514 stars as the components of 257 DDEB from the catalogue of Eker et al. (2014). Three distinct break points separating the four distinct mass domains on a $\log M - \log(L/M)$ diagram were identified. The mass domains were named as low mass ($0.38 < M/M_\odot \leq 1.05$), intermediate mass ($1.05 < M/M_\odot \leq 2.4$), high mass ($2.4 < M/M_\odot \leq 7$), and very high mass ($7 < M/M_\odot \leq 32$). The linear MLRs of the four mass domains were compared to linear and quadratic MLR of the full range $0.38 < M/M_\odot < 32$ and the four-piece linear MLRs were found to best represent the data on a $\log M - \log L$ diagram. The break points separating the mass domains were interpreted as abrupt changes in the power of M , most probably due to changes in the type of efficient nuclear reaction operating in the cores of main-sequence stars.

The statistical nature of MLR was sensed but not fully grasped yet by Eker et al. (2018). The referees were against calibrating new MLRs, which are useless in predicting M and R of single stars. The new trend in determining MLRs was to use them to obtain M and R of single stars, as done by Andersen (1991), Henry (2004), Malkov (2007), Torres et al. (2010), and Gafeira et al. (2012). Therefore, the justifications for recalibrating them again after only three years were explained by Eker et al. (2018) as: There are two tables in the handbook of astronomers, commonly known as “Allen’s Astrophysical Quantities” (Cox 2000). The first of the two tables lists calibration of MK spectral types with seven columns spectral type, $M(V)$, $B - V$, $U - B$, $V - R$, $R - I$, T_{eff} and BC (Table 15.7 on page 388). The second table with six columns spectral type, mass, radii, surface gravity, mean mass density, and rotational speed (Table 15.8 on page 389) is actually at continuation of the first table. The columns of the two tables were thus connected

by spectral types. The second table has a notification mark to say “columns containing uncertain values”, which actually indicates statistically determined typical masses, radii, surface gravity, and mean mass for a given spectral type. The rationale of the new paper was obvious that interrelated MLR, MRR, and MTR would be very useful in supplying reliable statistical information to the astronomical community.

After three years, Eker et al. (2018), this time, calibrated a six-piece MLR covering the mass range $0.179 < M/M_{\odot} < 31$, using 509 main-sequence stars selected from 639 stars as the components of 318 pairs (DDEB) and one detached spectroscopic triple. One should not be surprised by the higher increasing rate of the calibrating stars, which appears to be 90% while the number of newly added DDEB binaries is only 24%. This is because stars with less accurate M and R up to 15% were used in the calibrations rather than up to 3% as in the previous study. Thus, Eker et al. (2018) concluded that it is not always good to eliminate less accurate data for a better study because it may mean loss of information rather than gain. Lowering the limiting relative accuracy to 15% was a significant contribution to extending the low mass limit down to $0.179M_{\odot}$ from $0.38M_{\odot}$ and discovery of two more break points on the $\log M - \log L$ diagram. That is, adding new DDEB stars (24%) to the list was not as effective as lowering the limiting accuracy.

The distribution of the luminosities of 509 main-sequence stars on a $\log M - \log L$ diagram is shown in Figure 2, where the vertical lines mark the positions of the break points. Between the break points, there is a linear MLR luminosity of that domain; thus, there exists a six-piece MLR to cover the full range $0.179 < M/M_{\odot} \leq 31$. A six-degree polynomial, shown by a blue dotted line to fit the full range, was found producing a best fit better than the higher and the lower degree polynomials to explain the full range data by a single function. It is obvious in Figure 2 that the six-piece MLRs are even better at representing stellar luminosity than any polynomial of any degree.

The six-mass domains, which are named ultra-low mass ($0.179 < M/M_{\odot} \leq 0.45$), very-low mass ($0.45 < M/M_{\odot} \leq 0.72$), low mass ($0.72 < M/M_{\odot} < 1.05$), intermediate mass ($1.05 < M/M_{\odot} \leq 2.4$), high mass ($2.4 < M/M_{\odot} \leq 7$), and very-high mass ($7 < M/M_{\odot} \leq 31$), and their best fitting MLR functions are shown in Figure 3, where they were also compared to a single MLR function of sixth degree covering the entire mass range $0.179 < M/M_{\odot} \leq 31$. Analytical expressions and statistical parameters N (number of stars in the domain), R^2 (correlation coefficient), σ (standard deviation), and α (the power of M) as the inclination of a linear MLR on a $\log M - \log L$ diagram are listed in Table 2.

2.2. Revisiting MRR

Although it appears to be natural to sense a relation between M and R of main-sequence stars immediately after the discovery of MLR by Hertzsprung (1923) and Russell et al. (1923), the

empirical MRR of main-sequence stars did not appear in the literature for another one and a half decades. Kuiper (1938), who was suspicious about MLR being one of the fundamental relations, also plotted a $\log M - \log R$ diagram but did not discuss it. Only after mid of the 20th century, the studies discussing empirical stellar mass-radius relation (MRR) begin to appear in the literature (McCrea 1950; Plaut 1953; Huang & Struve 1956; Lacy 1977, 1979; Kopal 1978; Patterson 1984; Gimenez & Zamorano 1985; Harmanec 1988; Demircan & Kahraman 1991).

If M and L are related, why not M and R , since L is already known to be related to the square of R according to the Stefan-Boltzmann law? The main obstacle seems to be the difficulty of accessing reliable stellar radii. McCrea (1950) appears to be one of the first founders of the idea for two reasons: *i*) Using the light curve solutions of eclipsing binaries, not necessarily all being detached, that is, including W UMa binaries too, Plaut (1953) has drawn a diagram in the manner proposed by McCrea (1950). *ii*) Readers were referred to McCrea (1950) for theoretical interpretation of the relation in the form $\log(M/R) = a + b \log M$ suggested by Plaut (1953). Using the parameters of 30 systems with both components on the main sequence chosen from 130 eclipsing binaries of all kinds compiled by Plaut (1953), the coefficients of the relation were rectified as $a = -0.058 \pm 0.026$, $b = 0.335 \pm 0.29$ with a dispersion of ± 0.11 according to the least squares.

The masses and radii of the eclipsing stars compiled by Plaut (1953) had been studied by Huang & Struve (1956), who plotted them on two separate spectral type- $\log R$ diagrams, on which both components are smaller, thus not touching, both components are touching, primary is touching but secondary is not, and the secondary is touching but the primary is not touching. The inner contact surfaces were marked by special symbols for each. The two separate diagrams made Huang & Struve (1956) believe that the sub-giant components in such systems could have evolved from early main-sequence stars.

Empirical MRR in the form $\log R(M) = 8.495 - 0.2M_{\text{Bol}}(M) - 2 \log T_{\text{eff}}(M)$ suggested by Hoxie (1973) for the low mass stars ($M < 1M_{\odot}$) in the Solar neighbourhood. Comparing this MRR with low-mass model calculations of stellar R , Hoxie (1973) announced a discordance implying that theoretical radii are 30% or smaller than the observationally derived radii in the mass-radius plane for stars of mass less than $0.5M_{\odot}$. Subsequently, a method for estimating R of nearby stars was declared by Lacy (1977). Based on the Barnes-Evans relation and free of assumptions of spectral types, luminosity class, effective temperature, or bolometric correction, this method is applied to nearby single and double stars with accurate parallaxes and $V - R$ photometry. The double stars (visual binaries) were useful to supply components M and R , where R needed to be compared with predicted R by the new method with Barnes-Evans relation. Additional comparison was also possible to Lacy (1977) using R from non-contact eclipsing binaries with well-determined dimensions selected from Batten (1967)

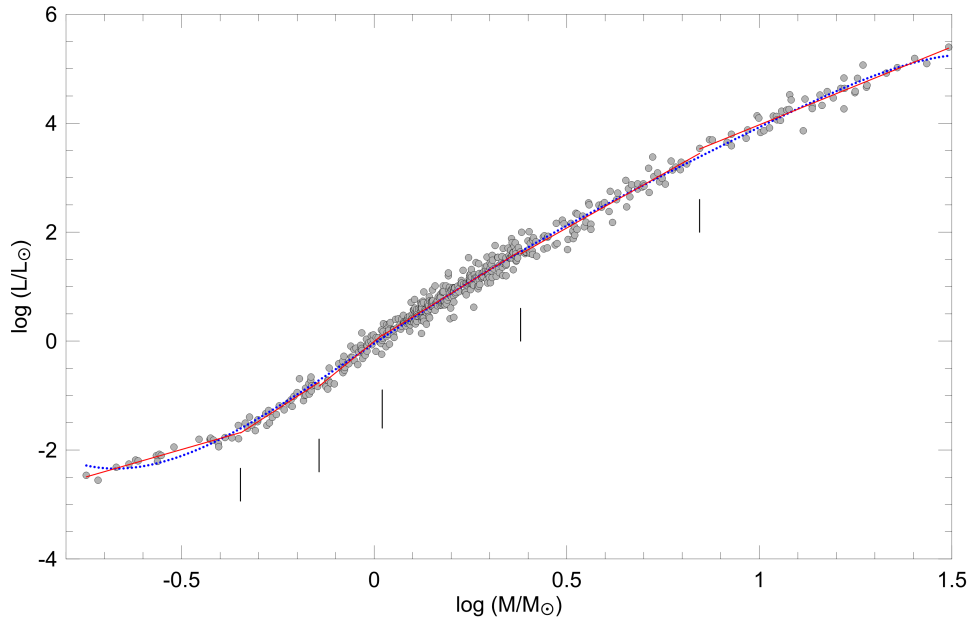


Figure 2. The dotted (blue) line is a sixth-degree polynomial, the solid (red) lines are classical MLRs, and the vertical lines are the break points separating the mass domains where the linear lines were fitted (credit to [Eker et al. 2018](#)).

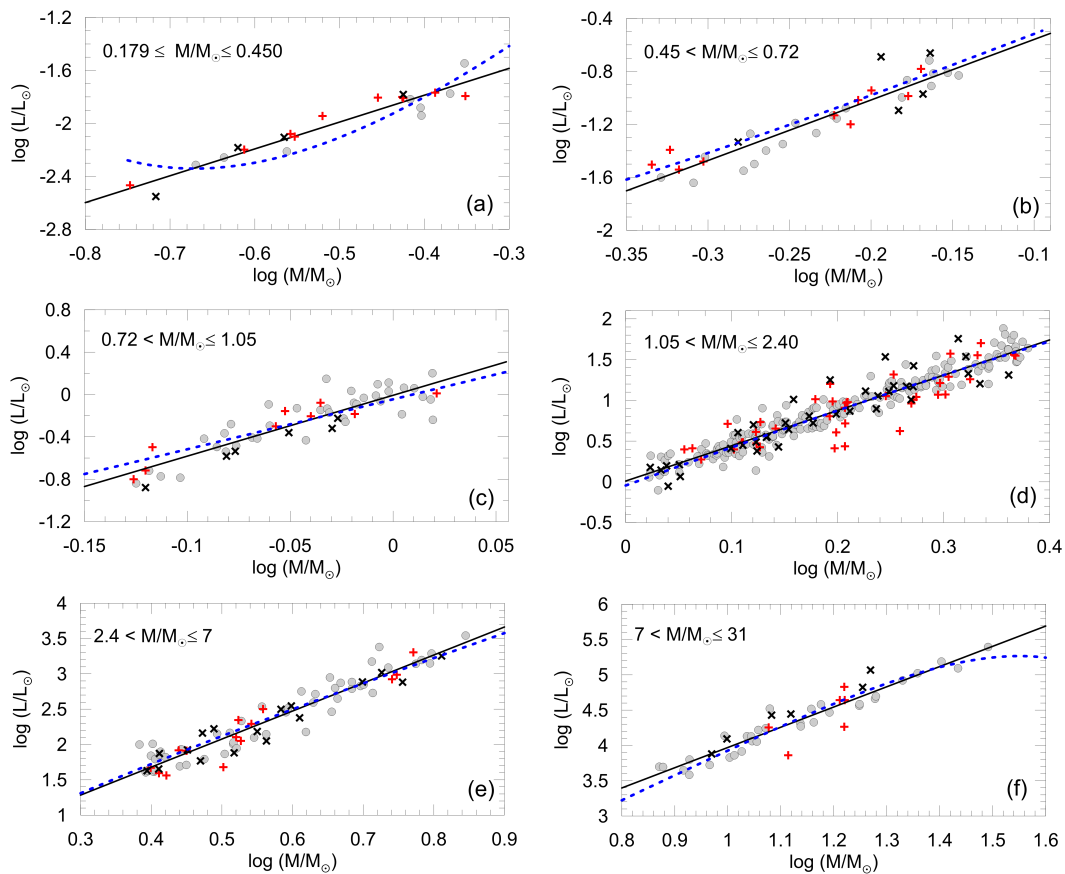


Figure 3. Mass domains and classical MLRs representing stellar masses and luminosities in each domain. 6th-degree polynomial representing all data (same as the dotted blue line in Figure 2) is not as successful as linear MLRs in low-mass domains ($M < 1.05$) and very high-mass domain ($M > 7$). Data accuracy is: (o) very accurate < 3%, (+) accurate (3-6%), and (x) less accurate (6-15%) (credit to [Eker et al. 2018](#)).

Table 2. Classical MLRs for main-sequence stars in various mass domains (credit to Eker et al. 2018).

Domain	N	Mass Range	Classical MLR	R^2	σ	α
Ultra low mass	22	$0.179 < M/M_{\odot} \leq 0.45$	$\log L = 2.028(135) \times \log M - 0.976(070)$	0.919	0.076	2.028
Very low mass	35	$0.45 < M/M_{\odot} \leq 0.72$	$\log L = 4.572(319) \times \log M - 0.102(076)$	0.857	0.109	4.572
Low mass	53	$0.72 < M/M_{\odot} \leq 1.05$	$\log L = 5.743(413) \times \log M - 0.007(026)$	0.787	0.129	5.743
Intermediate mass	275	$1.05 < M/M_{\odot} \leq 2.40$	$\log L = 4.329(087) \times \log M + 0.010(019)$	0.901	0.140	4.329
High mass	80	$2.4 < M/M_{\odot} \leq 7$	$\log L = 3.967(143) \times \log M + 0.093(083)$	0.907	0.165	3.967
Very high mass	44	$7 < M/M_{\odot} \leq 31$	$\log L = 2.865(155) \times \log M + 1.105(176)$	0.888	0.152	2.865

and Koch et al. (1970). Having a sufficient number of accurate masses and radii (both 5% or better) from the visual systems and non-contact eclipsing binaries, Lacy (1977) was also able to produce the most reliable $\log M - \log R$ diagram so far, where the empirical relation of Hoxie (1973) was plotted with a special symbol different from the symbols of visual binaries, eclipsing systems that have undergone mass exchange and without any mass exchange.

Therefore, Lacy (1977) suggested $\log R = 0.640 \log M + 0.011$ for the region $0.12 \leq \log M \leq 1.30$ and $\log R = 0.917 \log M - 0.020$ for the region $-1.00 \leq \log M \leq 1.30$ as two MRR functions to indicate the zero-age main sequence (ZAMS), where R and M are in Solar units. Lacy (1977) interpreted the break point as a signal crossing over from the region of the p-p chain to the C-N-O cycle. The terminal age main sequence (TAMS) line was deduced from the models of Iben (1967) and Paczyński (1970) marked on the $\log M - \log R$ as a dashed line, while ZAMS is shown by a continuous line with a break at $1.3 \pm 1M_{\odot}$. Theory and observation were found to be in good agreement for stars $M \gtrsim 1M_{\odot}$, but the models of M dwarfs having 25% smaller radii than real stars. Another line of development used the Catalogue of the Elements of Eclipsing Binaries (Kopal & Shapley 1956), where Kopal (1959) obtained a good statistical definition of the MRR. He found a linear relation, in logarithmic scales, for the values of individual stars irrespective of being primary or secondary, but the slope is different for massive and less massive stars with a transition at $\sim 2M_{\odot}$ (Kopal & Shapley 1956; Kopal 1978). Popovici & Dumitrescu (1974), who compiled data from Kopal & Shapley (1956) and Svetchnikoff (1969)², were mainly interested in the radius-luminosity diagram. Five mean empirical mass-radius relations had been constructed by Habets & Heintze (1981). The number of MRR is five because it is calibrated not only for main-sequence stars but also for luminosity class IV (subgiants), III (giants), V_{\odot} (ZAMS) and EV_{\odot} (EZAMS) using visual and eclipsing binaries which are at the same time double-lined spectroscopic systems collected by themselves. Patterson (1984) was unsatisfied by the MRRs suggested before him, thus he proposed the empirical ZAMS mass-radius relation in the form $R = \alpha M^{\beta}$, where M and R in Solar units

and $\alpha = 1$, $\beta = 0.88 \pm 0.02$ for the region $0.1 \leq M/M_{\odot} \leq 0.8$ and $\alpha = 0.98$, $\beta = 1.00$ for the region $0.8 \leq M/M_{\odot} \leq 1.4$ by a quotation “poorly defined for $M \leq 0.4M_{\odot}$ ” for himself to apply it to cataclysmic variables. Gimenez & Zamorano (1985) preferred using the Catalogue of Stellar Masses and Radii published by Popper (1980) for studying the classical MRR on $\log M - \log R$ diagram. Using reliable M and R from OB and B6-M detached eclipsing and visual binaries and resolved spectroscopic binaries, Gimenez & Zamorano (1985) determined $a = 0.041 \pm 0.011$ and $b = 0.749 \pm 0.011$ for an MRR in the form $\log R = a + b \log M$ with a correlation coefficient 0.96.

It must be noted that Lacy (1977, 1979), Gimenez & Zamorano (1985) and Demircan & Kahraman (1991) presented their $\log M - \log R$ diagrams without fitting an MRR function to the data, but with a ZAMS line as the lower limit and a TAMS line as the upper limit of main-sequence stars, which are estimated with the help of theoretical stellar structure and evolution models. The most recent example is by Eker et al. (2018) is shown in Figure 4, where it is clear that the statistical MRR does not appear as strong as the classical MLR expressed on $\log M - \log L$ diagram (Figure 3). Considering the difference in data distribution on both diagrams $\log M - \log L$ and $\log M - \log R$, it is not difficult to understand why $\log M - \log R$ diagram is presented without a fitting curve like Figure 3.

Because of the very large scatter caused by the evolution of stars $M \gtrsim 1.3M_{\odot}$ ($\log M > 0.15$), data of main-sequence stars on a $\log M - \log R$ diagram are not suitable for expression by a function or a curve. Obviously, plotting a ZAMS MLR on a $\log M - \log R$ diagram permits one to see the evolution of stellar radii for main-sequence stars $M \gtrsim 1.3M_{\odot}$.

Despite its hassle-free appearance and tight and narrow distribution of stellar L on a $\log M - \log L$ diagram for the full mass range of main-sequence stars, different forms of MLR functions causing confusion were suggested, calibrated, and shown together with the data. Looking at the already suggested main sequence MLR and MRR functions so far, one should see another noticeable difference. Contrary to the different forms of MLR suggested by different study groups, the main sequence MRR in the form $\log R = a + b \log M$ were common. The form $R \propto M^{\beta}$ suggest by Patterson (1984), Demircan & Kahraman (1991) and Karetnikov (1991), appears different, but it is not. The same form of function is expressed once in logarithmic form, while the other is a power law.

² Catalog Orbitalnii Elementov, Mass i Svetimostii Tesnii Dvornik Svezd, Sverdlovsk

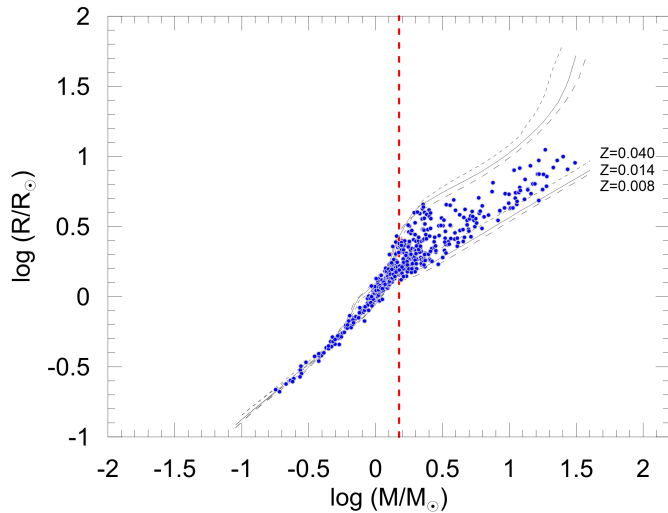


Figure 4. Main sequence mass-radius diagram of DDEB stars. ZAMS and TAMS lines are from the PARSEC models of Bressan et al. (2012) (credit to Eker et al. 2018). The vertical line is a division at $M = 1.5M_{\odot}$ ($\log M = 0.176$).

Despite such obvious differences (appearance on a diagram, formal expression), similarities between MLR and MRR studies also exist. Andersen (1991)’s exclamation against classical MLR also affected MRR studies; thus, modern MRR also appears to have deviated from the main path. Older MRR studies aimed to calibrate an MRR relation for two practical purposes: *i*) to get an answer to the question: how mean (or typical) M and R of main-sequence stars are related? *ii*) to estimate R of a star for a given M , or vice versa. The former is useful for making models that require mean M and R , and the latter is useful for guessing the R of a star from its M , or vice versa. Models using mean M and R as well as mean L , have a larger application area not only in stellar astrophysics but also in Galactic and extra-galactic studies.

The exclamation of Andersen (1991), unfortunately, caused the first aim to be neglected. As explained above, in the new trend of calibrating MLR, there is only one aim: to obtain the most accurate M and R together from the other observed parameters of the star. Thus, Malkov (2007), Torres et al. (2010), Moya et al. (2018), and Fernandes et al. (2021) have not only calibrated a single relation for predicting R of a single star but also at least one more relation useful to deliver M of the same star. Thus, the new trend of MRR cannot be considered independent of the new trend of MLR appearing after Andersen (1991).

2.3. Revisiting MTR

If M and L are related, why not M and T_{eff} since L is known to be equal to the surface area times the surface flux, where the flux is proportional to the fourth power of the effective temperature. A relation even stronger than mass-radius is expected because the power of T_{eff} is two times greater than the power of R in the Stefan-Boltzmann law. Its calibration and usage

also appear easier than the calibration and usage of the MRR relation. Regardless, except for the spectral type-effective temperature (horizontal axis of the H-R diagram) relationship, it took almost sixty years for a MTR to appear in the literature.

First empirical mass- T_{eff} relation is studied by Habets & Heintze (1981) and shown on a $\log M - \log T_{\text{eff}}$ diagram for main sequence-stars after studying newly calibrated mass-spectral type and spectral type- T_{eff} relations from the main-sequence components of eclipsing binaries. The empirical relation was shown together with two theoretical mass- T_{eff} relations of Stothers (1974, for a metallicity $Z = 0.02$ with $Y = 0.49$ and 0.25) and the one by Demarque & Gisler (1975, for $Z = 0.02$ and $Y = 0.25$). The form of the relation was not given. Karetnikov (1991) later determined coefficients of mass- T_{eff} relation in the form $\log T_{\text{eff}} = a + b \log M$ for six different types of eclipsing systems using absolute parameters of 303 eclipsing binaries of different types with varying and constant orbital periods without showing them on diagrams. The relations were determined for primaries and secondaries separately; thus, coefficients of 24 relations were determined and listed without showing them on $\log M - \log T_{\text{eff}}$ diagrams.

Apparently, MTR relation had also been affected by Andersen (1991)’s objection to MLR because Malkov (2007) announced a direct $[\log T_{\text{eff}} - (\log M)]$ and an inverse $[\log M - (\log T_{\text{eff}})]$ mass-effective temperature relations together with his M and R predicting relations and their inverse functions. Like $\log M - \log L$ diagram without a fitting curve, his M versus $\log T_{\text{eff}}$ diagram is too presented without a fitting curve. Being not interested in calibrating an MTR, Moya et al. (2018), on the other hand, used T_{eff} as one of the free parameters for predicting M and R of single stars. Moya et al. (2018), calibrated 38 relations: 18 for M and 20 for R . This is very much similar to Torres et al. (2010) who suggested only two relations using T_{eff} , $\log g$ and $[\text{Fe}/\text{H}]$ as free parameters, one for obtaining M one for obtaining R , to replace classical MLR claimed inadequate to provide stellar M by two reasons: *i*) It is a mean relation, thus M from L is very inaccurate. *ii*) Scatter on $\log M - \log L$ diagram is not only due to random observational errors of M and L but also due to stellar age and chemical composition differences. As if, a reliable (or true) MLR function must contain all the parameters that introduce scattering. Such an MLR function, however, cannot be drawn on a $\log M - \log L$ diagram.

On the other hand, following the old tradition of looking for mean relations for MRR and MTR, Eker et al. (2015) have compared L , R , and T_{eff} distributions on $\log M - \log L$, $\log M - \log R$ and $\log M - \log T_{\text{eff}}$ diagrams. The first comparison between $\log M - \log L$, $\log M - \log R$ has been commented as: “the appearance of data on the $\log M - \log R$ diagram is very different from the appearance on the $\log M - \log L$ diagram (compare Figures 2 and 4), which rather looks like a band of data expressible by a function; however, with a very narrow distribution of radii for masses $M < 1M_{\odot}$ and a broad band of radii for stars with $M > 1M_{\odot}$, a single function to express a MRR would be odd and meaningless”. Then, a comparison between

$\log M - \log R$, $\log M - \log T_{\text{eff}}$ were commented as: “the temperature evolution within the main-sequence band is not that obvious on the $M - T_{\text{eff}}$ diagram. At first glance, it resembles the MLR”. It is indeed not like MRR, where the main-sequence evolution of R is obvious for $M > 1M_{\odot}$ (compare Figures 2, 4, and 5).

Despite the distribution of data on $\log M - \log T_{\text{eff}}$ diagram (Figure 5) resembles the distribution of data on $\log M - \log L$ diagram, Eker et al. (2015) preferred not to calibrate a mean MTR because it would have been odd or inappropriate to oppose literature where MLR and MRR are many, but MTR is almost absent. Later, Eker et al. (2018) noted: “Stefan–Boltzmann law clearly indicates that stellar luminosity are related to stellar radii and effective temperatures. Having empirically determined the MLR and MRR available, one is not free to determine another independent mass–effective temperature relation (MTR)”. The three independently calibrated MLR, MRR, and MTR functions are not guaranteed to give consistent L , R , and T_{eff} for a given M . The solution to the problem is given in the next subsection.

2.4. Revisiting interrelated MLR, MRR, and MTR

It has been noticed that the distribution of R on the $\log M - \log R$ diagram (Figure 4) on the left of the vertical line ($M \leq 1.5M_{\odot}$) is smooth and tight, that is, it is expressible by a simple function, which is to be called MRR. However, in the high mass region $M > 1.5M_{\odot}$ due to faster evolution, R values are scattered very much, and thus, its band-like appearance does not seem expressible by a curve of a function.

Despite its overall appearance resembling an MLR, the T_{eff} distribution on the $\log M - \log T_{\text{eff}}$ diagram shows almost opposite characteristics when choosing the same mass domain to calibrate an MTR. One can easily notice that the low-mass region $M \leq 1.5M_{\odot}$ (left of the vertical line) in Figure 5 has a tight but wavy distribution, which is rather not possible to fit a simple function. On the contrary, one can easily spot the domain of high-mass stars $M > 1.5M_{\odot}$ (right of the vertical line) in Figure 5 with a sufficiently tight but smoothly varying distribution, which is easily expressed by a function called MTR.

Having six linear MLRs already calibrated (Table 2, Figures 2 and 3) for the main-sequence stars in the full range of observed stellar masses, probable inconsistencies among the mean L , R , and T_{eff} values for a given M will be eliminated if the MRR was calibrated for the low-mass region $M \leq 1.5M_{\odot}$ only and the MTR was calibrated for the high-mass region $M > 1.5M_{\odot}$ only. This is because the vertical line is a dimensionless border between the low- and high-mass regions in both R and T_{eff} distributions as shown in Figures 4 and 5. Otherwise, with independently calibrated MLR, MRR, and MTR functions, we obtain a mean luminosity ($\langle L \rangle$), a mean radius ($\langle R \rangle$), and a mean effective temperature ($\langle T_{\text{eff}} \rangle$) for a given M . No one would know which of the three mean values are wrong because the mean $\langle L \rangle$ will not be equal to the mean

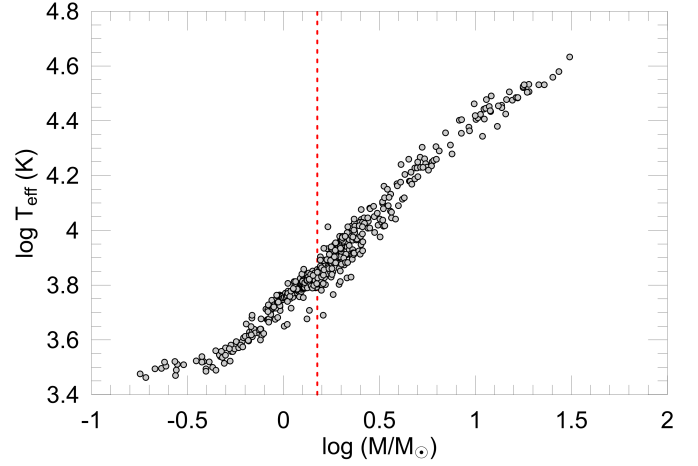


Figure 5. Main sequence mass-effective temperature diagram of DDEB stars (credit to Eker et al. 2018). The vertical line is a division at $M = 1.5M_{\odot}$ ($\log M = 0.176$).

surface area $\langle 4\pi R^2 \rangle = 4\pi(\langle R^2 \rangle)$ multiplied by the mean surface flux $\langle \sigma T^4 \rangle = \sigma(\langle T_{\text{eff}}^4 \rangle)$ for a typical main-sequence star of given M . Choosing the most eligible regions on $\log M - \log R$ and $\log M - \log T_{\text{eff}}$ diagrams as compensating mass domains for covering the full mass range, not only removes a probable inconsistency but also guarantees the most trustable MLR and MRR for the low-mass stars ($M \leq 1.5M_{\odot}$) and the most trustable MLR and MTR for the high-mass stars ($M > 1.5M_{\odot}$). Then, one could calculate consistent $\langle L \rangle$, $\langle R \rangle$ and $\langle T_{\text{eff}} \rangle$ for the full range of main-sequence stars, which occurs in two steps for both mass domains. For low-mass stars: *i*) Use MLR and MRR to calculate $\langle L \rangle$ and $\langle R \rangle$ for a given mass, *ii*) use Stefan-Boltzmann law to calculate $\langle T_{\text{eff}} \rangle$ for the same mass from its already computed $\langle L \rangle$ and $\langle R \rangle$. For high-mass stars: *i*) Use MLR and MTR to calculate $\langle L \rangle$ and $\langle T_{\text{eff}} \rangle$ for a given mass, *ii*) use Stefan-Boltzmann law to calculate $\langle R \rangle$ for the same mass from its already computed $\langle L \rangle$ and $\langle T_{\text{eff}} \rangle$.

Utilising the least squares, Eker et al. (2018) determined an empirical MRR directly from M and R of 233 main-sequence stars for low-mass stars within range $0.179 \leq M/M_{\odot} \leq 1.5$, and an empirical MTR from $\log M$ and $\log T_{\text{eff}}$ of 276 main-sequence stars for high-mass stars within range $1.5 < M/M_{\odot} \leq 31$. Because the table giving the empirical MRR and MTR by Eker et al. (2018) has misprints, the open forms of the functions, correlation coefficients (R^2), and standard deviations (σ) from Eker et al. (2021a) are given here. The empirical MRR in the form of a quadratic equation, where R and M are Solar units, is:

$$R = 0.438(0.098) \times M^2 + 0.479(0.180) \times M + 0.137(0.075), \quad (3)$$

has $R^2 = 0.867$ and $\sigma = 0.176$. The empirical MRR in the form of a quadratic equation, where T_{eff} and M are the Kelvin and Solar units, is:

$$\log T_{\text{eff}} = -0.170(0.026) \times (\log M)^2 + 0.888(0.037) \times \log M + 3.671(0.010), \quad (4)$$

has $R^2 = 0.961$ and $\sigma = 0.042$.

The empirical MRR and MTR by Eker et al. (2018) are

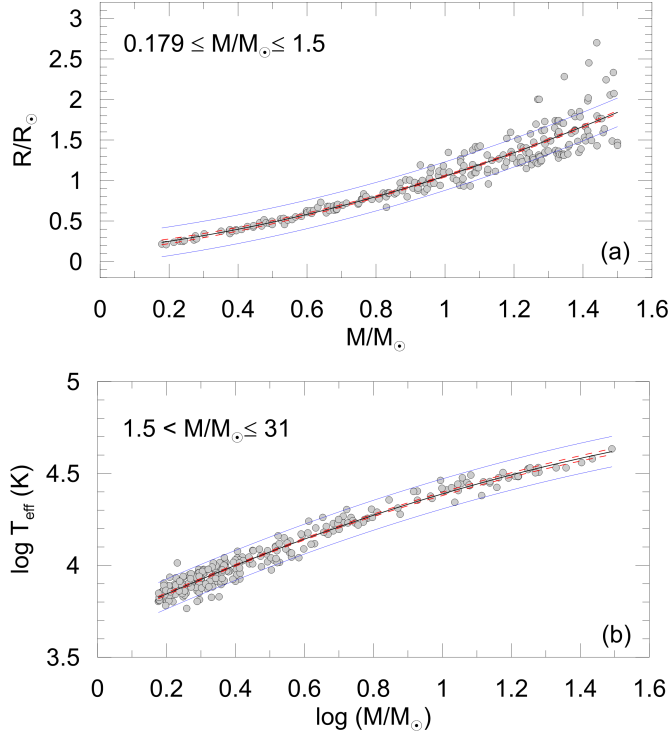


Figure 6. Empirical MRR and MTR calibrated from 509 main-sequence stars for the mass ranges $0.179 \leq M/M_{\odot} \leq 1.5$ and $1.5 \leq M/M_{\odot} \leq 31$ of DDEB stars. Note that MTR is on a logarithmic scale, but MRR is not (credit to Eker et al. 2018).

shown together with data in Figure 6. The division between the low- and high-mass stars at $1.5M_{\odot}$ is a nice coincidence that plots of MRR and MTR appear with the same numbers in the horizontal axis; thus, one must be careful that MTR is shown on a logarithmic scale while MRR is not.

The mean values ($\langle L \rangle$, $\langle R \rangle$, $\langle T_{\text{eff}} \rangle$) computed from the empirical MLR, MRR, and MTR of Eker et al. (2018) are compared to L , R and T_{eff} of 509 main-sequence stars chosen from 318 DDEB and one detached eclipsing triple, as shown in Figure 7. The solid lines mark the mean values calculated directly from MLR, MRR, or MLR, MTR, while the dotted lines mark the mean values $\langle T_{\text{eff}} \rangle$ calculated from $\langle L \rangle$, $\langle R \rangle$ for the low-mass stars and $\langle R \rangle$ calculated from $\langle L \rangle$ and $\langle T_{\text{eff}} \rangle$ for the high-mass stars.

Calculating the mean values ($\langle L \rangle$, $\langle R \rangle$, $\langle T_{\text{eff}} \rangle$) in two steps as described above has the advantage of further checking them and confirming whether the mean values of the first step is consistent or not. Note that, only if $\langle L \rangle$ and $\langle R \rangle$ values of the low-mass stars are consistent, then in the second step consistent $\langle T_{\text{eff}} \rangle$ values could be produced from $\langle L \rangle$ and $\langle R \rangle$; similarly, only if $\langle L \rangle$ and $\langle T_{\text{eff}} \rangle$ values of high-mass stars are consistent, then in the second step, consistent $\langle R \rangle$ values could be produced according to the Stefan-Boltzmann law. The three break points and varying inclinations of MLR before, between, and after the break points in the mass range $M \leq 1.5M_{\odot}$, apparently, are causing the wavy look of the MTR of low-mass stars. What simple function would have produced the current successful

appearance of the fit displayed in Figure 7c by the dotted line? Similar influence of the break points and effect of varying inclinations of MLR before, between, and after the break points for the high-mass stars $M > 1.5M_{\odot}$ are there in the middle panel (Figure 7b) but appear to be lost within the scatter caused by the faster evolution of more massive stars. Therefore, it is a bull's eye to choose the mass region $M \leq 1.5M_{\odot}$ for devising MRR and to choose the mass region $M > 1.5M_{\odot}$ for devising MTR.

The two-step procedure in determining the mean values of $\langle L \rangle$, $\langle R \rangle$, $\langle T_{\text{eff}} \rangle$ for a given M may appear problematic because it introduces extra errors in the error propagation. Users should not be deceived by this illusion. First, this is because consistent mean values of higher uncertainty are better than inconsistent more accurate ones. To avoid inconsistency, one may use a two-step procedure as described above or use MLR and MRR only or MLR and MTR only for the full mass range of main-sequence stars. Thus, in either case, the two-step procedure is inevitable for consistent results. For the high-mass stars $M > 1.5M_{\odot}$ the scatter on R is too large; thus, authors usually prefer not to determine MRR. In the former case, MRR and MTR would

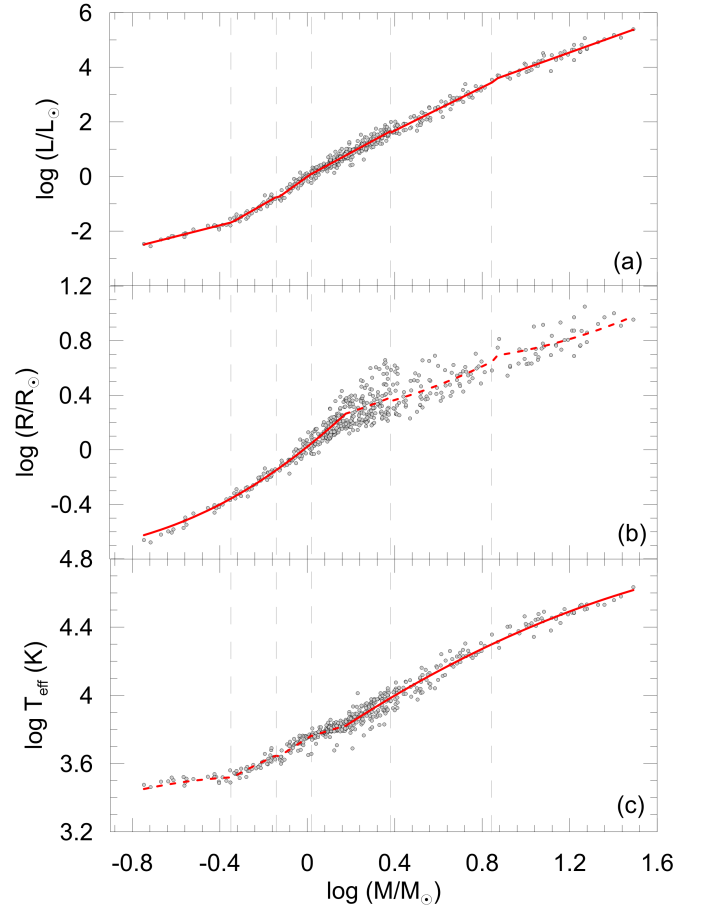


Figure 7. The mean values ($\langle L \rangle$, $\langle R \rangle$, $\langle T_{\text{eff}} \rangle$) computed from empirical MLT, MRR, and MTR are compared to L , R and T_{eff} of 509 main-sequence stars. The mean values taken directly from MLR, MRR or MLR, MTR are solid, The mean values from the Stefan-Boltzmann law are dotted. The dashed vertical lines represent the break points of MLR (credit to Eker et al. 2018).

be missing for high-mass stars, while interrelated MLR, MRR, and MTR would be possible only for low-mass stars. On the other hand, for low-mass stars $M < 1.5M_{\odot}$ it is not possible to find a simple function to fit in determining MTR. Then, interrelated MLR, MRR, and MTR become possible only for high-mass stars since MRR and MTR would be missing for low-mass stars $M < 1.5M_{\odot}$. If one prefers to fit an MRR together with MLR in the full mass region, then he/she will end up having very unreliable $\langle R \rangle$ for the stars $M > 1.5M_{\odot}$. Error propagation, then, would produce similarly unreliable, even worse $\langle T_{\text{eff}} \rangle$ since the independent MTR function is not there. If one prefers to calibrate MLR and MTR in the full range of masses, similar unreliable or erroneous $\langle T_{\text{eff}} \rangle$, $\langle R \rangle$ values emerge for the low mass stars $M < 1.5M_{\odot}$. Therefore, the two-step procedure described in the paragraph before this one in determining the mean values of $\langle L \rangle$, $\langle R \rangle$, $\langle T_{\text{eff}} \rangle$ for a given M is always better and more reliable than the independently determined MLR, MRR and MTR for sure.

3. CONCLUSIONS

Fundamental relations are handy tools to explain simple natural phenomena or starting points for understanding more complex phenomena. The main difference between statistical and fundamental relations is that a statistical relation is valid under certain conditions implied by the data from which it was formulated, whereas a fundamental relation is rather independent of data, that is, data are not there to constrain it but only to confirm or to falsify it. All empirical relations derived from observational or experimental data are statistical in spirit. This does not, however, mean a fundamental relation cannot be derived from observational and/or experimental data. A statistical study could reproduce and may even find a fundamental relationship.

Physical laws are indifferent to fundamental relations. Their scope is wider; for example, the Stefan-Boltzmann law ($L = 4\pi R^2 \sigma T_{\text{eff}}^4$) is valid for all stars radiating thermally and for a hypothetical star representing $\langle L \rangle$, $\langle R \rangle$, and $\langle T_{\text{eff}} \rangle$ implied the main sequence MLR, MRR, and MTR. In contrast, MLR, MRR, and MTR are valid to give mean values for a main-sequence star of a given M within a valid mass range, which was suggested after their calibrations. Because they are not valid for non-main sequence stars, they are also not valid for estimating L , R , or T_{eff} of a main-sequence star with a known M only. This is because, nowadays, many stellar structure and evolution models exist for one to look for L , R , and T_{eff} of a star according to its M , chemical composition (X, Y, Z), and age.

Because of their simplicity, some statistical relations can be mistaken or misused as fundamental relations. A good example of this is the classical MLR. This is because, immediately after its discovery by Hertzsprung (1923) and Russell et al. (1923), for a while, there were no other methods to obtain masses of single stars but estimate them from L or absolute bolometric magnitude (M_{Bol}) by using an MLR in the form of $L \propto M^{\alpha}$ or M_{Bol} - mass diagrams.

Having no alternative is another property of fundamental relations. Indeed, neither the Stefan-Boltzmann law nor the Planck law (spectral energy distribution of a black body with specific temperature) have alternatives. Since there is no alternative to estimate M of a single star, using a classical MLR convinced early astronomers that it could be used as a fundamental relation. Today, there are alternatives to estimating M and R of single stars; thus, there is no excuse to assume any form of MLR as fundamental laws. One might still want to use MLR, MRR, and MTR, as a fundamental law, that is, if he/she is more interested in knowing M of star from its L . This is permissible with a larger uncertainty covering the main sequence at the value of M on a $\log M - \log L$ diagram, simply $\pm 1\sigma$, which is given in Table 2.

On the other hand, statistical relations could be devised to serve a very specific purpose; for example, to obtain M and R of a single star from its other observables. In this respect, a statistical relation may appear to operate like a fundamental relation, but this is an illusion. M and R predicting relations are still statistical relations if their validity depends on the data from which they were calibrated. In addition, because there are many alternatives to provide R or M of a star from its T_{eff} , L , g , ρ , and $[\text{Fe}/\text{H}]$, as expressed by Moya et al. (2018) and as summarised by Serenelli et al. (2021). Malkov (2007), Torres et al. (2010), and Fernandes et al. (2021).

Naming a newly devised or renaming a re-calibrated empirical relation is very important; as important as classifying it as another statistical relation or one of the fundamental laws. Names must be unique to avoid confusion and guide users towards the original purpose of the relation. Repeating the same improper and non-unique names should not be advocated by saying: Let us keep the same name in the past. This will be nothing but insisting on the same error. There are many mis-calling or non-unique naming examples in the past, which are identified with possible correct names in the previous section. Especially after Andersen (1991)'s exclamation that some R and M predicting relations were non-uniquely and incorrectly called MLR. Let us hope, Chevalier et al. (2023), and Malkov et al. (2022) would be the last examples who erroneously named their mass- M_G diagrams, where M_G is absolute brightness in *Gaia* G band, "mass-luminosity" diagram, and their mass - M_G relations "mass-luminosity" relation. Possible unique names for them are the "mass-absolute brightness" diagram or the "mass-absolute brightness" relation at *Gaia* G band.

The empirical relations for predicting M and R of single stars developed as alternatives to classical MLR and MRR after the split, initiated after Andersen (1991)'s exclamation, occurred on the classical path aiming to obtain mean values $\langle L \rangle$, $\langle M \rangle$, and $\langle R \rangle$, and individual L , R , and M of single stars. In this respect, it is not possible for one to say, "the empirical relations giving M and R of single stars are more valuable than the classical MLR and MRR". Claiming the opposite is also not correct. Both schools of thought have useful applications that are valuable concerning their own aims. Empirical M and R

prediction relations have found a fruitful application to explore exoplanets hosting single stars. Estimating M and R of planet-hosting stars is the starting point for exploring hosted exoplanets (Stassun et al. 2017, 2018). Classical MLR, MRR, and MTR, on the other hand, are practical for constructing astrophysical models that need mean values, which are beneficial not only to stellar astrophysics but also to Galactic and extragalactic search, and even to cosmological models.

Further improvements in the prediction accuracy of single star parameters depend mainly on the quantity and quality of the radial velocity and light curve solutions of DDEB. Advances in already established relations or new forms are possible because of the increasing demand for exoplanet investigations. Developments on the classical MLR, MRR, and MTR, on the other hand, are encouraged to include the metallicity effect, as well as to extend them further towards high and low mass limits, not only for the main sequence but also for other luminosity classes.

Peer Review: Externally peer-reviewed.

Author Contribution: Conception/Design of study - Z.E., F.S., S.B.; Data Acquisition - Z.E., F.S., S.B.; Data Analysis/Interpretation - Z.E., F.S., S.B.; Drafting Manuscript - Z.E., F.S., S.B.; Critical Revision of Manuscript - Z.E., F.S., S.B.; Final Approval and Accountability - Z.E., F.S., S.B.; Technical or Material Support - Z.E., F.S., S.B.

Conflict of Interest: Authors declared no conflict of interest.

Financial Disclosure: Authors declared no financial support.

Acknowledgements: The authors thank the anonymous referees who provided valuable comments in improving the quality of discussions in the manuscript. This research has made use of NASA's Astrophysics Data System.

Note: The Co-Editor-in-Chief was not involved in the evaluation and peer-review processes of the article. These processes were carried out by the Editor-in-Chief and the member editors of the editorial management board.

LIST OF AUTHOR ORCIDS

Z. Eker <https://orcid.org/0000-0003-1883-6255>
 F. Soyduğan <https://orcid.org/0000-0002-5141-7645>
 S. Bilir <https://orcid.org/0000-0003-3510-1509>

REFERENCES

- Akbulut B., Ak S., Yontan T., Bilir S., Ak T., Banks T., Ulgen E. K., Paurzen E., 2021, *Ap&SS*, 366, 68
- Albert A., et al., 2021, *ApJ*, 912, L4
- Aller A., Lillo-Box J., Jones D., Miranda L. F., Barceló Forteza S., 2020, *A&A*, 635, A128
- Andersen J., 1991, *A&ARv*, 3, 91
- Arora U., Hasegawa Y., 2021, *ApJ*, 915, L21
- Bahcall J. N., 2000, *J. R. Astron. Soc. Canada*, 94, 219
- Bakiş V., Eker Z., 2022, *Acta Astron.*, 72, 195
- Baraffe I., Homeier D., Allard F., Chabrier G., 2015, *A&A*, 577, A42
- Batten A. H., 1967, Publications of the Dominion Astrophysical Observatory Victoria, 13, 119
- Baxter E. J., Blake C. H., Jain B., 2018, *AJ*, 156, 243
- Bellinger E. P., Hekker S., Angelou G. C., Stokholm A., Basu S., 2019, *A&A*, 622, A130
- Benedict G. F., et al., 2016, *AJ*, 152, 141
- Berger T. A., Huber D., Gaidos E., van Saders J. L., Weiss L. M., 2020, *AJ*, 160, 108
- Bethe H. A., 1939, *Physical Review*, 55, 434
- Bressan A., Marigo P., Girardi L., Salasnich B., Dal Cero C., Rubele S., Nanni A., 2012, *MNRAS*, 427, 127
- Burt J., et al., 2021, *AJ*, 161, 10
- Caballero J. A., et al., 2022, *A&A*, 665, A120
- Cester B., Ferluga S., Boehm C., 1983, *Ap&SS*, 96, 125
- Chadwick J., 1933, *Proceedings of the Royal Society of London Series A*, 142, 1
- Chevalier S., Babusiaux C., Merle T., Arenou F., 2023, *A&A*, 678, A19
- Clayton D. D., 1968, Principles of stellar evolution and nucleosynthesis
- Cox A. N., 2000, Allen's astrophysical quantities
- Daszyńska-Daszkiewicz J., Miszuda A., 2019, *ApJ*, 886, 35
- Dattilo A., Batalha N. M., Bryson S., 2023, *AJ*, 166, 122
- Demarque P., Gisler G. R., 1975, *A&AS*, 20, 237
- Demircan O., Kahraman G., 1991, *Ap&SS*, 181, 313
- Dotter A., 2016, *ApJS*, 222, 8
- Eddington A. S., 1926, The Internal Constitution of the Stars
- Eggen O. J., 1956, *AJ*, 61, 361
- Eker Z., 1999, *New Astron.*, 4, 365
- Eker Z., Bakiş V., 2023, *MNRAS*, 523, 2440
- Eker Z., Bilir S., Soyduğan F., Gökçe E. Y., Soyduğan E., Tüysüz M., Şenyüz T., Demircan O., 2014, *Publ. Astron. Soc. Australia*, 31, e024
- Eker Z., et al., 2015, *AJ*, 149, 131
- Eker Z., et al., 2018, *MNRAS*, 479, 5491
- Eker Z., et al., 2020, *MNRAS*, 496, 3887

- Eker Z., Soyduğan F., Bilir S., Bakış V., 2021a, *Galactic Astronomy Workshop Proceedings Book*, 1, 51
- Eker Z., Bakış V., Soyduğan F., Bilir S., 2021b, *MNRAS*, 503, 4231
- Eker Z., Soyduğan F., Bilir S., Bakış V., 2021c, *MNRAS*, 507, 3583
- Fernandes J., Gafeira R., Andersen J., 2021, *A&A*, 647, A90
- Flower P. J., 1996, *ApJ*, 469, 355
- Gabovits J., 1938, Publications of the Tartu Astrofizika Observatory, 30, A3
- Gafeira R., Patacas C., Fernandes J., 2012, *Ap&SS*, 341, 405
- Garani R., Palomares-Ruiz S., 2022, *J. Cosmology Astropart. Phys.*, 2022, 042
- Gaulme P., et al., 2016, *ApJ*, 832, 121
- Gimenez A., Zamorano J., 1985, *Ap&SS*, 114, 259
- Gomel R., Faigler S., Mazeh T., 2021a, *MNRAS*, 504, 2115
- Gomel R., Faigler S., Mazeh T., Pawlak M., 2021b, *MNRAS*, 504, 5907
- Gorda S. Y., Svechnikov M. A., 1998, *Astronomy Reports*, 42, 793
- Griffiths S. C., Hicks R. B., Milone E. F., 1988, *J. R. Astron. Soc. Canada*, 82, 1
- Habets G. M. H. J., Heintze J. R. W., 1981, *A&AS*, 46, 193
- Harmanec P., 1988, Bulletin of the Astronomical Institutes of Czechoslovakia, 39, 329
- Henry T. J., 2004, in Hilditch R. W., Hensberge H., Pavlovski K., eds, *Astronomical Society of the Pacific Conference Series Vol. 318, Spectroscopically and Spatially Resolving the Components of the Close Binary Stars*. pp 159–165
- Henry T. J., McCarthy Donald W. J., 1993, *AJ*, 106, 773
- Hertzsprung E., 1923, *Bull. Astron. Inst. Netherlands*, 2, 15
- Hoxie D. T., 1973, *A&A*, 26, 437
- Huang S. S., Struve O., 1956, *AJ*, 61, 300
- Ibanoğlu C., Soyduğan F., Soyduğan E., Dervişoğlu A., 2006, *MNRAS*, 373, 435
- Iben Icko J., 1967, *ARA&A*, 5, 571
- Ilin E., Schmidt S. J., Poppenhäger K., Davenport J. R. A., Kristiansen M. H., Omohundro M., 2021, *A&A*, 645, A42
- Karetnikov V. G., 1991, *Azh*, 68, 880
- Kerins E., 2021, *AJ*, 161, 39
- Kerins E., et al., 2023, *arXiv e-prints*, p. [arXiv:2306.10202](https://arxiv.org/abs/2306.10202)
- Koch R. H., Plavec M., Wood F. B., 1970, A catalogue of graded photometric studies of close binaries
- Kopal Z., 1959, *Close binary systems*
- Kopal Z., 1978, *Dynamics of close binary systems*, doi:10.1007/978-94-009-9780-6.
- Kopal Z., Shapley M. B., 1956, *Jodrell Bank Ann.*, 1, 139
- Kuiper G. P., 1938, *ApJ*, 88, 472
- Lacy C. H., 1977, *ApJS*, 34, 479
- Lacy C. H., 1979, *ApJ*, 228, 817
- Lahremruati P. C., Kalita S., 2021, *MNRAS*, 502, 3761
- Malkov O. Y., 2003, *A&A*, 402, 1055
- Malkov O. Y., 2007, *MNRAS*, 382, 1073
- Malkov O., Kovaleva D., Zhukov A., Dluzhnevskaya O., 2022, *Ap&SS*, 367, 37
- McCluskey George E. J., Kondo Y., 1972, *Ap&SS*, 17, 134
- McCrea W. H., 1950, *Physics of the sun and stars*.
- McLaughlin D. B., 1927, *AJ*, 38, 21
- Moya A., Zuccarino F., Chaplin W. J., Davies G. R., 2018, *ApJS*, 237, 21
- Munday J., et al., 2020, *MNRAS*, 498, 6005
- Paczyński B., 1970, *Acta Astron.*, 20, 47
- Patterson J., 1984, *ApJS*, 54, 443
- Peled G., Volansky T., 2022, *arXiv e-prints*, p. [arXiv:2203.09522](https://arxiv.org/abs/2203.09522)
- Petrie R. M., 1950a, Publications of the Dominion Astrophysical Observatory Victoria, 8, 341
- Petrie R. M., 1950b, *AJ*, 55, 180
- Pietroni S., Bozza V., 2022, *J. Cosmology Astropart. Phys.*, 2022, 018
- Plaut L., 1953, Publications of the Kapteyn Astronomical Laboratory Groningen, 55, 1
- Popovici C., Dumitrescu A., 1974, in Mavridis L. N., ed., *Stars and the Milky Way System*. p. 169
- Popper D. M., 1980, *ARA&A*, 18, 115
- Ramesh R., Meena A. K., Bagla J. S., 2022, *Journal of Astrophysics and Astronomy*, 43, 5
- Russell H. N., Adams W. S., Joy A. H., 1923, *PASP*, 35, 189
- Schrijver K., et al., 2019, *arXiv e-prints*, p. [arXiv:1910.14022](https://arxiv.org/abs/1910.14022)
- Serenelli A., et al., 2021, *A&ARv*, 29, 4
- Stassun K. G., Collins K. A., Gaudi B. S., 2017, *AJ*, 153, 136
- Stassun K. G., Corsaro E., Pepper J. A., Gaudi B. S., 2018, *AJ*, 155, 22
- Stothers R., 1974, *ApJ*, 194, 651
- Strand K. A., Hall R. G., 1954, *ApJ*, 120, 322
- Torres G., Andersen J., Giménez A., 2010, *A&ARv*, 18, 67
- Wysoczańska R., Dybczyński P. A., Królikowska M., 2020a, *MNRAS*, 491, 2119
- Wysoczańska R., Dybczyński P. A., Polińska M., 2020b, *A&A*, 640, A129
- Xia F., Fu Y.-N., 2010, *Chinese Astron. Astrophys.*, 34, 277
- Yontan T., 2023, *AJ*, 165, 79
- Yontan T., et al., 2021, *Astronomische Nachrichten*, 342, 538
- Yontan T., Bilir S., Çakmak H., Michel R., Banks T., Soyduğan E., Canbay R., Taşdemir S., 2023, *Advances in Space Research*, 72, 1454
- Yuan H., et al., 2022, *ApJ*, 940, 165

AIMS AND SCOPE

Physics and Astronomy Reports aims to contribute to the scientific knowledge in all areas of physics and astronomy. It is an open-access, peer-reviewed and international journal published semiannually in June and December.

The journal is devoted to publish original research and review articles written in English. Original and high quality research articles, review articles (by invitation only), and high-quality conference proceedings (in special issues by the approval of the editorial board) are welcome. The journal targets international and national communities.

Processing and publication are free of charge with the journal. There is no article processing charges or submission fees for any submitted or accepted articles.

POLICIES

Publication Policy

The journal is committed to upholding the highest standards of publication ethics and pays regard to Principles of Transparency and Best Practice in Scholarly Publishing published by the [Committee on Publication Ethics \(COPE\)](#), the [Directory of Open Access Journals \(DOAJ\)](#), the [Open Access Scholarly Publishers Association \(OASPA\)](#), and the [World Association of Medical Editors \(WAME\)](#) on <https://publicationethics.org/resources/guidelines-new/principles-transparency-and-best-practice-scholarly-publishing>

The subjects covered in the manuscripts submitted to the journal for publication must be in accordance with the aim and scope of the journal. Only those manuscripts approved by every individual author and that were not published before or sent to another journal, are accepted for evaluation.

Changing the name of an author (omission, addition or order) in papers submitted to the Journal requires written permission from all the declared authors.

Plagiarism, duplication, fraudulent authorship/denied authorship, research/data fabrication, salami slicing/salami publication, breaching copyrights, and prevailing conflicts of interest are unethical behaviors. All manuscripts that are not in accordance with accepted ethical standards will be removed from publication. This also includes any possible malpractice discovered after publication.

Plagiarism:

Submitted manuscripts that pass the preliminary control are scanned for plagiarism using iThenticate software. If plagiarism/self-plagiarism is found, the authors will be

informed of it. Editors may resubmit the manuscript for a similarity check at any peer-review or production stage if required. High similarity scores may lead to rejection of the manuscript before and even after acceptance. Depending on the type of article and the percentage of the similarity score taken from each article, the overall similarity score is generally expected to be less than 15 or 20%.

Double Blind Peer-Review:

After the plagiarism check, the eligible ones are evaluated by the editors-in-chief for their originality, methodology, importance of the subject covered and compliance with the journal scope. The editor provides a fair double-blind peer review of the submitted articles and hands over the papers matching the formal rules to at least two national/international referees for evaluation and gives green light for publication upon modification by the authors in accordance with the referees' claims.

Open Access Statement

The journal is open access and all content is freely available without charge to the user or his/her institution. Except for commercial purposes, users are allowed to read, download, copy, print, search, or link to the full text of the articles in this journal without asking prior permission from the publisher or author. This is in accordance with the [BOAI](#) definition of open access.

The open access articles in the journal are licensed under the terms of the Creative Commons Attribution-NonCommercial 4.0 International ([CC BY-NC 4.0](#)) license.

Article Processing Charge

All expenses of the journal are covered by Istanbul University. The processing and publication are free of charge. There are no article processing charges or submission fees for any submitted or accepted articles.

Copyright Notice

Authors publishing with the journal retain the copyright to their work licensed under the Creative Commons Attribution-NonCommercial 4.0 International license (<https://creativecommons.org/licenses/by-nc/4.0/>) and grant the Publisher non-exclusive commercial right to publish the work. CC BY-NC 4.0 license permits unrestricted, non-commercial use, distribution, and reproduction in any medium, provided the original work is properly cited.

Correction, Retraction, Expression of Concern

The editor should consider publishing corrections if minor errors that do not affect the results, interpretations and conclusions of the published paper are detected. The editor should consider retraction if major errors and/or misconduct invalidate results and conclusions are detected.

The editors should consider issuing an expression of concern if there is evidence of research or publication misconduct by the authors; there is evidence that the findings are not reliable and institutions of the authors do not investigate the case or the possible investigation seems to be unfair or nonconclusive.

The [COPE](#) and [ICJME](#) guidelines are considered for correction, retractions or expression of concern.

Archiving Policy

To guarantee that all papers published in the journal are maintained and permanently accessible, articles are stored in Dergipark, which serves as a national archival website and simultaneously permits LOCKSS to collect, preserve, and serve content.

Additionally, the authors are encouraged to self-archive the final PDF version of their articles in open electronic archives, which conform to the standards of the Open Archives Initiative ([https:// www.openarchives.org/](https://www.openarchives.org/)). Authors should provide a link from the deposited version to the URL of IUPress journal website.

ETHICS

PUBLICATION ETHICS AND PUBLICATION MALPRACTICE STATEMENT

Physics and Astronomy Reports is committed to upholding the highest standards of publication ethics and pays regard to Principles of Transparency and Best Practice in Scholarly Publishing published by the [Committee on Publication Ethics \(COPE\)](#), the [Directory of Open Access Journals \(DOAJ\)](#), the [Open Access Scholarly Publishers Association \(OASPA\)](#), and the [World Association of Medical Editors \(WAME\)](#) on <https://publicationethics.org/resources/guidelines-new/principles-transparency-and-best-practice-scholarly-publishing>

All submissions must be original, unpublished (including full text in conference proceedings), and not under the review of any other publication. The authors must ensure that the submitted work is original in nature. They must certify that the manuscript has not already been published or submitted elsewhere, in any language. Applicable copy-

right laws and conventions must be followed. Copyright materials (e.g., tables, figures or extensive quotations) must be reproduced only with appropriate permission and acknowledgement. Any work or words by other authors, contributors, or sources must be appropriately credited and referenced.

Each manuscript is reviewed by at least two referees using a double-blind peer review process. Plagiarism, duplication, fraudulent authorship/ denied authorship, research/data fabrication, salami slicing/salami publication, breaching of copyrights, and prevailing conflicts of interest are unethical behaviors. All manuscripts that are not in accordance with accepted ethical standards will be removed from publication. This also includes any possible malpractice discovered after publication.

Research Ethics

Physics and Astronomy Reports adheres to the highest standards in research ethics and follows the principles of international research ethics as defined below. The authors are responsible for the compliance of the manuscripts with ethical rules.

- Principles of integrity, quality and transparency should be sustained in designing the research, reviewing the design and conducting the research.
- The research team and participants should be fully informed about the aims, methods, possible uses, requirements of the research, and risks of participation in research.
- The confidentiality of the information provided by the research participants and the confidentiality of the respondents should be ensured. The research should be designed to protect the autonomy and dignity of the participants.
- Research participants should voluntarily participate in the research, not under any coercion.
- Any possible harm to the participants must be avoided. Research should be planned in such a way that the participants are not at risk.
- The independence of research must be clear, and any conflicts of interest must be disclosed.
- In experimental studies with human subjects, written informed consent from the participants who decided to participate in the research must be obtained. In the case of children and those under wardship or with confirmed insanity, legal custodian assent must be obtained.

- If the study is to be carried out in any institution or organization, approval must be obtained from that institution or organization.
- In studies with human subjects, it must be noted in the method section of the manuscript that the informed consent of the participants and ethics committee approval from the institution where the study was conducted have been obtained.

Author's Responsibilities

The authors are responsible for ensuring that the article is in accordance with scientific and ethical standards and rules. The authors must ensure that the submitted work is original in nature. They must certify that the manuscript has not already been published or submitted elsewhere, in any language. Applicable copyright laws and conventions must be followed. Copyright materials (e.g., tables, figures or extensive quotations) must be reproduced only with appropriate permission and acknowledgement. Any work or words by other authors, contributors, or sources must be appropriately credited and referenced.

All the authors of the submitted manuscript must have direct scientific and academic contributions to the manuscript. The author(s) of the original research articles is defined as a person who is significantly involved in “conceptualization and design of the study”, “collecting the data”, “analyzing the data”, “writing the manuscript”, “reviewing the manuscript with a critical perspective” and “planning/conducting the study of the manuscript and/or revising it”. Fund raising, data collection and supervision of the research group are not sufficient roles to be accepted as authors. The author(s) must meet all these criteria described above. The order of names in the author list of an article must be a co-decision and must be indicated in the [Copyright Agreement Form](#).

Individuals who do not meet the authorship criteria but have contributed to the study must take place in the acknowledgement section. Individuals providing technical support, general support, material, financial support and assisting in writing are examples to be indicated in the acknowledgement section.

All authors must disclose any issues concerning financial relationships, conflicts of interest, and competing interests that may potentially influence the results of the research or scientific judgment. When an author discovers a significant error or inaccuracy in his/her own published paper, it is the author's obligation to promptly cooperate with the editor-in-chief to provide retractions or corrections of mistakes.

Responsibility for the Editor and Reviewers

The editor-in-chief evaluates manuscripts for their scientific content without regard to ethnic origin, gender, sexual orientation, citizenship, religious beliefs or the authors' political philosophy. He/She provides a fair double-blind peer review of the submitted articles for publication and ensures that all the information related to submitted manuscripts is kept as confidential before publishing.

The editor-in-chief is responsible for the content and overall quality of publications. He/She must publish errata pages or make corrections when needed.

The editor-in-chief does not allow any conflicts of interest between the authors, editors and reviewers. Only he has the full authority to assign a reviewer and is responsible for the final decision to publish the manuscripts in the journal.

The reviewers must have no conflict of interest with respect to the research, authors and/or research funders. Their judgment must be objective.

Reviewers must ensure that all information related to submitted manuscripts is kept confidential and must report to the editor if they are aware of copyright infringement and plagiarism on the author's side.

A reviewer who feels unqualified to review the topic of a manuscript or knows that its prompt review will be impossible should notify the editor and excuse him/herself from the review process.

The editor informs the reviewers that the manuscripts are confidential information and that this is a privileged interaction. The reviewers and editorial board cannot discuss the manuscripts with other people. The anonymity of referees must be ensured. In particular situations, the editor may share a review by one reviewer with other reviewers to clarify a particular point.

PEER REVIEW

Peer Review Policies

Only those manuscripts approved by every individual author and that were not published before or submitted to another journal, are accepted for evaluation.

Submitted manuscripts that pass the preliminary control are scanned for plagiarism using iThenticate software. After the plagiarism check, the eligible ones are evaluated by the editor-in-chief for their originality, methodology, importance of the subject covered, and compliance with the journal scope.

The editor hands over the papers matching the formal rules to at least two national/international referees

for double-blind peer review evaluation and gives green light for publication upon modification by the authors in accordance with the referees' claims.

Peer Review Process

Only those manuscripts approved by every individual author and that were not published before or submitted to another journal, are accepted for evaluation.

Submitted manuscripts that pass the preliminary control are scanned for plagiarism using iThenticate software. After the plagiarism check, the eligible ones are evaluated by the editor-in-chief for their originality, methodology, importance of the subject covered and compliance with the journal scope. Editor-in-chief evaluates manuscripts for their scientific content without regard to ethnic origin, gender, sexual orientation, citizenship, religious belief or political philosophy of the authors and ensures a fair double-blind peer review of the selected manuscripts.

The selected manuscripts are sent to at least two national/international external referees for evaluation, and publication decision is made by the editor-in-chief upon modification by the authors in accordance with the referees' claims.

Editor-in-chief does not allow any conflicts of interest between the authors, editors, and reviewers and is responsible for the final decision for publication of the manuscript in the journal.

The reviewers' judgments must be objective. Reviewers' comments on the following aspects are expected during the review.

- Does the manuscript contain new and significant information?
- Does the abstract clearly and accurately describe the content of the manuscript?
- Is this problem significant and concisely stated?
- Are the methods comprehensively described?
- Are the interpretations and conclusions justified by the results?
- Is adequate reference made to other works in the field?
- Is the language acceptable?

Reviewers must ensure that all information related to submitted manuscripts is kept confidential and must report to the editor if they are aware of copyright infringement and plagiarism on the author's side.

A reviewer who feels unqualified to review the topic of a manuscript or knows that its prompt review will be

impossible should notify the editor and excuse him/herself from the review process.

The editor informs the reviewers that the manuscripts are confidential information, and that this is a privileged interaction. The reviewers and editorial board cannot discuss the manuscripts with other people. The anonymity of the referees is important.

AUTHOR GUIDELINES

Manuscript Organization and Submission

1. The publication language of the journal is English
2. Authors are required to submit Copyright Agreement Form, Author Form and Title Page together with the main manuscript document
3. Manuscripts should be prepared using the article template in Latex format
4. Due to double-blind peer review, the main manuscript document must not include any author information.
5. Title page should be submitted together with the main manuscript document and should include the information below:
 - Category of the manuscript
 - The title of the manuscript.
 - All authors' names and affiliations (institution, faculty/department, city, country), e-mail addresses, and ORCIDs.
 - Information of the corresponding author (in addition to the author's information e-mail address, open correspondence address, and mobile phone number).
 - Financial support
 - Conflict of interest.
 - Acknowledgment.
6. Submitted manuscripts should have an abstract of 150-250 words before the introduction, summarizing the scope, the purpose, the results of the study, and the methodology used. Under the abstract, a minimum of 3 and a maximum of 6 keywords that inform the reader about the content of the study should be specified.
7. The manuscripts should contain mainly these components: title, abstract and keywords; sections, references, tables and figures. The main text of research articles should include introduction, methods, results, discussion, conclusion and references subheadings.
8. Tables and figures should be given with a number and

a caption. Every Figure or Table should be referred within the text of the article in numerical order with no abbreviations (ie: Table 1, Figure 1)

9. References should be prepared in line with Harvard reference system. For information: <https://www.easybib.com/guides/citation-guides/harvard-referencing/>
10. Authors are responsible for all statements made in their work submitted to the journal for publication.

References

Physics and Astronomy Reports complies with Harvard system for referencing and in-text citations. For information: <https://www.easybib.com/guides/citation-guides/harvard-referencing/>. Accuracy of citations is the author's responsibility. All references should be cited in the text. It is strongly recommended that authors use Reference Management Software such as Zotero, Mendeley, etc.

Submission Checklist

Please ensure the following:

- The title page was prepared according to the journal rules.
- This manuscript has not been submitted to any other journal.
- The manuscript has been checked for English language.
- The manuscript was written in accordance with the full-text writing rules determined by the journal.
- The manuscript has an abstract of 150-250 words and the number of keywords should be 3-6.
- The references are in line with the Harvard reference system.
- The Copyright Agreement Form has been filled in and is ready for submission together with the manuscript.
- The Author Contribution Form has been filled in and is ready for submission together with the manuscript.
- Permission for previously published copyrighted material (text, figure, table) has been obtained if used in the present manuscript.
- The Ethics Committee Report (if necessary) has been obtained and ready for submission together with the manuscript, and the ethics committee report date and number have been given in the manuscript text.
- Review of the journal policies.
- All authors have read and approved the final version of the manuscript.

EK 2-B

 Istanbul University
 İstanbul Üniversitesi

Journal name: Physics and Astronomy Reports
 Dergi Adı: Physics and Astronomy Reports

Copyright Agreement Form
 Telif Hakkı Anlaşması Formu

Responsible/Corresponding Author Sorumlu Yazar				
Title of Manuscript Makalenin Başlığı				
Acceptance Date Kabul Tarihi				
List of Authors Yazarların Listesi				
Sıra No	Name - Surname Adı-Soyadı	E-mail E-Posta	Signature İmza	Date Tarih
1				
2				
3				
4				
5				

Manuscript Type (Research Article, Review, etc.) Makalenin türü (Araştırma makalesi, Derleme, v.b.)				
Responsible/Corresponding Author: Sorumlu Yazar:				
University/company/institution	<i>Çalıştığı kurum</i>			
Address	<i>Posta adresi</i>			
E-mail	<i>E-posta</i>			
Phone; mobile phone	<i>Telefon no; GSM no</i>			

The author(s) agrees that:

The manuscript submitted is his/her/their own original work, and has not been plagiarized from any prior work, all authors participated in the work in a substantive way, and are prepared to take public responsibility for the work, all authors have seen and approved the manuscript as submitted, the manuscript has not been published and is not being submitted or considered for publication elsewhere, the text, illustrations, and any other materials included in the manuscript do not infringe upon any existing copyright or other rights of anyone. İSTANBUL UNIVERSITY will publish the content under Creative Commons Attribution-NonCommercial 4.0 International (CC BY-NC 4.0) license that gives permission to copy and redistribute the material in any medium or format other than commercial purposes as well as remix, transform and build upon the material by providing appropriate credit to the original work. The Contributor(s) or, if applicable the Contributor's Employer, retain(s) all proprietary rights in addition to copyright, patent rights. I/We indemnify İSTANBUL UNIVERSITY and the Editors of the Journals, and hold them harmless from any loss, expense or damage occasioned by a claim or suit by a third party for copyright infringement, or any suit arising out of any breach of the foregoing warranties as a result of publication of my/our article. I/We also warrant that the article contains no libelous or unlawful statements, and does not contain material or instructions that might cause harm or injury. This Copyright Agreement Form must be signed/ratified by all authors. Separate copies of the form (completed in full) may be submitted by authors located at different institutions; however, all signatures must be original and authenticated.

Yazar(lar) aşağıdaki hususları kabul eder:

Sunulan makalenin yazar(lar)ın orijinal çalışması olduğunu ve intihal yapmadıklarını, Tüm yazarların bu çalışmaya aslı olarak katılmış olduklarını ve bu çalışma için her türlü sorumluluğu aldıklarını, Tüm yazarların sunulan makalenin son halini gördüklerini ve onayladıklarını, Makalenin başka bir yerde basılmadığını veya basılmak için sunulmadığını, Makalede bulunan metnin, şekillerin ve dokümanların diğer şahıslara ait olan Telif Haklarını ihlal etmediğini kabul ve taahhüt ederler. İSTANBUL ÜNİVERSİTESİ'nin bu fikri eseri, Creative Commons Atıf-GayrıTicari 4.0 Uluslararası (CC BY-NC 4.0) lisansı ile yayınlamasına izin verirler. Creative Commons Atıf-GayrıTicari 4.0 Uluslararası (CC BY-NC 4.0) lisansı, eserin ticari kullanım dışında her boyut ve formatta paylaşılmasına, kopyalanmasına, çoğaltılmasına ve orijinal esere uygun şekilde atıfta bulunmak kaydıyla yeniden düzenleme, dönüştürme ve eserin üzerine inşa etme dâhil adapte edilmesine izin verir. Yazar(lar)ın veya varsa yazar(lar)ın işverenin telif dâhil patent hakları, fikri mülkiyet hakları saklıdır. Ben/Biz, telif hakkı ihlali nedeniyle üçüncü şahıslarca vuku bulacak hak talebi veya açılacak davalarda İSTANBUL ÜNİVERSİTESİ ve Dergi Editörlerinin hiçbir sorumluluğunun olmadığını, tüm sorumluluğun yazarlara ait olduğunu taahhüt ederim/ederiz. Ayrıca Ben/Biz makalede hiçbir suç unsuru veya kanuna aykırı ifade bulunmadığını, araştırma yapılırken kanuna aykırı herhangi bir malzeme ve yöntem kullanılmadığını taahhüt ederim/ederiz. Bu Telif Hakkı Anlaşması Formu tüm yazarlar tarafından imzalanmalıdır/onaylanmalıdır. Form farklı kurumlarda bulunan yazarlar tarafından ayrı kopyalar halinde doldurularak sunulabilir. Ancak, tüm imzaların orijinal veya kanıtlanabilir şekilde onaylı olması gerekir.

Responsible/Corresponding Author; Sorumlu Yazar;	Signature / İmza	Date / Tarih
	/...../.....